CONTROL OF WATER AND TOXIC GAS ADSORPTION IN METAL-ORGANIC FRAMEWORKS

Matthew J. McPherson

A Thesis Submitted for the Degree of PhD
at the
University of St Andrews

2016

DOI: https://doi.org/10.17630/10023-16489
http://hdl.handle.net/10023/16489

Control of Water and Toxic Gas Adsorption in Metal-Organic Frameworks

Matthew J. McPherson

University of
St Andrews

This thesis is submitted in partial fulfilment for the degree of PhD

at the

University of St Andrews

May 2016

Candidate's Declarations

I, Matthew J. McPherson hereby certify that this thesis, which is approximately 33,551 words in length, has been written by me, and that it is the record of work carried out by me, or principally by myself in collaboration with others as acknowledged, and that it has not been submitted in any previous application for a higher degree.

I was admitted as a research student in January,2012 and as a candidate for the degree of PhD in January, 2013; the higher study for which this is a record was carried out in the University of St Andrews between 2012 and 2016.

(*If you received assistance in writing from anyone other than your supervisor/s*):

I, Matthew J. McPherson, received assistance in the writing of this thesis in respect of grammar and syntax which was provided by Dr Laura J. M^{c}Cormick and Martin W. Smith.

Date Matthew J. McPherson

2. Supervisor's declaration:

I hereby certify that the candidate has fulfilled the conditions of the Resolution and Regulations appropriate for the degree of PhD in the University of St Andrews and that the candidate is qualified to submit this thesis in application for that degree.

Date …… Professor Russell E. Morris

3. Permission for publication: (*to be signed by both candidate and supervisor*)

In submitting this thesis to the University of St Andrews I understand that I am giving permission for it to be made available for use in accordance with the regulations of the University Library for the time being in force, subject to any copyright vested in the work not being affected thereby. I also understand that the title and the abstract will be published, and that a copy of the work may be made and supplied to any bona fide library or research worker, that my thesis will be electronically accessible for personal or research use unless exempt by award of an embargo as requested below, and that the library has the right to migrate my thesis into new electronic forms as required to ensure continued access to the thesis. I have obtained any third-party copyright permissions that may be required in order to allow such access and migration, or have requested the appropriate embargo below.

The following is an agreed request by candidate and supervisor regarding the publication of this thesis:

PRINTED COPY

Embargo on all or part of print copy for a period of 5 years on the following ground(s):

- Publication would preclude future publication

ELECTRONIC COPY

Embargo on all or part of electronic copy for a period of 5 years on the following ground(s):

Publication would preclude future publication

Permanent or longer term embargo on all or part of electronic copy for a period of 5 years (the request will be referred to the Pro-Provost and permission will be granted only in exceptional circumstances).

Date Matthew J. McPherson Professor Russell E. Morris

Acknowledgements

I would like to extend my thanks to Professor Russell Morris of the University of St Andrews as well as Martin W. Smith and Dr Corinne Stone of Dstl for the opportunity to undertake this work and for their guidance over the years spanned by my PhD.

Thanks also to everyone in the Morris group, both past and present for their company and acting as a sounding board to my ramblings as I wrote up.

Special thanks to our collaborators, Gregory W. Peterson of Edgewood Chemical and Biological Center in the United States of America and Professor Barbara Gil of Jagellion University, who provided invaluable measurements and data to compare our materials to previously explored materials.

Thank-you to Charlotte Sansome and Dr. Daniel Dawson for their assistance with MAS-NMR work.

Thank-you to all the technical and support staff in the Chemistry department, especially Sylvia Williamson, without whose patient tutelage, analytical expertise and wisdom, this thesis would be much shorter and far less interesting.

I gratefully acknowledge the funding provided by Dstl for this project.

Love and thanks to my family, Gary, Eileen and Marc for their unending support and confidence in me. You had more faith than I did.

And lastly, to my dearest Laura McCormick, who was there for every high and low and who lit the road ahead so I could see where to place my feet. No distance can ever keep you from my heart. I am yours, forever and always.

Abstract

The research presented in this thesis aims to determine the effectiveness of the uptake of toxic gases by several MOFs for future use in gas-mask cartridges, and to attempt to compensate for any deficiencies they show in “real-world” conditions.

The main findings of this thesis confirm that MOFs are suitable candidates for the use in respirator cartridge materials and provide high capacity for adsorption of toxic gases like ammonia and STAM-1 in particular showed an impressive improvement in humid conditions, which normally decrease the performance of MOFs made from the same materials, such as HKUST-1.

STAM-1’s improved performance in humid conditions is attributed to the structural shift it displays upon dehydration and rehydration and this was shown to be the case in a structural analogue, CuEtOip, which was synthesised in the author’s research group. This analogue was analysed using a combination of single crystal XRD and solid state MAS-NMR, both of which showed the structural change occurring and displays similar gas sorption behaviours, suggesting that this mechanism is the source of STAM-1’s improved performance in humid conditions.

This thesis also examines the “Armoured MOF” process and investigates the transferability of the process of deposition of mesoporous silica onto MOFs with vastly different properties and synthetic methods compared to those published in the original publication. Alongside this, attempts to protect MOFs using mesoporous silicates were investigated for their viability.

Publications

Publications arising from work described in this Thesis:

The Effect of Humidity on Ammonia Removal from Contaminated Airstreams by the Metal-Organic Frameworks STAM-1 and HKUST-1.

Matthew J. McPherson, Martin W. Smith, Corinne A. Stone, Gregory W. Peterson, Russell E. Morris, *J. Mat. Chem. A*, In review

Publications arising from work not described in this Thesis:

Coordination polymers of Zn^{II} and 5-methoxy isophthalate

Laura J. McCormick, Samuel A. Morris, Simon J. Teat, **Matthew J. McPherson**, Alexandra M. Z. Slawin and Russell E. Morris, *Dalton Trans.*, 2015, **44**, 17686-17695 DOI: 10.1039/C5DT02924D

Ionic Liquid assisted Synthesis of Zeolite-TON

Yuyang Tian, **Matthew J. McPherson**, Paul S. Wheatley, and Russell E. Morris, *Z Anorg. Allg. Chem.,* 2014, **640**, 1177–1181.

"Better to run, than curse the road"

Zambian Proverb

Table of Contents

Chapter 1 Introduction

1.1. Respirator Cartridges

Gas masks are an important tool for emergency first-responders and military personnel for ensuring their safety during the course of their duties. Many airborne contaminants encountered by first-responders and military personnel have rapid onsets of symptoms including disorientation and incapacitation, which can easily lead to fatalities without a method to mitigate the effects. A chemical cartridge respirator allows users to immediately limit their exposure to a toxic agent and enables them to remove themselves from a situation to avoid further harm.

The modern respirator is comprised of two main parts, a particulate filter and an adsorbent. This project aims to investigate materials that will augment or replace components of the adsorbent material. The current adsorbent material is comprised of a mixture of activated carbon, copper, silver, zinc, molybdenum, and triethylenediamine (more commonly known as DABCO).[1] Metal-organic frameworks represent a material with a high surface area and high capacity for removal of toxic molecules, alongside the potential to design frameworks that are effective against specific contaminants by varying the metals and ligands used in their construction.

1.2. Metal-Organic Frameworks

These materials are comprised of metal centres or clusters of metal centres that are connected by organic bridging ligands to form an extended framework that extends in 1, 2 or 3-dimensions.

The concept of a deliberately designed coordination polymer was first posited by Robson and Hoskins in 1990[2] and initial reports of what would later be termed metal-organic frameworks (MOFs) occurred some twenty years ago by Yaghi *et al.*[3] Since then the area has experienced a huge amount of interest. There has been a large amount of time invested into determining exactly what constitutes a MOF[4] and it was only as recently as 2013 that a general consensus has been reached and International Union of Pure and Applied Chemistry (IUPAC) guidelines have been published.[5] The guidelines state that a MOF "is a co-ordination network with organic ligands containing potential voids". As such a co-ordination network is defined as "a co-ordination compound extending through repeating co-ordination entities in 1 dimension but with cross-links between two or more individual chains, loops or spiro-links, or a co-ordination compound extending through repeating co-ordination entities in 2 or 3 dimensions." In the simplest terms, a MOF represents a molecular sponge, containing open channels which are accessible to other molecules.

In terms of classification of the size of the openings in the structure, MOFs are microporous i.e. having a pore diameter below 2 nanometres, as opposed to mesoporous compounds which have a pore diameter in the range of 2-50nm or macroporous compounds which have pore diameters greater than 50nm.[6] There have however, been several reported mesoporous MOFs (or meso-MOFs). The larger pore sizes have been achieved either through the use of extended ligands, or by use of templating materials. Templating materials include quaternary ammonium salts, or organic molecules such as DABCO or co-block polymers such as Pluronic 123. These are termed “soft” templates which are used in the synthesis of mesoporous solids that form micelles in solution, around which the materials are deposited. These materials are then typically calcined at high temperatures, causing the template material to burn off and leave open-channels behind.

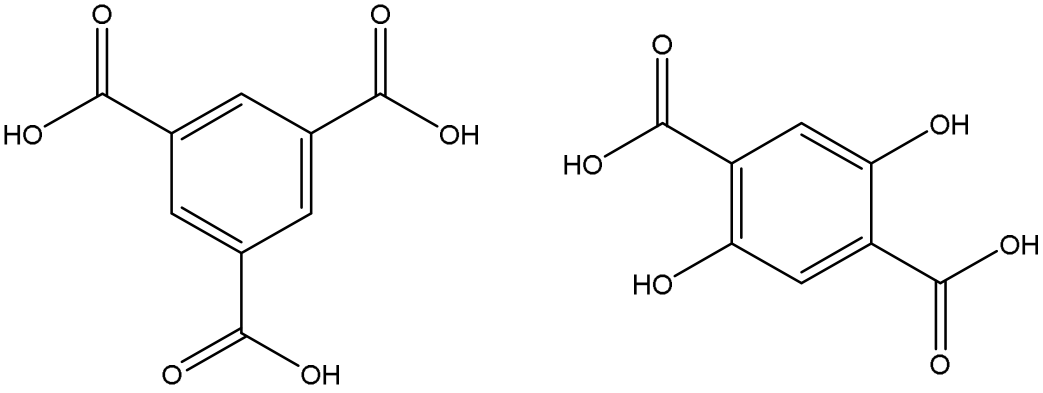

trimesic acid

2,5-dihydroxyterephthalic acid

Figure 1: 1,3,5-benzenetricarboxylate (left) and 2,5-dihydroxyterephthalic acid (right)

Figure 1 shows two typical bridging ligands that are components of the MOFs used as part of this project. Ligands used to make MOFs typically contain two or more carboxylic acid groups bound to an aromatic core such as a phenyl ring, or a biphenyl or naphthalene unit. Other functional groups such a hydroxyl, amine or pyridyl groups may also be used to coordinate metal centres or provide additional binding sites for guest molecules.

Many MOFs also have solvent molecules binding to the metal centres. In some cases, these co-ordinated solvent molecules may be removed to leave a highly reactive vacant co-ordination site on the metal. This is a desirable property in MOFs that are being investigated for gas storage[7] and drug delivery.[8] Guest molecules may be stored in the MOF powder by exposing the powder to liquid or gas which diffuses into open channels and binds to the open metal sites throughout the structure, The guest can then later be recovered from the MOF by application of heat or another guest molecule, most typically water, which possesses a strong binding affinity for the metal ions. The guest molecules are then released into the environment where they can be utilised for their intended purpose.

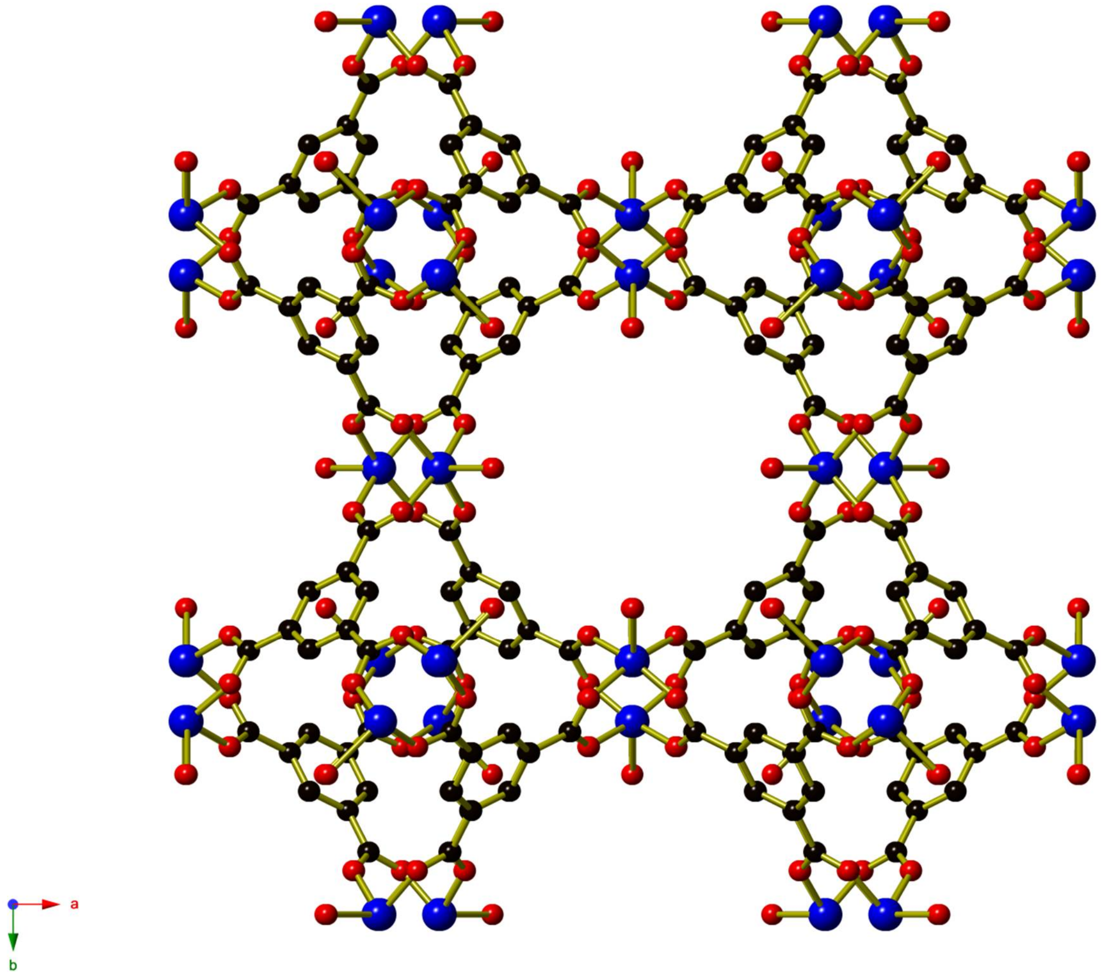

Figure 2: Crystal structure of the MOF, HKUST-1, made from 1,3,5-benzenetricarboxylic acid (btc) and copper metal centres. Key: C: Black, O: Red, Cu: blue. Hydrogen atoms omitted for clarity.

A well-studied example of a MOF is HKUST-1 (Figure 2) which was first reported in 1999.[9] The repeating unit within the structure is an octahedral cage in which copper acetate lantern-like units are located at the six vertices and a btc ligand occupies four of the eight faces. Copper acetate lanterns connect adjacent cages such that each cage is connected to six others and adjacent cages are related by mirror symmetry. This extends in all three dimensions to create the infinite framework. Within the framework, the cages are arranged so that they sit at the corners of a cube. The framework is porous and contains three perpendicular series of channels that run through the centre of each of the cube faces and intersect at the centre of the cubes. Solvent is able to travel freely through the channels, and through the octahedral cages via the four faces of the octahedra that are not blocked by the btc^{3-} ligands, which act as windows between the channels and the spaces inside the cages.

In HKUST-1, the copper centres are bound to solvent molecules that project into the pores and may be removed by heating the MOF, or placing it in a reduced pressure environment. Once these co-ordinated solvent molecules removed, this leaves what are termed co-ordinatively unsaturated metal sites (CUS) to which guest molecules can bind. They can later be released by increasing the temperature, reducing the ambient pressure or by introduction of another molecule which has a higher affinity for the metal-centre, typically water.

Synthesis of MOFs can be undertaken using a variety of methods. Solvothermal methods conducted in autoclaves may be used to produce highly crystalline materials suitable for analysis but as research indicated that MOFs had many useful applications, the need to develop methods suitable for mass production brought several different strategies to the forefront. HKUST-1 has been produced by spray drying (where the reagents are mixed in a heated gas stream[10]), ball milled in minimal solvent,[11] synthesised at room temperature[12] or under reflux at ambient pressure.[13] Other methods of industrial scale-up such as flow processing are also under investigation.[14]

Many MOFs have high surface area and, open-metal sites and with potential to design frameworks that are suited to task makes them excellent candidates for separation of mixed gases and liquids[15], catalysis[16], drug delivery[8] and gas adsorption of many different gases including hydrogen[17,18], hydrogen sulphide[19], hydrocarbons[20,21], ammonia[22], nitric oxide [23]and carbon dioxide[7]. A recent review[24] issue of Chemical Reviews examined over 4000 pieces of new research in the field.

1.3. MOFs as Toxic Gas Adsorbents

This study primarily looks into the ability of metal-organic frameworks (MOFs) to act as gas adsorbents and separators, removing toxic molecules and allowing breathable air to pass through uninhibited. In this project, ammonia gas uptake is being investigated as a commonly encountered threat for personnel in front line situations and first-responders dealing with emergencies. MOFs have shown evidence of uptake of a wide range of toxic gases including toxic hydrides,[25] as well as being investigated for use in respirators, MOFs are being explored for their ability to remove toxic or unwanted gases from a variety of air-streams, including industrial flue gases.[26]

Other gases also need to be adsorbed and contained safely which can include hydrocarbons, carbon monoxide, hydrogen sulphide and nitric oxide, the latter two of which are well studied for their uptake and release from MOFs due to the beneficial properties they display in therapeutic quantities.[8,23,27] As such MOFs present a good all round choice for their ability to selectively adsorb the aforementioned gases while still allowing the passage of oxygen and nitrogen through the material, ensuring a supply of breathable air. The metals and organic ligands used in MOFs are also usually relatively cheap and the materials themselves often exhibit reversible adsorption characteristics, allowing them to be reused by simple thermal desorption of adsorbates This property can be troublesome however if the innocuous gases have a higher affinity for the vacant co-ordination site than the contaminant to be removed does. For examples, H_2O has a greater affinity for the vacant co-ordination sites than nitric oxide does in the works referenced above. This results in the bound material being displaced from the open metal sites and replaced by a harmless molecule. While this is highly useful for a drug delivery system, it could be potentially catastrophic for a filter system. Investigation of the difference between the physisorptive and chemisorptive properties that MOFs display will be crucial to determination of the fitness of the materials for purpose.

A further potential benefit of MOFs over the traditional adsorbents currently in use is that MOFs can often be modified either by use of functionalised ligands or post-synthetic modification of the material. This allows for scope to improve a material in certain areas by adding key functionalities to improve performance or allow for adsorption that did not take place before, for example, addition of NH_2 groups for removal of CO_2 or for increasing capacity of NO. A large number of different of current chemical cartridges have specialised active materials designed to deal with different known threats. By having a base material than can be further functionalised to cope with specific threats, this will allow a consistent level of protection against both known and unknown threats.

Different ligands and metals lend themselves to different properties and, as such, selection of a suitable MOF that fits the task at hand is a key factor before this study can begin. Several key criteria must be addressed:

- The MOF must be stable when desolvated.
- The MOF must be suitable for industrial scale synthesis.
- The MOF must not exhibit degradation of performance when stored for extended periods.
- The MOF should be able to withstand modification or functionalization to improve properties with relation to specific contaminants.

Several well-known and characterised MOFs were selected that could be reliably produced and would likely be suitable for industrial scale synthesis in the future.

1.4. CPO-27 Series

The framework designated CPO-27 was initially selected as a potential candidate due to the numerous analogues available by reacting the 2,5-dihydroxyterephthalate (H_4dhtp) with different metal salts to produce the same overall structure. The structure (Figure 3) has shown great promise in CO_2 adsorption[7] even at low pressures and displays a high affinity for CO_2 over other gases like nitrogen and methane[28] . The nickel and magnesium analogues of this MOF will be investigated as each offer different properties relating to capacity and long term stability.

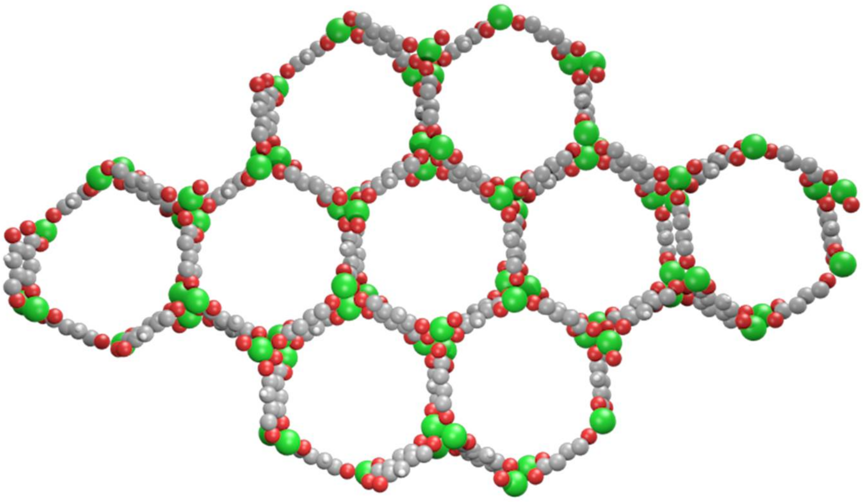

Figure 3:3D Model of a CPO-27 Structure. Key: Carbon: Grey, Oxygen: Red, Green: Metal atoms (Ni, Mg, Cu, Mn, Zn).

The nickel derivative is expected to be the more stable of the two structures when exposed to water or heat while the magnesium species has been consistently shown to have one of the highest known capacities for storage of CO_2 inside a MOF, adsorbing up to 68% by weight at elevated pressure for the magnesium derivative and 51% by weight for the nickel derivative, also at elevated pressure.[29] Figure 3 shows the structure of the material, where the 2,5-dhtp^{4-} is indicated by the carbon (grey) and oxygen (red) spheres and the metal centres are represented in green. Hydrogen atoms are omitted for clarity. The structure of these materials is a honeycomb-like framework that contains a series of 1-d channels that can be occupied by guest molecules. An animation to illustrate the structure, the differing metals that can be used with the same organic ligand and the loading and unloading of guest molecules is available online and in the digital version of this thesis.[30]

The selection of CPO-27-M series (M = Mg, Mn, Fe, Co, Ni, Cu and Zn) offers multiple metal ions to choose from, all of which produce the same structure but each of which have their own implications for use. CPO-27-Co was not considered as the use of cobalt, which is highly toxic, in a material to be used for air filtration was deemed too hazardous. CPO-27-Ni was selected for its general all round ability, showing good CO_2 adsorption of around 5mmol/g at atmospheric pressure, relative stability in water and ease of synthesis, despite a lack of crystallinity.[31,32] CPO-27-Mg was also selected due to its exceptional CO_2 adsorption capacity at low pressures of CO_2[33], holding over 5mmol/g at 0.1 atm and nearly 8mmol/gram at standard temperature and pressure (STP). CPO-27-Mn and CPO-27-Fe are not stable in air.

There is potential for confusion of terms regarding this structure MOF-74 or CPO-27 where MOF-74 tends to be used to describe the zinc or cobalt based framework and CPO-27 usually refers to those incorporating magnesium or nickel, clarified by the addition of the elemental symbol to the end. However, they are isostructural and are often used interchangeably to mean the same structure, depending on the author of a report. Throughout this report which focuses on the magnesium and nickel variants, they will be referred to exclusively as CPO-27-Mg and CPO-27-Ni respectively, however, cited articles may refer to MOF-74, even for the Mg/Ni variants thus necessitating that this distinction be made.

1.5. STAM-1

An alternate MOF was also selected as a potential candidate as it displayed an interesting dual pore system.

STAM-1 (Figure 4) was first reported in 2011[34] and was the first in a series of MOFs developed at St Andrews University. It is produced by reaction of $Cu(NO_3)_2$ and trimesic acid in aqueous methanol under similar conditions to those used to synthesise HKUST-1, a MOF which has been extensively studied and produced on an industrial scale. So far, STAM-1 has not been widely explored beyond the initial reporting. Unlike HKUST-1, STAM-1 forms as a two-dimensional coordinate framework. Two of the three carboxylate groups are co-ordinated to the copper centres, to form copper acetate lantern units similar to those found in HKUST-1. The third carboxylate group has been methylated and so does not coordinate to any copper ions. The monomethyl ester of trimesate thus acts as a two-connecting ligand, bridging Cu dimers into a two-dimension framework of Kagome topology, an arrangement of tessellated equilateral triangles and regular hexagons. The Kagome framework contains two different types of channel, channels with triangular cross-section into which the co-ordinated water molecules project, giving it hydrophilic character; the other channel has a hexagonal cross section into which the methyl ester groups project, giving hydrophobic character. The hydrophilic pores are occupied by disordered solvent molecules whilst the hydrophobic pores remain empty.

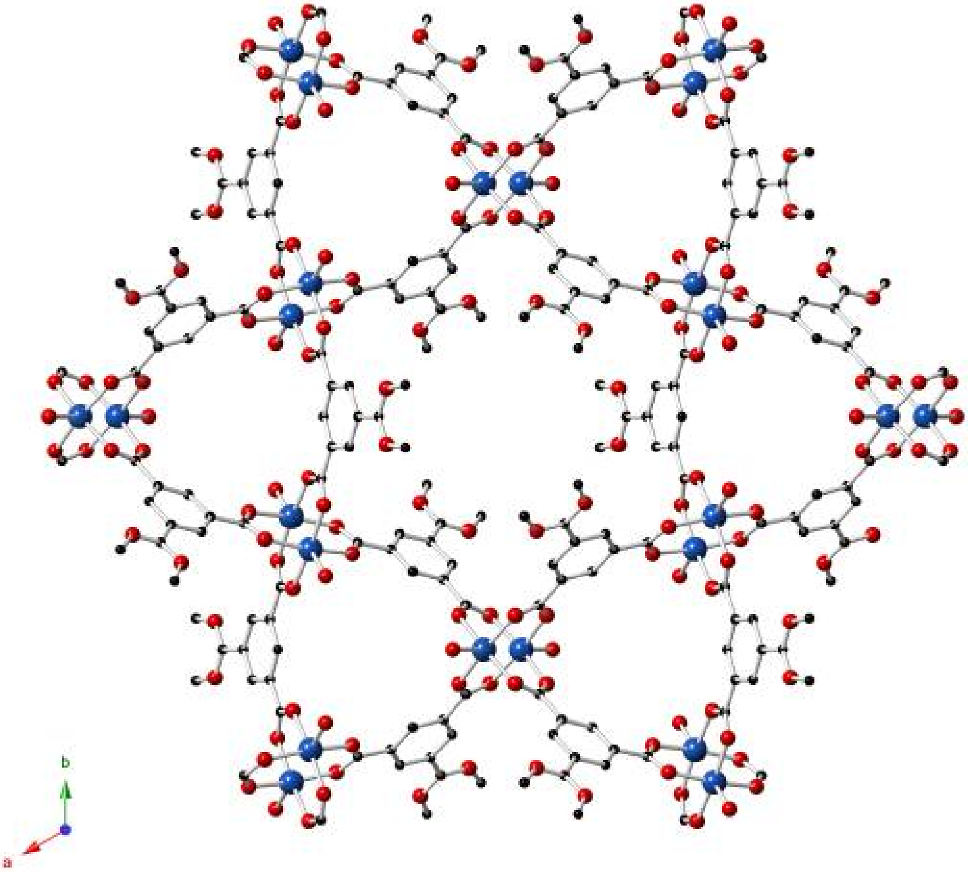

Figure 4: Single Crystal Structure of STAM-1. Hydrogen atoms and solvent molecules have been omitted for clarity. Key: C: Black, O: Red, Cu: blue. Hydrogen atoms omitted for clarity.

The hydrophobic pores of STAM-1 also confer an increased stability in water when compared to HKUST-1, which is unstable in wet conditions, rapidly losing crystallinity and suffering from pore collapse when exposed to water for extended periods. STAM-1 does not suffer from this problem, showing greatly increased stability in humid conditions and also higher stability at elevated temperatures. The MOF displays a Kagome-type lattice and has an unusual property that was, until recently,[35] relatively rare in MOFs, where the structure appears to "breathe", causing pores to open and close reversibly within the structure. This behaviour is not unique to STAM-1, with MIL-53 showing a similar breathing behaviour upon dehydration and rehydration.

It was initially hypothesised that the breathing behaviour of STAM-1 was tied to the concerted opening and closing of the two types of pores but this has now been revised, in that the removal of solvent causes a reversible structural rearrangement.[35,36]

An attractive property of this MOF is the presence of copper metal centres in the structure. Research in the field of adsorbents has shown that in protection against ammonia, copper based materials HKUST-1 and Cu-ZSM-5 (a zeolite which has been infused with copper) are shown to have an exceptionally high ammonia adsorptive capacity in dry conditions. The work of Peterson, Decoste and co-workers [25,37–39] has focussed largely on the use of HKUST-1 as an adsorbent against ammonia in filter materials which shows an astonishing capacity for ammonia. However the MOF material breaks down during the ammonia adsorption, resulting in formation of copper diamine complexes and ammonium salts of trimesic acid in dry conditions and copper hydroxide in wet conditions. Given the industrial availability of HKUST-1 but with the attendant problems encountered with the material potentially breaking down in humid conditions before it can be used, the investigation of STAM-1, which is comprised of the same materials as HKUST-1, could provide a viable alternative that offers strong protection along with enhanced shelf life.

1.6. Protection Strategies

It is apparent that while a large number of MOFs display excellent gas storage properties in controlled laboratory conditions, it becomes much more difficult to maintain such efficiency in "real-world" conditions. Fine control over the atmosphere surrounding the materials is not possible in real-world scenarios, particularly given the ubiquitous presence of water, which preferentially binds to open metal sites in a large majority of MOFs, displacing and leaving the toxic and unwanted gases free to move on through the pores of the filter material. To this end, attempts were made to select MOFs that had these excellent gas storage and separation properties and protect them using a variety of methodologies where hydrophobic outer coatings will exclude any atmospheric water allowing the open metal sites to remain available. This would allow toxic gases to bind to the metal sites, while nitrogen and oxygen will continue to pass through the pores and out the other side of the filter material. Several strategies to protect the MOFs were investigated, centred around mesoporous silicas.

1.7. Mesoporous Silicas

A mesoporous solid refers to a class of materials which have pore openings in the size range of 2-50nm, placing them in the middle of the spectrum of pore size (MOFs fall into the microporous category, having pore sizes below 2nm and the macroporous materials containing pore sizes above 50nm in diameter).[40] The most common mesoporous materials in nature are silicates or aluminates but there are also dozens of synthetic variants that have been produced in the last few decades.[41]

These materials show huge surface areas and have been used in the past for nanocasting of materials[42], or as catalysts[43] and molecular sieves[44]. They are noted for having exceptionally high surface areas ranging into the thousands of square metres per gram, allowing them to take up huge amounts of gas but they are unable to store it effectively without further modification. They exhibit little selectivity for the gases involved except where the pore size would exclude the adsorption of a particular gas. A desirable property for the purposes of this study, however is the large scope for modification of the functional groups present on the surface of the mesoporous structure without loss of the high surface area or porisity. This method allows for the incorporation of functional groups that give the silicas useful properties, such as an increase in hydrophobicity or alteration of selectivity. Similar modifications cannot necessarily be carried out on the metal-organic framework structures, as extensive modification of the MOF can either cause dissolution of the desired structure or a reduction in desired properties like gas adsorption capacity. Numerous studies of CO_2 adsorption by post-synthetically modified silica have been carried out,[45,46] showing that it is possible for the silica to be modified in some way so that it may retain CO_2 in a useful manner. Later work may involve multiple modifications to further fine tune the properties of the material and enhance adsorption.

The combination of two different classes of porous solids has been reported in literature as a "nano-hybrid"[47] using a combination of mesoporous silica furnished with a series of functional groups to make an outer shell with high hydrophobic character while the internal mesopores[48] are packed with a suitable metal-organic framework to adsorb undesirable gases in environments that contain water. This characteristic sets this class of materials apart from those which are currently being investigated for industrial CO_2 adsorption in flue gas systems where water is removed from the gas mixture during the cooling process and, as a result, large volumes of water never come into contact with the adsorbents designed to take up CO_2.

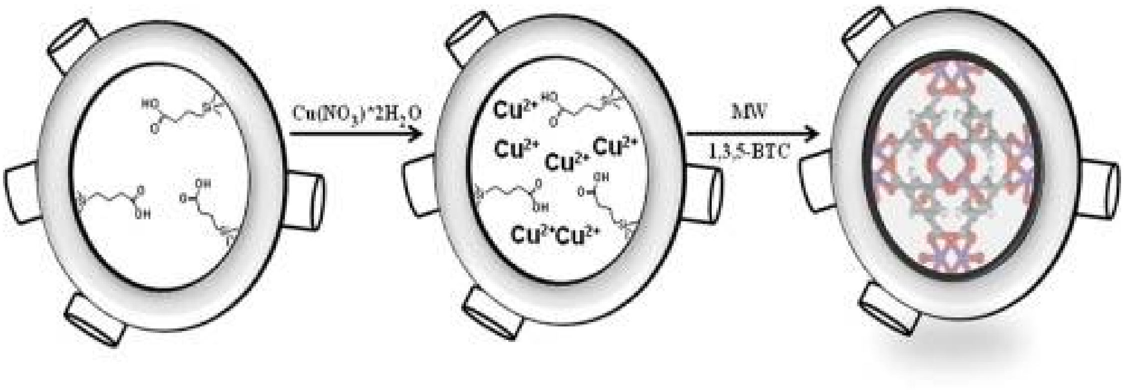

Figure 5: Modified Mesoporous Silica containing a MOF.[47]

The composite material detailed above is however, at most, a crude mixing of the two materials and as such it becomes very difficult to control the distribution of the MOF in the material. In order to better protect the MOF, a more direct approach may be used where the as-synthesised MOF is treated with a polymer and then has a layer of silica deposited onto the surface of the polymer using a standard template-directed synthesis, such as cetyl-trimethyl ammonium chloride or bromide (CTACl and CTAB, respectively). The template is then removed by heating, leaving the MOF enveloped within a silica "armour" that completely encases the MOF particles but also allows access by gases through a slightly hydrophobic barrier. This "armour" can also potentially be modified to alter its properties and improve its performance depending on what toxic gases are expected to be encountered, while still providing good all-round protection against a wide variety of toxins. This method was originally attempted as an avenue to improving the stability and mechanical strength of MOFs, enabling them to be used in a wider variety of applications where the conditions would be unsuitable for the as-synthesised MOF.

It should be noted that there have been numerous reports of successfully using ionic liquids as a templating agent for the production of mesoporous silicas. As our early research suggested that ionic liquids would not negatively affect the uptake of the gases into the MOF material, they presented a natural choice as an avenue of expanding the method reported by Li and Zheng.[49] By using the ionic liquids to template the silica shell, it allows a wider range of MOFs to be explored, including those which might not survive the calcination needed to remove the traditional templating agent from the silica, one such example being HKUST-1 which is not capable of being heated to the decomposition point of CTAB (over 243°C) without losing structural integrity and degrading. The ability to use MOFs without the need to expose them to harsh conditions to remove templating agents opens up the possibility of applying the armouring process to other MOFs that while perfectly capable adsorbents, may not be able to withstand the rigorous conditions needed for the standard armouring procedure.

By refining the protection strategy for use on a wide variety of MOFs, we can potentially expand MOFs into applications where extreme conditions were unsuitable for the use of these materials.

1.8. Aims and Thesis Overview

MOFs represent a class of compounds that offer potentially the largest variety of structural types and functionalities, compared to other traditional adsorbent materials such as activated carbon and zeolites. During the course of this PhD, the aim of the project was investigate known MOFs for their ability to remove small molecule toxic gases, such as ammonia, and to attempt to allow them to continue adsorbing toxic gases in humid conditions, which have been shown to considerably reduce the overall capacity of MOFs used for this purpose.

The MOFs selected for examination over the course of the project included CPO-27-Mg, CPO-27-Ni and STAM-1. The CPO-27 series (also described as MOF-74) of MOFs reported by Yaghi *et al*[50] and Dietzel *et al*[31] is an isostructural series made with the 2,5-dihydroxyterephthatlic acid (H_4dhtp) ligand which has been reported using cobalt, nickel, magnesium, manganese, zinc, copper[51] and iron[35]. STAM-1 was first reported in 2011 by Mohideen *et al*[52] by reaction of the same components as HKUST-1 in a methanolic solution. This causes the methylation of one of the carboxylic acid groups, resulting in the formation of a two-dimensional coordination framework that contains two different pore types, as opposed to the three-dimensional framework of HKUST-1.

The first objective of the PhD was to attempt to find a method which would allow the above mentioned MOFs to selectively take up a toxic gas, in this case ammonia, while preventing water from occupying the open-metal sites of the framework. This will be investigated using barrier methods. Design and modification of these barriers will be the primary means of preventing water from occupying potential adsorption sites.

Secondly, STAM-1 showed unexpected improvement in humid conditions that had not been observed in HKUST-1. Determination of the mechanism by which the MOF takes up ammonia under both dry and humid conditions forms a large part of the work undertaken here. Due to the original STAM-1 material not retaining single crystal character upon dehydration, examination was undertaken on a structural analogue reported by McCormick *et al*.[35] Examination of this analogue and comparison with STAM-1 allows us to propose a potential mechanism for the uptake of ammonia in Kagome lattice structured MOFs.

Chapter 1 gives an introduction of metal-organic frameworks (MOFs), the MOFs explored in this thesis and the additional materials used to improve their performance, primarily mesoporous silica.

Chapter 2 details the theoretical basis behind the experimental techniques used in this thesis and Chapter 3 gives details of the synthetic procedures and practicalities of running the experiments undertaken in this thesis.

STAM-1 and its performance in ammonia adsorption under both dry and humid conditions covers a large part of the work undertaken. This MOF displays a “breathing” ability upon dehydration and rehydration, which causes a structural re-arrangement that alters what parts of the MOF take up ammonia. Chapter 4 details the mechanism of ammonia uptake in STAM-1, a comparison with an isostructural material that allows for single-crystal diffraction to observe the structural rearrangement, and STAM-1’s performance compared with HKUST-1 in a variety of conditions.

The CPO-27 series was also explored for its potential to remove ammonia from airstreams. Much of the work in Chapter 5 deals with attempting to produce a composite material that will allow the material to continue taking up ammonia in humid conditions by exluding water, which would normally occupy open metal sites and limit the total ammonia capacity of the material. This was attempted using mesoporous silicas.

Chapter 6 covers further attempts at improving MOFs using mesoporous silica, using a method that fully encapsulates particles of the material in a shell of mesoporous silica, rather than *in situ* formation of the MOF described in Chapter 6. The encapsulated materials show an improvement in thermal resistance over the as-synthesised materials, but little improvement at ammonia uptake in humid conditions.

Chapter 7 concludes the thesis, summarises the findings and discusses future work that could be conducted.

1.9. References

1 M. Jacoby, *Chemical & Engineering News*, 2014, 92.

2 B. F. Hoskins and R. Robson, *J. Am. Chem. Soc.*, 1989, **111**, 5962–5964.

3 O. M. Yaghi and H. Li, *J. Am. Chem. Soc.*, 1995, **117**, 10401–10402.

4 S. R. Batten, N. R. Champness, X.-M. Chen, J. Garcia-Martinez, S. Kitagawa, L. Öhrström, M. O'Keeffe, M. P. Suh and J. Reedijk, *CrystEngComm*, 2012, **14**, 3001.

5 S. R. Batten, N. R. Champness, X.-M. Chen, J. Garcia-Martinez, S. Kitagawa, L. Öhrström, M. O'Keeffe, M. Paik Suh and J. Reedijk, *Pure and Applied Chemistry*, 2013, **85**.

6 *Metal-organic frameworks: applications from catalysis togas storage*, Wiley-VCH, Weinheim, 2011.

7 K. Sumida, D. L. Rogow, J. A. Mason, T. M. McDonald, E. D. Bloch, Z. R. Herm, T.-H. Bae and J. R. Long, *Chem. Rev.*, 2011, **112**, 724–781.

8 A. C. McKinlay, R. E. Morris, P. Horcajada, G. Férey, R. Gref, P. Couvreur and C. Serre, *Angewandte Chemie International Edition*, 2010, **49**, 6260–6266.

9 S. S.-Y. Chui, S. M.-F. Lo, J. P. H. Charmant, A. G. Orpen and I. D. Williams, *Science*, 1999, **283**, 1148–1150.

10 A. Carné-Sánchez, I. Imaz, M. Cano-Sarabia and D. Maspoch, *Nat Chem*, 2013, **5**, 203–211.

11 M. Klimakow, P. Klobes, A. F. Thünemann, K. Rademann and F. Emmerling, *Chem. Mater.*, 2010, **22**, 5216–5221.

12 G. Majano and J. Pérez-Ramírez, *HCA*, 2012, **95**, 2278–2286.

13 G. Majano and J. Pérez-Ramírez, *Adv. Mater.*, 2013, **25**, 1052–1057.

14 A. J. Brown, N. A. Brunelli, K. Eum, F. Rashidi, J. R. Johnson, W. J. Koros, C. W. Jones and S. Nair, *Science*, 2014, **345**, 72–75.

15 J.-R. Li, J. Sculley and H.-C. Zhou, *Chem. Rev.*, 2012, **112**, 869–932.

16 J. Lee, O. K. Farha, J. Roberts, K. A. Scheidt, S. T. Nguyen and J. T. Hupp, *Chem. Soc. Rev.*, 2009, **38**, 1450–1459.

17 N. L. Rosi, J. Eckert, M. Eddaoudi, D. T. Vodak, J. Kim, M. O'Keeffe and O. M. Yaghi, *Science*, 2003, **300**, 1127–1129.

18 M. P. Suh, H. J. Park, T. K. Prasad and D.-W. Lim, *Chem. Rev.*, 2011, **112**, 782–835.

19 C. Petit, B. Mendoza and T. J. Bandosz, *ChemPhysChem*, 2010, **11**, 3678–3684.

20 T. A. Makal, J.-R. Li, W. Lu and H.-C. Zhou, *Chem. Soc. Rev.*, 2012, **41**, 7761–7779.

21 W. Zhou, *The Chemical Record*, 2010, **10**, 200–204.

22 C. Petit and T. J. Bandosz, *Advanced Functional Materials*, 2010, **20**, 111–118.

23 B. Xiao, P. S. Wheatley, X. Zhao, A. J. Fletcher, S. Fox, A. G. Rossi, I. L. Megson, S. Bordiga, L. Regli, K. M. Thomas and R. E. Morris, *J. Am. Chem. Soc.*, 2007, **129**, 1203–1209.

24 H.-C. Zhou, J. R. Long and O. M. Yaghi, *Chem. Rev.*, 2012, **112**, 673–674.

25 G. W. Peterson, D. K. Britt, D. T. Sun, J. J. Mahle, M. Browe, T. Demasky, S. Smith, A. Jenkins and J. A. Rossin, *Ind. Eng. Chem. Res.*, 2015, **54**, 3626–3633.

26 J.-R. Li, R. J. Kuppler and H.-C. Zhou, *Chemical Society Reviews*, 2009, **38**, 1477.

27 P. K. Allan, P. S. Wheatley, D. Aldous, M. I. Mohideen, C. Tang, J. A. Hriljac, I. L. Megson, K. W. Chapman, G. D. Weireld, S. Vaesen and R. E. Morris, *Dalton Trans.*, 2012, **41**, 4060–4066.

28 Z. R. Herm, R. Krishna and J. R. Long, *Microporous and Mesoporous Materials*, 2012, **151**, 481–487.

29 P. D. C. Dietzel, V. Besikiotis and R. Blom, *J. Mater. Chem.*, 2009, **19**, 7362–7370.

30 *Metal Organic Frameworks - 3D Model of NO Adsorption - http://www.youtube.com/watch?v=c3WkhgpCBTM*, 2012.

31 P. D. C. Dietzel, B. Panella, M. Hirscher, R. Blom and H. Fjellvåg, *Chem. Commun.*, 2006, 959–961.

32 P. D. C. Dietzel, R. E. Johnsen, H. Fjellvag, S. Bordiga, E. Groppo, S. Chavan and R. Blom, *Chem. Commun.*, 2008.

33 S. R. Caskey, A. G. Wong-Foy and A. J. Matzger, *J. Am. Chem. Soc.*, 2008, **130**, 10870–10871.

34 M. I. H. Mohideen, B. Xiao, P. S. Wheatley, A. C. McKinlay, Y. Li, A. M. Z. Slawin, D. W. Aldous, N. F. Cessford, T. Düren, X. Zhao, R. Gill, K. M. Thomas, J. M. Griffin, S. E. Ashbrook and R. E. Morris, *Nat Chem*, 2011, **3**, 304–310.

35 L.J. McCormick, S.A. Morris, M.J. McPherson, D.B. Cordes, A.M.Z. Slawin, S.J. Teat and R.E. Morris, *Manuscript in Preparation.*

36 H. Sato, W. Kosaka, R. Matsuda, A. Hori, Y. Hijikata, R. V. Belosludov, S. Sakaki, M. Takata and S. Kitagawa, *Science*, 2014, **343**, 167–170.

37 G. W. Peterson, G. W. Wagner, A. Balboa, J. Mahle, T. Sewell and C. J. Karwacki, *J. Phys. Chem. C*, 2009, **113**, 13906–13917.

38 J. B. Decoste, G. W. Peterson, M. W. Smith, C. A. Stone and C. R. Willis, *J. Am. Chem. Soc.*, 2012, **134**, 1486–1489.

39 J. B. DeCoste and G. W. Peterson, *Chemical Reviews*, 2014, **114**, 5695–5727.

40 J. Rouquerol, D. Avnir, C. W. Fairbridge, D. H. Everett, J. M. Haynes, N. Pernicone, J. D. F. Ramsay, K. S. W. Sing and K. K. Unger, *Pure and Applied Chemistry*, 1994, **66**, 1739–1758.

41 F. Tang, L. Li and D. Chen, *Adv. Mater.*, 2012, **24**, 1504–1534.

42 A.-H. Lu and F. Schüth, *Advanced Materials*, 2006, **18**, 1793–1805.

43 R. Luque, A. M. Balu, J. M. Campelo, M. D. Gracia, E. Losada, A. Pineda, A. A. Romero and J. C. Serrano-Ruiz, in *Catalytic applications of mesoporous silica-based materials*, 2012.

44 A. Corma, *Chem. Rev.*, 1997, **97**, 2373–2420.

45 R. S. Franchi, P. J. E. Harlick and A. Sayari, *Ind. Eng. Chem. Res.*, 2005, **44**, 8007–8013.

46 S.-N. Kim, W.-J. Son, J.-S. Choi and W.-S. Ahn, *Microporous and Mesoporous Materials*, 2008, **115**, 497–503.

47 Y.-K. Seo, J. W. Yoon, U.-H. Lee, Y. K. Hwang, C.-H. Jun and J.-S. Chang, *Microporous and Mesoporous Materials*, 2012, **155**, 75–81.

48 S. Galli, N. Masciocchi, V. Colombo, A. Maspero, G. Palmisano, F. J. López-Garzón, M. Domingo-García, I. Fernández-Morales, E. Barea and J. A. R. Navarro, *Chem. Mater.*, 2010, **22**, 1664–1672.

49 Z. Li and H. C. Zeng, *J. Am. Chem. Soc.*, 2014, **136**, 5631–5639.

50 A. R. Millward and O. M. Yaghi, *J. Am. Chem. Soc.*, 2005, **127**, 17998–17999.

51 M. J. Katz, A. J. Howarth, P. Z. Moghadam, J. B. DeCoste, R. Q. Snurr, J. T. Hupp and O. K. Farha, *Dalton Trans.*, 2015.

52 M. I. H. Mohideen, B. Xiao, P. S. Wheatley, A. C. McKinlay, Y. Li, A. M. Z. Slawin, D. W. Aldous, N. F. Cessford, T. Düren, X. Zhao, R. Gill, K. M. Thomas, J. M. Griffin, S. E. Ashbrook and R. E. Morris, *Nat Chem*, 2011, **3**, 304–310.

Chapter 2 Experimental Techniques.

2.1.Summary

This chapter details the theoretical basis behind the experimental and analytical techniques applied during the course of this project. Briefly, X-ray diffraction was used to compare produced materials with known patterns to confirm formation of the desired material and to monitor the effects of gas sorption on MOFs. Gas adsorption was used to confirm viability of samples prior to testing and also as a comparison to published data. Electron microscopy was used to determine distribution of different materials in composite materials and supplemented with EDX and ICP-MS to obtain information on the ratios of compounds present in hybrid materials. FTIR, TGA and NMR were used to determine bonding states of atoms during gas sorption and to examine the interactions between the MOFs and the adsorbed gases. Ball milling and particle size analysis were used to obtain a more consistent material for use in synthetic procedures.

2.2. X-Ray Diffraction

X-ray diffraction[1] is a technique used to identify the phases of a crystalline material rapidly. This relies on constructive interference of monochromatic x-rays that diffract from a crystalline solid. Crystalline substances function as 3-dimensional diffraction gratings for radiation at the x-ray wavelength, which are in a very similar range to the spacing of planes in a crystalline lattice (of the order of 1-10 Å). When an X-ray strikes an atom at a given angle (θ), it is scattered at an equal angle, as shown in Figure 6. As x-rays are diffracted by multiple atoms within the crystal, each a different distance from the x-ray source, the diffracted x-rays exiting the crystal have all travelled different distances and are no longer necessarily in phase with each other. Interference between the diffracted x-rays results in a diffraction pattern, which is observed using a detector that measures the intensity of x-rays striking its surface. When the difference in the distance travelled by the x-rays is an integer (1,2,3 etc) multiple of the wavelength of the x-ray, constructive interference occurs and the x-rays are detected by the detector. When the distance travelled is not an integer multiple, of the wavelength, destructive interference occurs and the x-rays effectively cancel each other out.

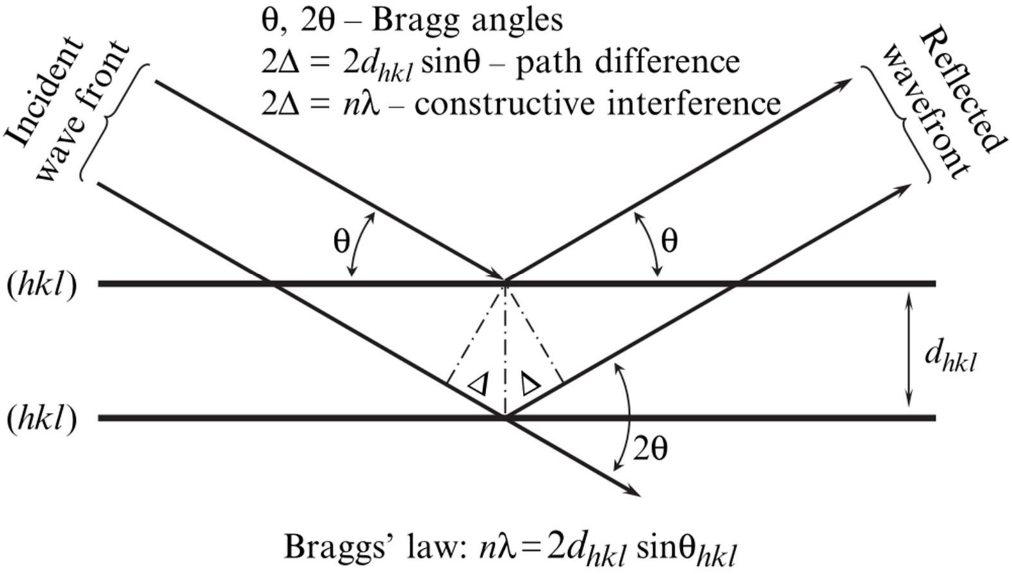

Figure 6: Bragg Diffraction[1]

The benefits of using powder x-ray diffraction in this way is that it is a fast and non-destructive method to determine the structure of a crystalline solid, particularly those which are not easy to elucidate by methods such as NMR or IR spectroscopy.

2.2.1. X-Ray Crystallography

A crystal structure is defined as a regular, repeating sequence of atoms or ions within a lattice that exhibits long range order and symmetry. The asymmetric unit is the smallest repeating unit of a given compound. The unit cell of a crystal structure is the smallest segment of the structure from which the complete structure may be generated purely by translation of the segment in three dimensions. There are four categories of unit cell which are distinguished by the position of the lattice points of the unit cell. Unit cells with lattice points located only at the eight corners of the unit cell are described as primitive (P) cell. An additional point in the centre of the unit cell is described as body centered (I) and an additional points on the centre of the faces of the unit cell are described as face centered (F). Finally the cells with designation A, B or C centred, which have two additional points on a pair of parallel faces of the cell, with A, B or C indicating on which pair of faces the additional points are located.(B is shown below: Figure 7).

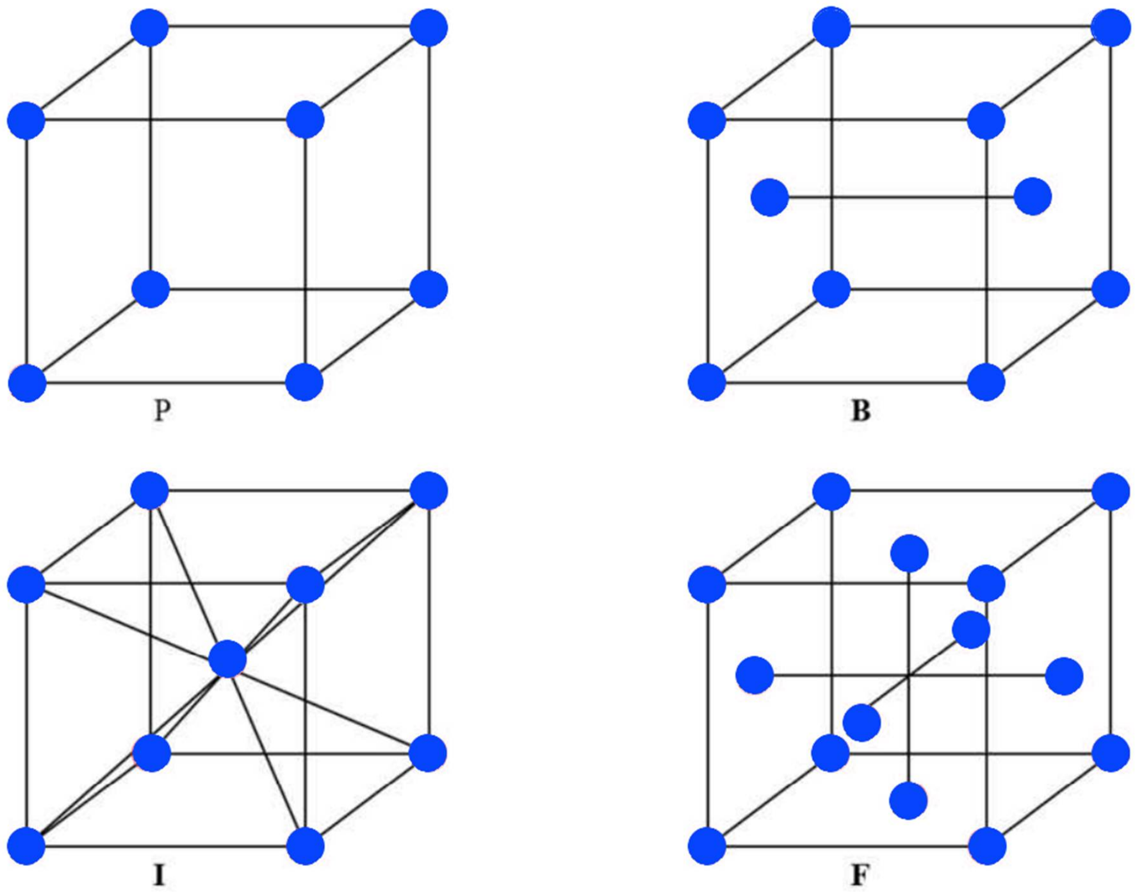

Figure 7: Basic Crystal Lattices

Unit cells have a series of parameters that define them based on the lengths of the edges of the cells (*a, b* and *c*) and the angles at the edges of the cell (α,β and γ). Table 1 shows the six crystals systems that are possible with this array of variables.

Table 1: Crystal Systems

Crystal System	Lengths	Angles
Triclininc	a ≠ b≠ c	α ≠β ≠ γ ≠ 90°
Monoclinic	a ≠b ≠ c	α = γ = 90° β ≠ 90°
Orthorhombic	a ≠ b ≠ c	α = β = γ = 90°
Tetragonal	a = b ≠ c	α = β = γ = 90°
Hexagonal/Trigonal	a = b ≠ c	α = β = 90° γ = 120°
Cubic	a = b = c	α = β = γ = 90°

2.2.2. Powder X-Ray Diffraction

In many samples, single-crystal diffraction is rendered impractical or impossible by the small size of the crystallites in many inorganic materials. In these cases, powder x-ray diffraction can be used to determine the structure of the material. In contrast to the single-crystal method which relies on a single crystal with a known orientation, PXRD relies on all possible orientations of a crystal being represented in a powdered sample. Through the averaging effect this produces, a one-dimensional diffraction pattern may be obtained which contains information about the internal structure of the material (Figure 8).

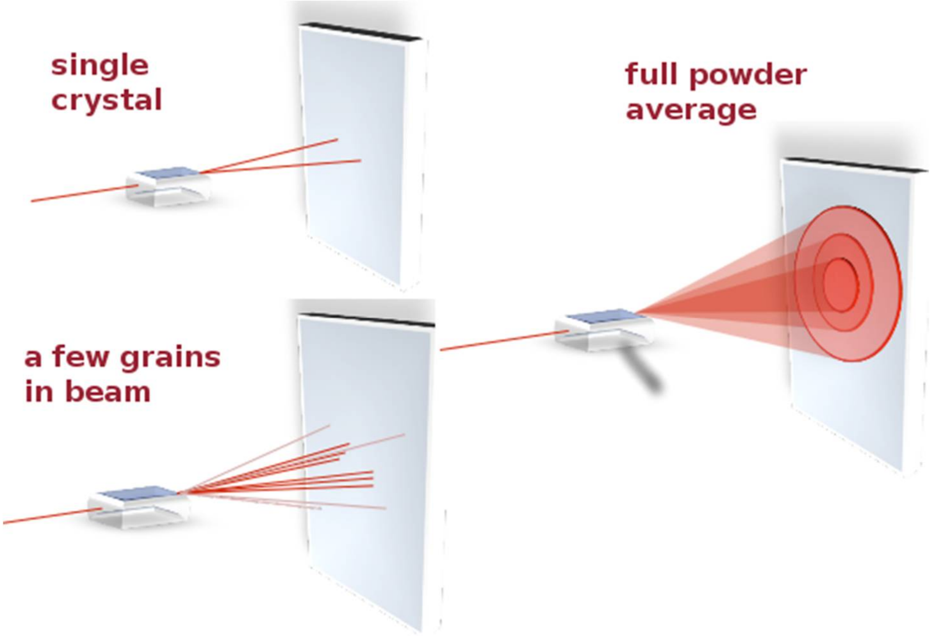

Figure 8: Schematic showing the difference between single crystal and powder diffraction. Since the crystallites are effectively at all possible orientations, concentric rings are seen instead of individual spots.[2]

Typically a small sample of material is placed on a disc (usually Teflon or stainless steel), or into a glass capillary and then rotated while it is exposed to x-rays over a range of angles, which are designated θ. The resulting pattern is collected to give a series of peaks.

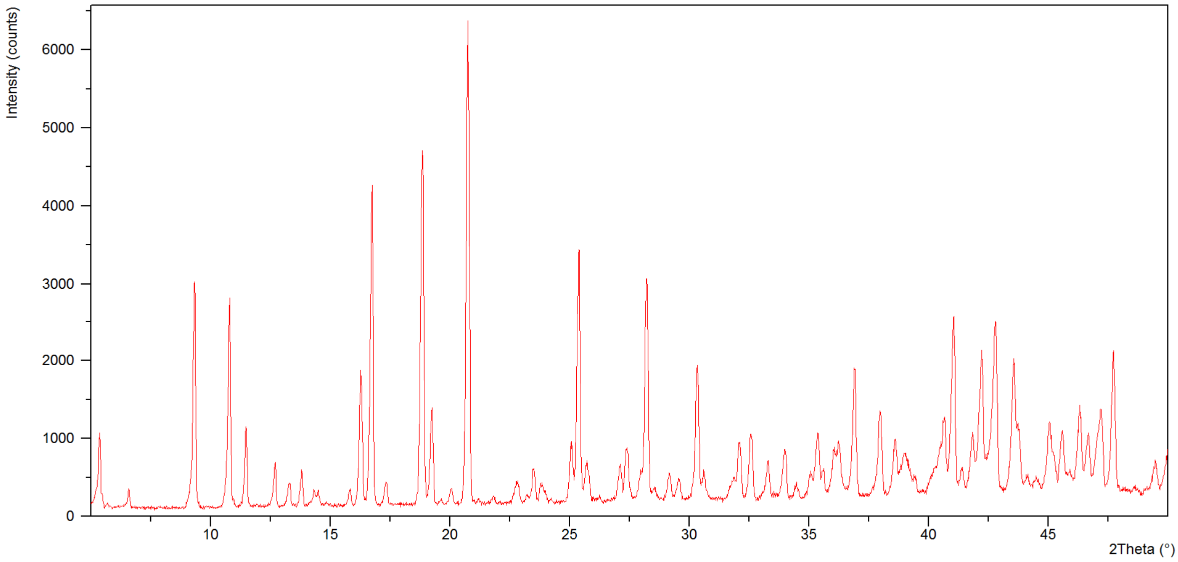

Figure 9: A typical MOF powder pattern. The PXRD pattern of STAM-1 with HKUST-1 contamination. The y-axis indicates the intensity of the peaks and the x-axis indicates the 2ϴ angle at which the peak appears.

The important data that can be obtained from a PXRD pattern includes the 2θ values at which the peaks occur, which gives information about the d-spacings between the atoms, and can be used to determine the unit cell of the material and the intensity of the peaks within the pattern which gives information on the location of electrons and therefore the atoms within the unit cell.

If the single crystal structure of a material is known, it can be used to generate a predicted powder pattern. This is useful for phase identification of materials where contaminants or other structures may be present in a mixture of powders. For example, the pattern shown in Figure 9 was obtained from a sample of STAM-1 that is contaminated with a small amount of HKUST-1. By comparing the predicted pattern for STAM-1 (shown in black in Figure 10, the extraneous peaks in Figure 9 may be identified and compared to the PXRD patterns of other materials to determine the nature of the contaminant.

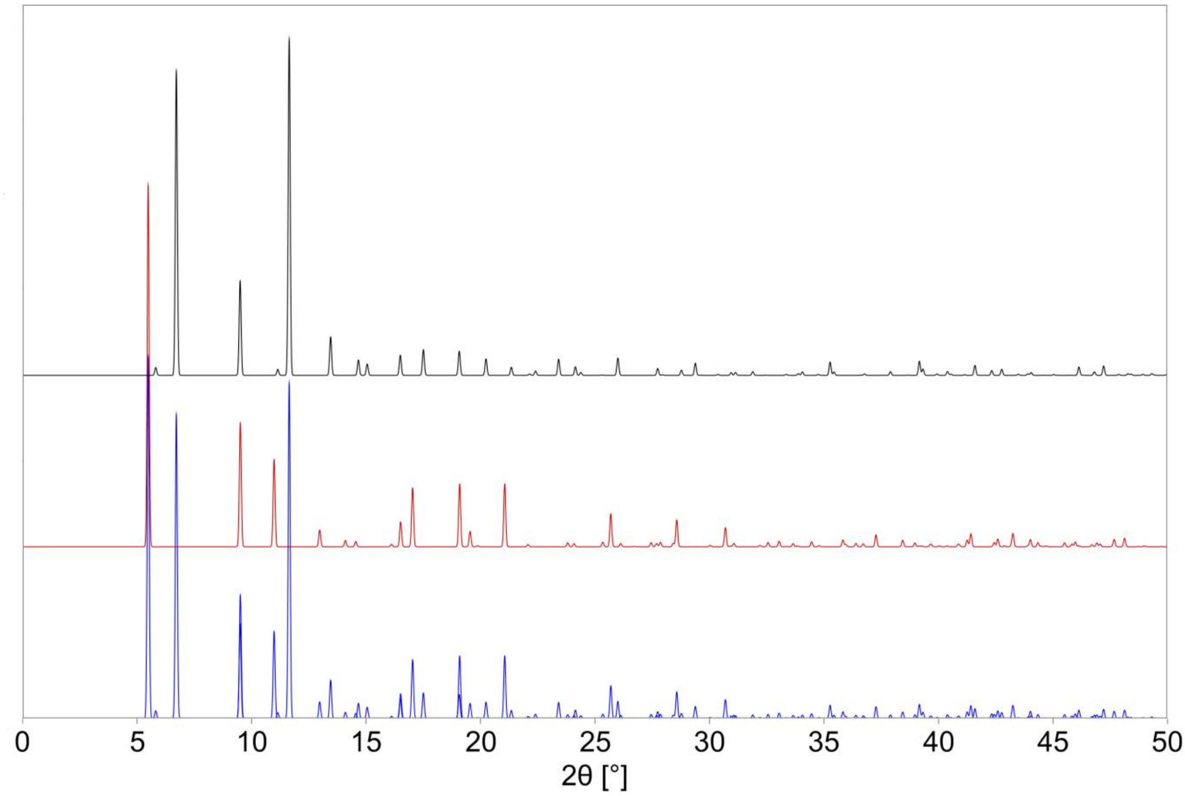

Figure 10: Simulated Powder patterns of STAM-1 (black) and HKUST-1 (red) and as-synthesised STAM-1 with HKUST-1 contamination (blue).

2.2.3. Variable Temperature PXRD

Variable temperature PXRD applies all of the principles described above combined with the ability to control the atmosphere and temperature that the sample experiences while it is being subjected to x-ray bombardment. The apparatus used for these studies described in this thesis is a PANalytical Empyrean Mo X-ray tube ß-filter (Mo Kα 1, 2) X'celerator with RTMS detector. This is capable of observing samples from room temperature to 1173K in vacuo or at pressures of up to 100 bar of inert gas. MOFs often incorporate solvent molecules into their structure and when heated in vacuum, solvent molecules may be evacuated from the pores and, at higher temperatures, the structure, causing a visible change in the PXRD pattern generated by the compound.

While less directly useful in observing the changes in the structure of the compound than single crystal, it allows for screening of compounds that have phase changes that cannot be observed by single-crystal diffraction. The change of phases observed under vacuum and elevated temperatures.

2.3. Gas Adsorption Techniques

This section will briefly discuss the theory of gas adsorption.[3,4]

2.3.1. Langmuir Theory

First posited in 1916 by Irvine Langmuir, his theory of gas adsorption is used as a method to characterise the number of vacant sites on a surface for gas molecules to adhere to. It makes several assumptions; that all adsorption sites are equivalent over a uniform surface, that only a monolayer of gas is adsorbed onto the available surface, and that none of the adsorbed molecules have any interactions with one another.

When measuring Langmuir adsorption in a porous material, adsorption is presented as an equilibrium wherein a gas molecule strikes a surface where there is an active site, briefly adheres to the surface then evaporates. The collision between the gas molecule and the surface is considered to be inelastic, and the molecule does not return immediately to the gas phase. This event is considered to be an adsorption and this is characterised by Equation 2-1

$$V_a = \frac{V_m bP}{1 + bP}$$

Equation 2-1

V_a is the quantity of gas in cm^3 at pressure P and b is an empirical constant. V_m represents the quantity of gas in cm^3 that, once adsorbed, will produce a monolayer.

This equation can be rearranged to give a linear equation that gives a straight line when P/V_a is plotted against P (Equation 2-2). At the cryogenic temperatures used in typical isotherms, the plot will only have a straight line in certain areas, however b and V_m can still be calculated from the gradient and y-intercept of the straight line segments.

$$\frac{P}{V_a} = \frac{1}{bV_m} + \frac{P}{V_m}$$

Equation 2-2

From this information, the specific surface area of the material, *s*, which represents the surface area of a gram of material, can be calculated using V_m from Equation 2-3

$$s = \frac{V_m \sigma N_A}{m V_o}$$

Equation 2-3

In this equation, σ represents the surface area in m^2 occupied by a single gas molecule that has adsorbed onto the surface of the material. For nitrogen, $\sigma = 1.62 \times 10^{-9}$ m^2, but others gases such as CO_2 can be used in the same manner and by substitution of the relevant gas molecule surface area. N_A represents Avogadro's number, m is the mass of the sample being tested for adsorption in grams and V_o is the molar volume of the gas in cm^3. For ease of calculation, it is assumed that gas used behaves as an ideal gas and this molar volume is treated as 22414 cm^3.

The original Langmuir theorem was improved by Brunauer, Emmett and Teller giving rise to the BET theory which allows calculation of surface areas where multi-layered adsorption is taking place. It operates by assuming that the same forces responsible for condensation of gases have an effect on the binding energy in multi-layer adsorption. Based on this, the rate of condensation of the gas onto an already monolayer-covered surface as being equal to the rate of evaporation from the monolayer Calculating for an infinite number of layers, Equation 2-4 may be derived, where C is a constant, P_0 is the saturation pressure of the gas being used and V_m and V_a are as described in the Langmuir theory section.

$$\frac{P}{V_a(P_0 - P)} = \frac{1}{V_m C} + \frac{C-1}{V_m C}\left(\frac{P}{P_0}\right)$$

Equation 2-4

From this, we can plot $P/V_a(P_0-P)$ vs P/P_0, giving a straight line with an intercept of $1/V_mC$ and a slope of $(C-1)/V_mC$.

The constant C allows the calculation to apply to more than one layer and is described in Equation 2-5.

$$C \propto exp\frac{q_l - q_L}{RT}$$

Equation 2-5

The values that compose C are $q_{l,}$ which is the heat of adsorption of the initial layer of gas molecules, q_L is the heat of liquefaction of nitrogen. R represents the gas constant and T the temperature. The surface area can be calculated using Equation 2-6, where S_{total} is the total surface area, ϑ_m is the volume of the adsorbate gas, N is Avogadro's number, s is the cross section of the adsorbate gas and V is the molar volume of the adsorbate gas.

$$S_{total} = \frac{(\vartheta_m N s)}{V}$$

Equation 2-6

The specific surface area, S_{BET} can then be obtained by Equation 2-7, where a represents the weight of the sample that was analysed.

$$S_{BET} = \frac{S_{total}}{a}$$

Equation 2-7

To calculate surface areas using BET theory, data points from the pressure range of 0.05 to 0.3 are used in traditional samples, which operate under the assumption that the formation of the monolayer of gas occurs is complete above this pressure range. Research to compare simulated models of gas uptake by Grand Canonical Monte Carlo simulation and comparison with existing isotherms of MOFs[5] suggests that due to their highly porous nature, MOFs form a monolayer at much lower pressures than originally determined for non-porous solids. As a result, calculations made using data from below 0.01 atmospheres produces surface areas that better match simulated surface areas in MOFs. Samples presented in this thesis were examined using the original 0.05-0.3 pressure range.

2.3.2. Physisorption and Chemisorption

When gases are adsorbed onto a surface, one of two different types of adsorption can occur, chemical adsorption (chemisorption) or physical adsorption (physisorption).

Chemisorption[6] occurs when a reaction takes place, transferring electrons between adsorbent and gas and results in the formation of a new chemical bond. This is a relatively slow process as the energy barrier for activation must be overcome before adsorption can occur. The required energy for chemisorption to take place is of the same magnitude as the heat of chemical reactions e.g. the heat of physical adsorption of nitrogen onto the surface of an iron catalyst is ~5.69kJ mol^{-1}, while the heat of chemisorption is ~146kJ mol^{-1}. [6] At these energies, the atoms of the gas molecules create a bond to the surface, forming a monolayer, upon which further reaction cannot take place.

In contrast, physisorption is a much more rapid process. Physisorption is the result of dispersive and electrostatic interactions taking place between an adsorbent surface and a gas molecule. When the atoms move close enough to interact, induced dipoles are formed and the gas molecule is adsorbed to the surface with a heat of adsorption equivalent to the heat of gas vaporisation. For example, the $\Delta_{vap}H$ of N_2 is 5.57kJ mol^{-1}. Gas molecules are adsorbed at the same rate as they are desorbed onto the surface, with the shape of the resulting isotherm giving information regarding whether this is a monolayer or multilayer adsorption of the gases. Physisorbed gases are not strongly bound to the surface they interact with and can often be easily removed by reducing the pressure to below the pressure at which the adsorption took place, and the gas molecule can then easily move away from the surface.

2.3.3. Water Adsorption

Water adsorption[4] is measured using a gravimetric method as opposed to the volumetric methods described above. These experiments were carried out at Dstl, Porton Down using a DVS Advantage 2. All experiments involving water adsorption took place at room temperature. A sample of the solid is placed on a sensitive microbalance. The chamber surrounding the microbalance can then be evacuated and the temperature controlled in order to remove residual solvent and in the case of MOFs, solvent bound to metal-centres and in the pores of the material.

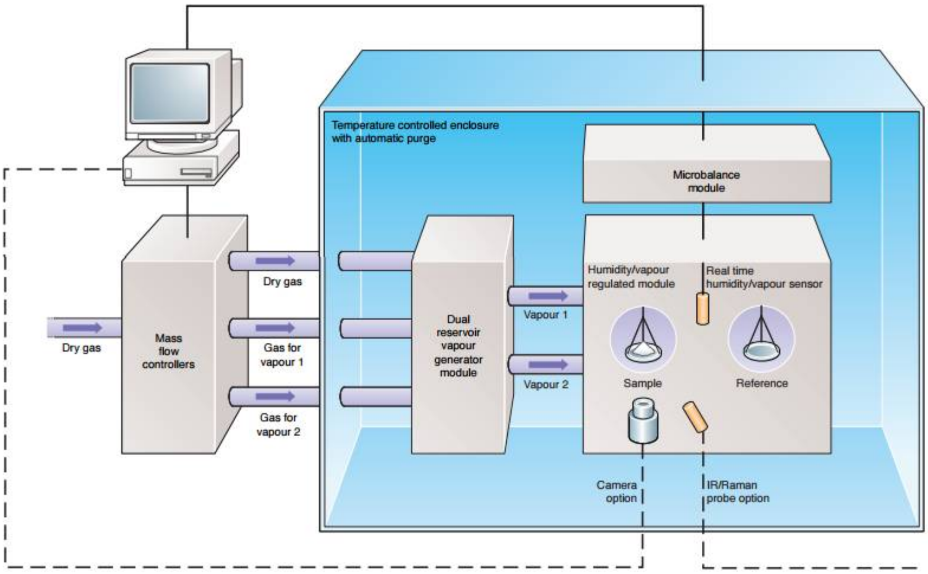

Figure 11: Schematic Diagram of DVS Advantage 2 Gravimetric Analyser used at Dstl. Figure courtesy of Surface Measurement Systems.

Once the sample is desolvated, the humidity of the chamber is raised to reach a target level and the change in weight of the sample measured over time. Equilibration for a given humidity is assumed to be reached when the rate of mass change detected by the microbalance is less than 0.002%/min. As a result of this method of determining uptake equilibrium, experiments proceed at a much slower pace than that typical of volumetric experiments.

2.3.4. Ammonia Breakthrough

Microbreakthrough is a quantitative method used to determine how long a given material will offer protection from a harmful substance. In its simplest form, breakthrough testing involves the creation of a solid plug of material through which a challenge gas of known concentration is flowed. An appropriate sensor measures the concentration in the exhaust gas. The breakthrough point is considered to be when the level of challenge gas in the atmosphere flowing out of the sample plug begins to rise above the background level (< 1 ppm).

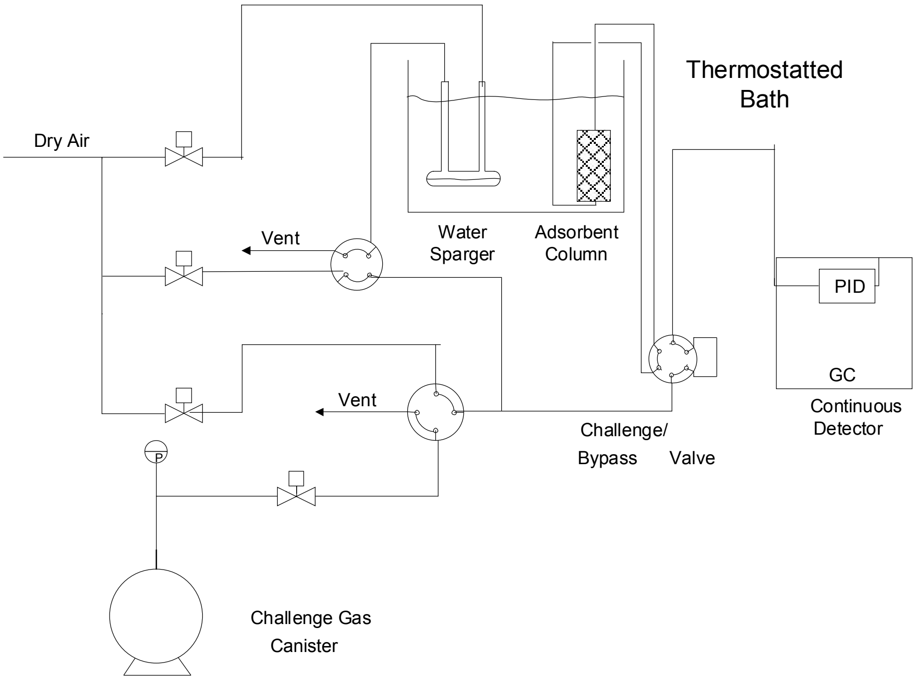

Figure 12: Advanced Breakthrough Apparatus with IR Monitoring of Breakthrough. Schematic provided by Gregory Peterson.

Breakthrough data is primarily used to calculate the dynamic capacity to saturation of a given material.[7] The concentration time (Ct_{feed}) which is described in units of mg min/m^3 is defined in Equation 2-8. C_{feed} is the concentration of the feed in mg min/m^3 is and t_f is the time the feed has flowed into the sample.

$$Ct_{feed} = t_f C_{feed}$$

Equation 2-8

The concentration of the challenge gas eluting from the sorbent during adsorption is calculated by integration underneath the elution curve with application of the mid-point approximation method (Equation 2-9). $Ct_{elution}$ is the concentration of challenge gas being eluted and has units of mg min/m^3, Ct_n is the concentration at time n, Ct_{n-1} is the concentration at the previous time and ts indicating the saturation time of the material.

$$Ct_{elution} = \sum_{t=0}^{ts} \frac{C_n + C_{n-1}}{2}(t_{n-1} - t_n)$$

Equation 2-9

The total effective loading to saturation (W_e) is calculated using Equation 2-10.

$$W_E = \frac{(Ct_{feed} - Ct_{elution})F_{feed}}{M_{ads}MW}10^{-6}$$

Equation 2-10: Calculation of effective loading at saturation for a given sample.

Equation 2-10 can also account for off-gases from the sample after discontinuation of the flow of effluent by subtracting it from the Ct values. This was not done with any of the samples tested in this thesis.

In order to produce an accurate breakthrough time for a given sample of material, corrections based on environmental factors must be made: the weight of the sample, the initial time taken for the challenge gas to permeate throughout the system, adsorption capacity for materials used to mount the samples in place (i.e. cotton wool adsorbs some ammonia whereas glass wool does not), and the time taken for the system to reach equilibrium (i.e. effluent concentration equals influent concentration of the challenge gas). Microbreakthrough experiments were conducted at Dstl Porton Down and Edgewood Chemical and Biological Centre.

2.4.Infrared Spectroscopy

Infrared (IR) Spectroscopy[8] operates by measuring the adsorption by a sample in the infrared portion of the electromagnetic spectrum, which has a lower frequency and longer wavelength than visible light. This technique is commonly used in the identification of compounds by passing IR radiation through a sample of the compound and measuring the intensity of transmitted light. This method can be employed on solids, liquids and gases. Originally, in order to prepare a sample for IR spectroscopy, solid materials are typically pressed into a disc with a suitable salt that displays minimal infrared absorbance such as potassium bromide. A quantity of sample is mixed with the salt and pressed into a thin disc, which is then mounted in an IR spectrometer and has a variety of wavelengths of IR light passed through it. The transmitted light is measured by a detector and from this a spectrum is built, showing the absorbance (0-100%) by the sample over a given wavelength range (given as wavenumbers in cm^{-1}).

In the case of liquid samples that are not capable of being pressed into a disc, the sample is mixed with oil to form a mull which can then be placed between salt (e.g. NaCl or $CaCl_2$) plates and analysed. The most commonly used oil is Nujol which has well defined bands in the IR spectrum.

Different functional groups absorb different wavelengths of light, so it is possible to determine which functional groups are present in a given sample by the location of the absorption peaks. The bonds adsorb energy in the form of IR radiation the radiation has the same energy as that of a deformation (stretching, wagging etc.) frequency of the bond.

As radiation with this energy passes through the sample, it is absorbed, resulting in the bands of the IR spectra.

To calculate the stretching frequency of a diatomic molecule Equation 2-11 can be used.

$$\bar{\upsilon} = \frac{1}{2\pi c}\left[\frac{f(m_1 + m_2)}{m_1 m_2}\right]^{1/2}$$

Equation 2-11: Calculation of the stretching frequency of a diatomic molecule.

In this equation, m_1 and m_2 are the mass of the two atoms involved in the stretching and bending, f is the force constant (Nm^{-1}), c is the speed of light and $\bar{\upsilon}$ is the wavenumber (cm^{-1})

2.5. Electron Microscopy

2.5.1. Scanning Electron Microscopy

Scanning electron microscopy (SEM)[9] is an analytical technique that allows for imaging of small particles by the use of a focussed beam of electrons, which is directed at the sample. There are numerous ways to image a material using this method, which include detecting back-scattered electrons and characteristic X-rays but the most common method is secondary electrons detectors, which are universal in SEM apparatus. The secondary electrons are used to produce very high resolution images of particles, down to 1nm, an effective magnification of roughly 500,000x.

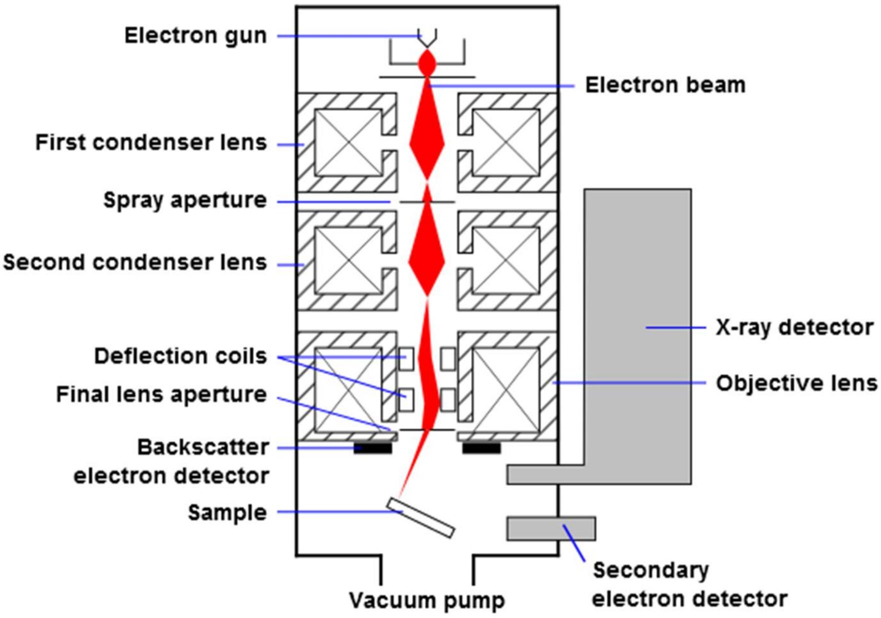

Figure 13: Diagram of an SEM Apparatus

2.5.2. Scanning Transmission Electron Microscopy

It is also possible to use SEM to "see through" thin samples using a detector placed below the sample. The electrons that pass through the material strike the detector and give an image indicating the internal structure of the sample. This technique is called scanning transmission electron microscopy.

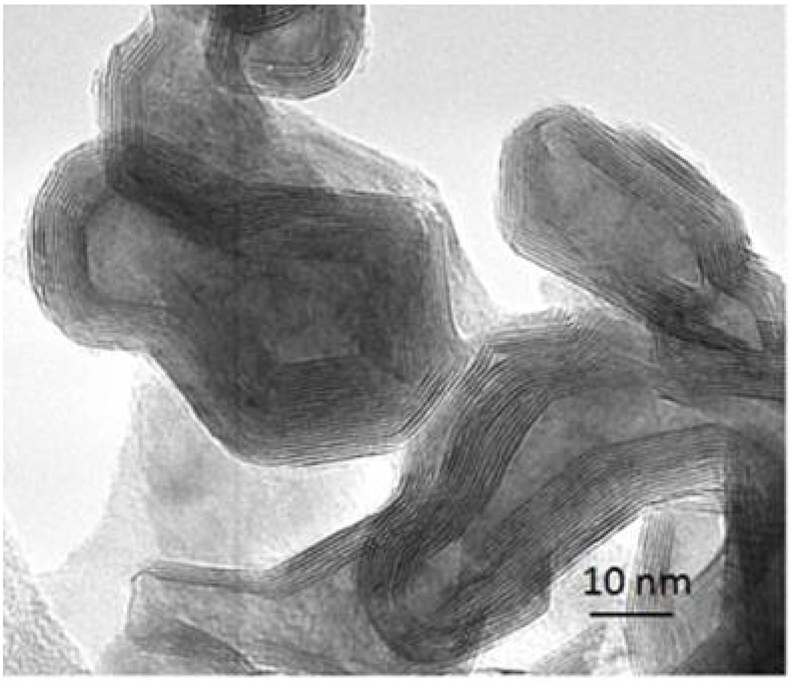

Figure 14: Scanning Transmission Electron Micrograph of a hollow silica nano-particle.[10]

Figure 14 shows the effect of using STEM, which allows us to see through the outer shell of this silica nanoparticle, showing us that the interior is hollow. This can also be used to view materials loaded inside hollow particles.

2.5.3. EDX

Energy Dispersive X-ray spectroscopy (EDX) is a technique that is used in conjunction with SEM as a form of elemental analysis. A high energy stream of electrons is directed at a sample, causing electrons to become excited to higher energy levels. These electrons emit X-rays as they relax back to their ground state. The wavelengths of the emitted X-rays are specific to the type of atom that emits them due to the energy gaps between electron shells being unique in different atoms, making it possible to quantify the composition of the sample. By measuring the energy and number of X-rays emitted, it is possible to determine which elements are emitting and thus the composition of the sample. The technique is limited in that it can only give the amount of a given element as a ratio, relative to the amount of other elements present.

2.6. Nuclear Magnetic Resonance Spectroscopy

Nuclear Magnetic Resonance (NMR) [11,12] spectroscopy is a form of absorption spectroscopy where molecules are placed in a strong magnetic field and bombarded with radio waves which are absorbed by the nuclei. This causes changes in the nuclear spin states of the nuclei, which can be measured and used to determine the bonding states of certain atoms that make up a molecule. Only certain atoms can be analysed in this way: an isotope of an atom must have an uneven number of nucleons (protons and/or neutrons), which causes the atom to have an intrinsic magnetic moment and angular momentum. This is described as having a non-zero spin. By placing isotopes which exhibit non-zero spin into a strong magnetic field, the spins polarise, as shown in Figure 15.

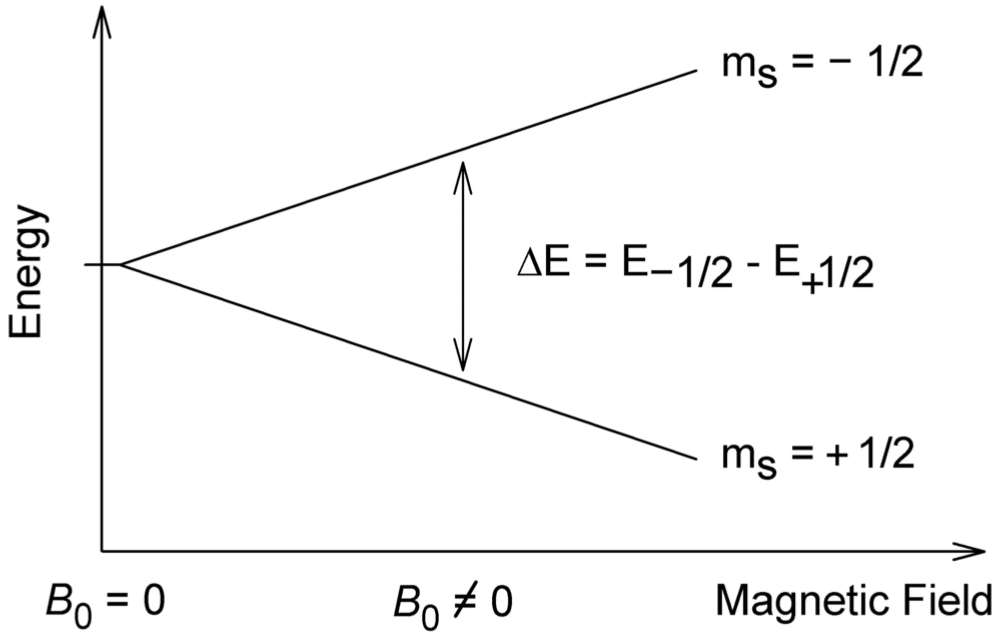

Figure 15: Effect on energy levels of the nucleons of an atom when a strong magnetic field is applied.

As shown in the diagram above, the splitting of the energy levels is a function of the strength of the magnetic field B_0.

The atoms most typically investigated are ^1H and ^{13}C, which both have a spin of ½ ^{12}C has a net spin of 0 and as such, is not NMR active. While ^1H has abundance of 99.985%, ^{13}C has only has a natural abundance of 1.1% and, as such, a strong magnetic field is required to create sufficient splitting of the energy levels to be able to detect the atoms. ^{19}F NMR was also used briefly in this project and is similar to ^1H NMR due to the 100% abundance of ^{19}F.

2.7. Solid State ^{13}C NMR

Due to the supramolecular structure of MOFs, if they dissolve in a solvent, they are no longer a MOF and as such NMR data gathered on "dissolved" MOF does not have any information regarding the MOF structure. The use of solid-state NMR allows us to examine the MOF without the use of solvents and gain an understanding of the local structure of the ligands that make up MOFs in the solid phase.[13–15]

2.7.1. Magic Angle Spinning

NMR in the solid phase typically produces very broad peaks, making it difficult to identify individual signals. This is due to the inability of the atoms in the solid to rapidly reorient as happens in a liquid sample. This sharply limits the usage of NMR to samples that were soluble or could be melted into a liquid. In order to overcome this, the solid is typically spun at speeds ranging from 1-100 kHz and at the "magic angle" of 54.74° with respect to the direction of the magnetic field.

The "magic angle" was first reported in the late 1950s, with the term itself being coined in 1960. It was reported that spinning a crystal in a magnetic field worked to mimic the effect of the molecules rapidly reorienting themselves as they would in a solution, causing the nuclear dipole-dipole interactions to average to near zero and reducing the nuclear-quadrupolar interactions substantially. Solid-state NMR allows for the investigation of supramolecular materials which would break down or be affected by the use of solvent.

One side-effect of the use of MAS NMR is the presence of spinning sidebands. These are sharp peaks which spread out from the peak present as a result of isotropic chemical shift. They are spaced apart at the spinning rate and as such change position depending on the speed at which the sample is rotated. Spinning sidebands can be used to determine anisotropic interactions that are averaged by magic-angle spinning. Due to the speed of MAS rotation used on the samples investigated in this thesis, the spinning sidebands were reduced to the point of being indistinguishable from the background noise of the spectra.

2.7.2. Decoupling and Pulse Sequences

While decoupling, where a sample is irradiated at a specific frequency to eliminate nuclear coupling, is commonly used to in ^{13}C NMR, it is not normally necessary in paramagnetic compounds examined by fast MAS. The fast spin-rate removes the majority of the heteronuclear dipole interactions and line broadening exhibited is usually the result of interactions with unpaired electrons, rather than other nuclei.[16,17]

For the direct polarisation NMR's described in this thesis, the spin-echo pulse sequence was used, to overcome the effects of a short relaxation time present in paramagnetic materials. After the pulse is applied, there is a short period, referred to as "dead time", where the initial pulse can still be detected (known as "pulse ringing") and as a result, will distort the signal The spin-echo pulse sequence operates by applying a 90° pulse the after a relaxation time, τ, a pulse is applied at 180°. The second pulse inverts the magnetisation and after a further delay, the FID can be collected .This is shown in Figure 16.

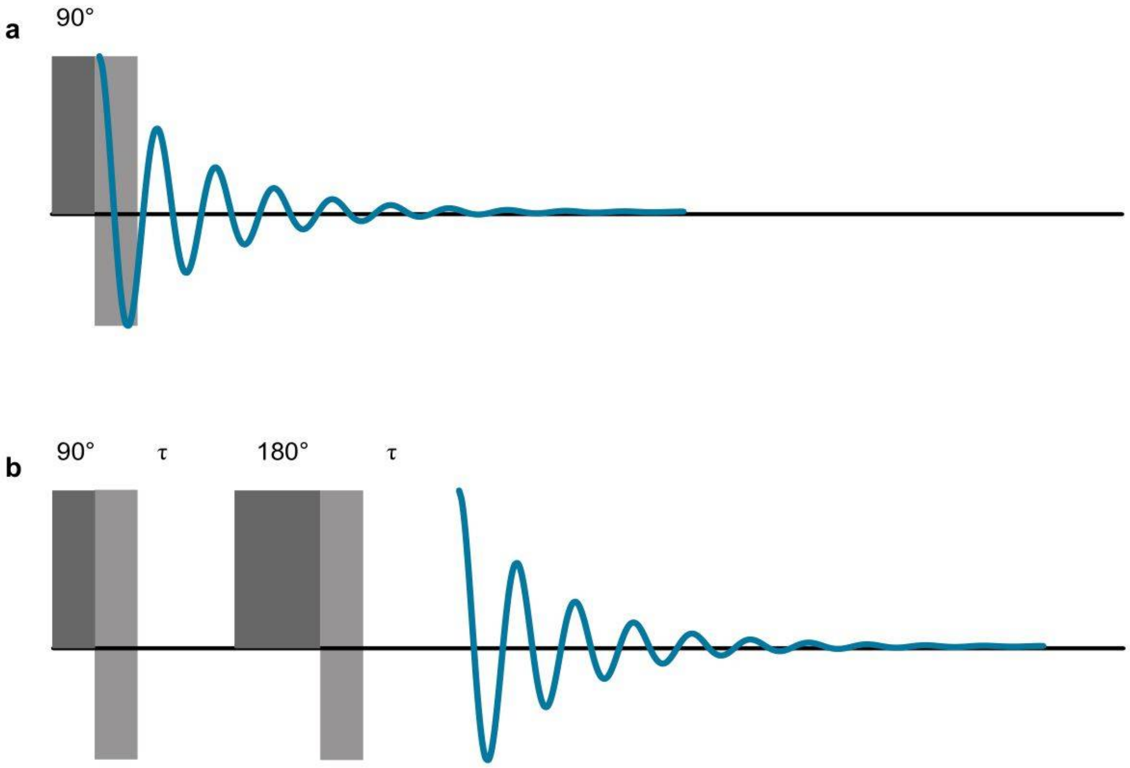

Figure 16: Diagram showing the effect of pulse ringing (a) where the signal is lost in the dead time and the effect of the spin-echo pulse sequence (b) which delays the signal allowing it to be collected in full without distortion by pulse ringing. Diagram kindly supplied by Daniel Dawson and Charlotte Sansome.

Further advantages of the spin-echo experiment include the removal of the background signal, which has a high degree of prominence in natural abundance ^{13}C NMR spectra, particularly in MOFs as the signal is typically weak and spread across the spinning side-band manifold. Due to rapid transverse relaxation of these samples, the echo delay is kept to a minimum by use of rapid MAS in the range of 30-80 kHz which has a rotor period of between ~12.5-33 μs which minimises the signal lost. [18]

2.7.3. Cross Polarisation

Cross-polarisation (CP) is a technique[19] which is used to improve the sensitivity of nuclei such as ^{13}C which have a low natural abundance and low gyromagnetic ratio (γ), by transferring magnetisation from a nuclei with a higher γ and abundance to the nuclei being investigated. This also has the effect of decreasing the T_1 and T_2 relaxation times, allowing for scans to be repeated more rapidly, falling from relaxation times on the order of minutes to seconds and below, allowing for greater fidelity of data by increasing the number of scans. CP can also be used for spectral editing purposes. The experiment is conducted by locking of the spins using a contact pulse which allows the nucleus being investigated to derive its magnetisation from the network of nearby abundant spins, typically ^{1}H, but any abundant nucleus of spin -1/2 can be used. The main drawback with the use of CP is that it cannot be considered to be a quantitative measurement, as the carbon atoms are not all magnetised to the same degree.

This technique can be combined with magic angle spinning which allows for superior analysis of solid-phase materials with low abundance nuclei. In the case of the MOFs investigated in this thesis, CP was not generally applied, due to the presence of paramagnetic copper atoms in the samples, which greatly reduce the relaxation time of ^{13}C atoms, eliminating the need for the pulse sequence to be applied. It does however have use in distinguishing between carbon atoms with different levels of bonding to ^{1}H which allows for distinction between different types of carbon atom present in the sample, e.g. between a CH_2 group and a quaternary carbon, as the CH_2 group will magnetise more rapidly than the quaternary carbon, allowing the distinction to be made. CP was used to assign the carbon atoms of MOFs that exhibit a structural shift when dehydrated.

2.7.4. NMR Data Acquisition

Solid-state NMR spectra were acquired using Bruker Avance III spectrometers at a B_0 field strength of 9.4 or 14.1 T (^{1}H Larmor frequencies of 400 and 600 MHz respectively). For spectra acquired at 9.4 T, zirconia MAS rotors with an outer diameter of 1.9 mm were packed with sample and rotated up to rates of 40 kHz. For spectra acquired at 14.1 T, samples were packed into zirconia MAS rotors with an outer diameter of 1.3 mm and rotated at speeds up to 60 kHz. Spectra were recorded using a rotor-synchronised spin-echo sequence, with an echo interval of one rotor period (typically 17 – 27 ms). The radiofrequency field strength for all experiments was $\omega 1 /2\pi = 100$ kHz. The relaxation constants, T_1 and T_2, were measured using inversion recovery and spin echo experiments, respectively. L -alanine was used as the chemical shift reference with the methyl resonance at 20.5 ppm in the ^{13}C NMR spectrum and the amine resonance at 8.5 ppm in the 1 H spectrum.

2.8. Thermogravimetric Analysis

Thermogravimetric analysis (TGA)[20] is a method for the measurement of the change in mass of a given sample as a function of temperature, using a selected controlled atmosphere. This method gives a quantitative measurement of the mass changes in a sample that can be related to material transitions, loss of incorporated solvent and decomposition of the material. The atmosphere can be chosen to be either inert, such as argon or to contain more reactive gases like hydrogen or oxygen. By noting the percentage of the sample mass lost at each mass loss step and the temperature at which it occurs, it is possible to make a tentative assignment as to the amount of free and bound solvent in the sample or determine decomposition or suitable adsorption temperatures.

In standard TGA, it is not possible to determine which volatile species are being lost at a given temperature without applying a separate analytical technique, such as infrared-spectroscopy, mass spectrometry or gas chromatography to the outgoing gas stream in order to identify any products of decomposition.

2.9. **Inductively Coupled Plasma Mass-Spectroscopy**

Inductively Coupled Plasma (ICP)[21–23] is a powerful technique that is used for the determination of metals present in a sample. ICP-MS allows for quantitative measurement of a large number of elements and quantities of the elements in question. The elements detectable by this technique and the concentrations that can be determined are shown in Figure 17.

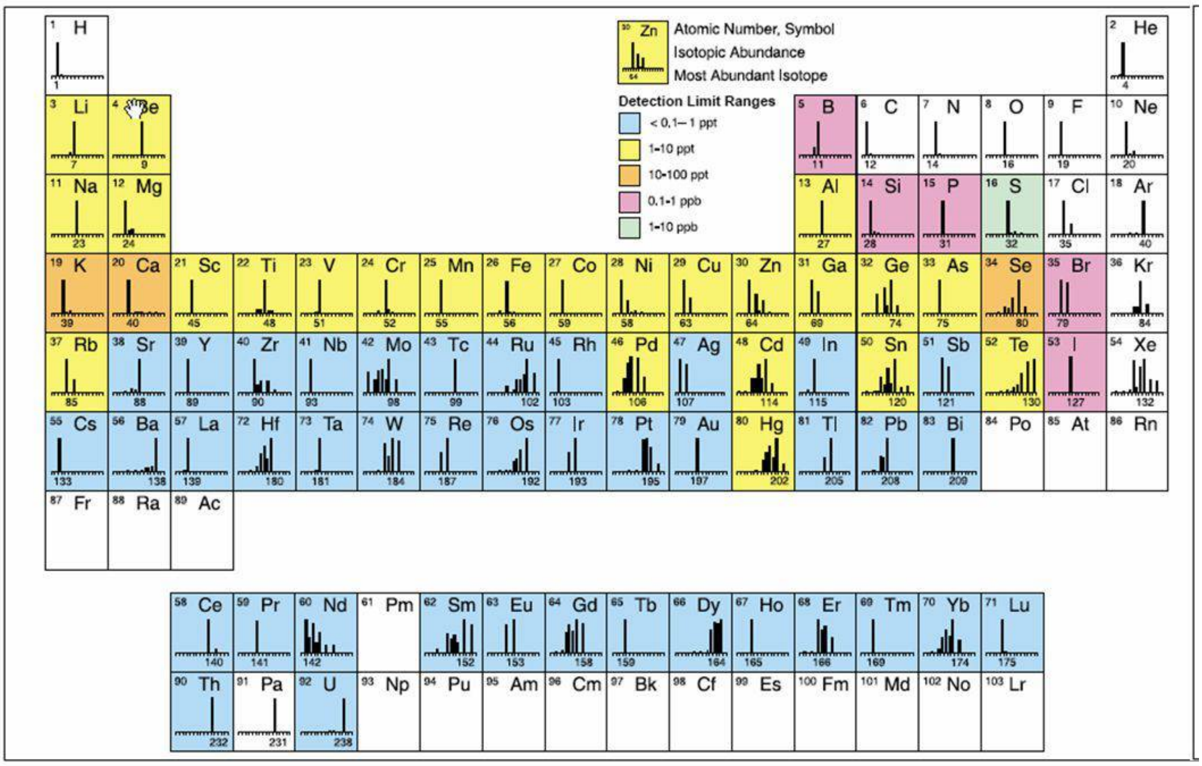

Figure 17: Periodic Table showing elements detectable by ICP-MS. Courtesy of Perkin-Elmer.

It is typically used for determining metal content of samples and the use of a plasma has benefits over traditional flame ionisation by allowing the ionisation to occur in an inert environment, free from oxidation and allowing for more complete ionisation of the sample. Calibration of the device with standard solutions of the element being examined allow for extremely accurate determination of quantities present.

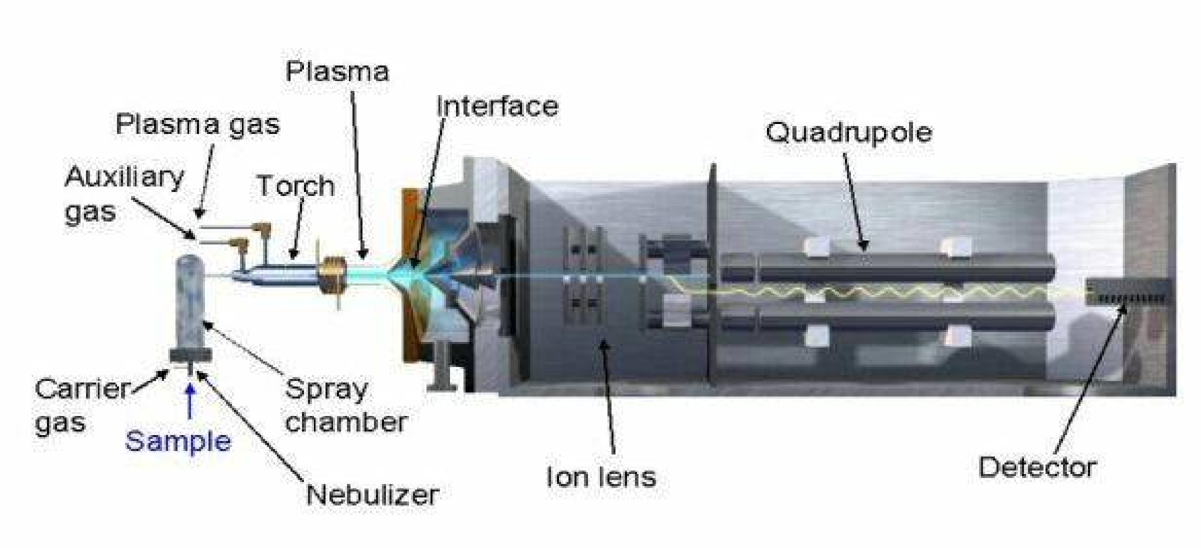

Figure 18: Diagram of an ICP-MS system.[24]

ICP-MS operates under four basic steps, sample introduction, ICP torching, interface and mass-spectroscopy. The sample is dissolved in nitric acid and then is aerosolised into the plasma (introduction), which is formed from argon gas which has been ionised (ICP torch). The sample is then passed into the mass-spectrometer (interface) which allows for identification of the elements and their quantities present (mass-spectroscopy). The ions present in the plasma pass through the quadrupole region of the device via ion lenses. The quadrupole region is charged to prevent the charged ions from diverging from their path. Passing through the quadrupole also has the effect of separating the ions by their mass to charge ratio (m/z). The ions then strike the detector, which generates a signal proportional to the concentration. By comparing these values to solutions of known concentration, it becomes possible to determine concentrations of trace metals in the parts per billion range. Mass spectroscopy is notable in that it allows very rapid detection of a range of ions, with measurements only taking seconds to fully quantity the range present in the sample.

For ICP-MS work done in this project, the samples are weighed before being dissolved due to the mesoporous silica component being insoluble in nitric acid. By using this technique to calculate the present mass of the metal that makes up the MOF and then subtracting it from the original sample weight, it is possible to determine the quantity of MOF present in the sample. The samples are compared to solutions of known concentrations of metal ions to obtain information in the ppb concentration present in each sample.

2.10. Ball Milling

Ball milling[25] is a mechanical process where a sample can have its particle size reduced by repetitive mechanical grinding. Typically, a sample is dispersed in a solvent alongside a grinding media such as zirconia spheres of a uniform size. Once dispersed, the vessel is rotated or shaken continuously to grind the sample particles to a smaller size. The diameter of the grinding media is related to the particle size that can be obtained, with smaller diameter grinding media producing smaller particles. The ground material is then separated from the media by decanting or filtration and the distribution of particle sizes can be measured. Recovering the material from the solvent by rotary evaporation causes aggregation of the particles. As such, recovered material should be ground, sieved and treated with ultrasonic waves to minimise aggregation and maintain the new particle size. In industrial processes, the slurry produced is typically used without recovery of the particles and as such, many of these issues do not come into play on large scale use of ball milling.

2.11. Particle Size Analysis

Particle sizes of samples were determined using laser scattering in a Mastersizer 2000 system courtesy of Professor John Irvine. [26] This allows for determination of particle sizes from as low as 0.01µm to 2000µm. The material to be examined is dispersed in a solvent, water or *iso*propyl alcohol (IPA) by stirring and ultrasonication before being exposed to a laser beam. The angle at which light is backscattered from the particles is inversely proportional to the size of the particle. These angles are measured and compiled computationally to give a distribution of the particle sizes, showing the range of particle sizes present with the intensity at a given size being representative of quantity of particles at that size.

2.12. References

1 W. Clegg, *Crystal Structure Determination*, Oxford University Press, 1998.

2 Rudi Winter, *Univ. Aberd. X-Ray Diffr.*

3 P. A. Webb, C. Orr, R. W. Camp and J. P. Olivier, *Analytical Methods in Fine Particle Technology*, Micromeritics Instrument Corp, Norcross, 1997.

4 D. M. Young and A. D. Crowell, *Physical adsorption of gases*, Butterworths, London, 1962.

5 K. S. Walton and R. Q. Snurr, *J. Am. Chem. Soc.*, 2007, **129**, 8552–8556.

6 S. Brunauer, *The Adsorption Of Gases And Vapors Vol I*, Oxford University Press., 1943.

7 T. Grant Glover, G. W. Peterson, B. J. Schindler, D. Britt and O. Yaghi, *Chem. Eng. Sci.*, 2011, **66**, 163–170.

8 A. K. Brisdon, *Inorganic spectroscopic methods*, Oxford University Press, Oxford, 1998.

9 P. J. Goodhew and F. J. Humphreys, *Electron microscopy and analysis*, Taylor & Francis, London, 2nd ed., 1988.

10 Image courtesty of University of Exeter, *Hollow Silica Nanoparticles Seen SEM*.

11 P. J. Hore, *Nuclear magnetic resonance*, Oxford University Press, Oxford ; New York, 1995.

12 J. A. Iggo, *NMR spectroscopy in inorganic chemistry*, Oxford University Press, Oxford ; New York, 1999.

13 J. W. Hennel and J. Klinowski, in *New Techniques in Solid-State NMR*, ed. J. Klinowski, Springer Berlin Heidelberg, 2005, pp. 1–14.

14 A. E. McDermott and T. Polenova, *Solid State NMR Studies of Biopolymers*, John Wiley & Sons, 2010.

15 E. R. Andrew, A. Bradbury and R. G. Eades, *Nature*, 1958, **182**, 1659–1659.

16 Y. Ishii, N. P. Wickramasinghe and S. Chimon, *J. Am. Chem. Soc.*, 2003, **125**, 3438–3439.

17 N. P. Wickramasinghe and Y. Ishii, *J. Magn. Reson.*, 2006, **181**, 233–243.

18 D. M. Dawson, Thesis, University of St Andrews, 2014.

19 M. J. Duer, *Introduction to solid-state NMR spectroscopy*, Blackwell, Oxford ; Malden, MA, 2004.

20 A. W. Coats and J. P. Redfern, *Analyst*, 1963, **88**, 906–924.

21 S. Duckett and B. C. Gilbert, *Foundations of spectroscopy*, Oxford University Press, Oxford, 2000.

22 Hou, Xiandeng and Jones, Bradley T., *Encyclopedia of Analytical Chemistry*, R.A. Meyers.

23 J. A. C. Broekaert, in *Handbook of Spectroscopy*, eds. G. Gauglitz and D. S. Moore, Wiley-VCH Verlag GmbH & Co. KGaA, 2014, pp. 583–646.

24 Image Courtesy of University of Washington in St. Louis, *ICP-MS Facil. Oper.*

25 M. Sopicka-Lizer and ScienceDirect(Online service), Eds., *High-energy ball milling: mechanochemical processing of nanopowders*, CRC Press ; Woodhead Pub, Boca Raton, Fla. : Oxford, 2010.

26 Jillavenkatesa, Ajit; Dapkunas, Stanley J.; Lum, Lin-Sien H., *NIST Spec. Publ. 960-1*, 2001.

Chapter 3 Experimental Information

3.1. Synthesis of MOF-74/CPO-27

Synthesis of these MOFs based on references. [1–3]

3.1.1. Synthesis of CPO-27-Ni

Nickel acetate tetrahydrate (0.568 g, 2.283 mmol) and 2,5-dihydroxyterephthalic acid (0.224 g, 1.131 mmol) were dissolved in a mixture of water (50 mL) and THF (50 mL) with stirring. The mixture was transferred to a Teflon autoclave liner and sealed in an autoclave. The autoclave was heated to 383K for 72 hours before being cooled and the resulting material recovered by filtration and washed with methanol. Typical yield 0.4710 g (1.9 mmol, 84% yield).

3.1.2. Synthesis of CPO-27-Mg

Magnesium nitrate hexahydrate (0.500 g, 1.95 mmol) and 2,5-dihydroxyterephthalic acid (0.200 g, 1.01 mmol) were dissolved in a mixture of THF (14 mL), water (6 mL) and 1M sodium hydroxide solution (4 mL, 4 mmol) in a Teflon autoclave liner and sealed in an autoclave. The autoclave was heated to 383K for 72 hours before being cooled and the material recovered by filtration and washed with methanol. Typical yield 0.299 g (0.707 mmol, 70% yield)

3.1.2.1. Synthesis of a sodium salt of dihydroxyterephthalic acid for CPO-27-Mg preparation

Sodium hydroxide pellets (8.20 g, 0.205 mol) were dissolved in water (100 mL), and H_4dhtp (10.0 g, 0.0505 mol) was dissolved in ethanol (100 mL). The two solutions were combined and stirred for 1 hour at ambient temperature. The solvent was then removed using rotary evaporation, and the solid dispersed and triturated in ethanol (200 mL) and the mixture heated to reflux for 16 hours. A pale yellow solid recovered by filtration. Typical recovery ~12.5 g.

3.1.2.2. Na_xH_{4-x}dhtp Synthesis of CPO-27-Mg

Na_xH_{4-x}.dhtp (2.40 g 9.83 mmol based on Na_2H_2dhtp) and magnesium nitrate hexahydrate (7.69 g 30.0 mmol) were dissolved in water (66 mL) and ethanol (33 mL) and heated to reflux for 16 hours. The solid was recovered by filtration and washed with ethanol. Recovered solid 3.78 g (91% yield, 8.95 mmol).

An alternate method was used in which the $Mg(NO_3)_2$/Na_xH_{4-x}dhtp solution was subjected to microwave heating at 383K for 2 hours. No solid was recovered.

3.2. Synthesis of Mesoporous Silica

Synthesis was adapted from work by Seo *et al*.[4] In a polyethylene bottle, Pluronic 123 (P123, 8.1 g, 1395 mmol) was dispersed in a solution of glacial acetic acid (4 g, 66.6 mmol) in water (166 mL) and the resulting mixture stirred for one hour at 333 K. In a separate bottle, tetraethylorthosilicate (TEOS, 11.458 g, 55 mmol) and 4-(triethoxysilyl) butyronitrile (TESBN, 1.15 g, 5 mmol) were dispersed in water (166 mL) and stirred for 1 hour. The two mixtures were combined and heated to 373 K for 16 hours. The resultant solid was collected by filtration and washed with water and ethanol before being dried at room temperature. The resulting solid was designated MS-TESBN, (Mesoporous Silica-triethyxysilylbutyronitrile.) Typical recovered solid 4.3 g.

3.2.1. Template removal from MS-TESBN

MS-TESBN (2 g) was dispersed in a solution of sulfuric acid (48%, 200 mL) and stirred for 16 hours. The solid was recovered by filtration and washed with water and dried at room temperature. This solid was designated MS-COOH (Mesoporous Silica- Carboxylic Acid). Recovered solid: 0.7298 g.

3.2.2. Post-Synthetic Methylation of Mesoporous Silica

MS-COOH (1 g) was dispersed in toluene (120 mL) with stirring. Methytriethoxysilane (0.89 g, 5 mmol) was added dropwise to the solution. The solution was then refluxed overnight before being dried by rotary evaporation under reduced pressure. Material was designated MS-COOH-M (Mesoporous Silica-Carboxylic Acid-Methyl). Recovered solid: 0.87 g.

3.2.3. Impregnation of Mesoporous Silica

MS-COOH-M (1g was ground into a fine powder with a pestle and mortar before being put in an evaporating basin. Nickel nitrate or magnesium acetate (0.2 M, 100 mL) in aqueous methanol (4:1 MeOH: H2O) is poured into the evaporating basin and stirred before being placed in an oven to evaporate slowly at 333 K. This evaporation process was repeated twice more, giving a final loading of 2.46 mmol/g of loaded solid. Typical recovered solid 1.46 g.

3.2.4. Synthesis of CPO-27 inside the mesoporous silica

Impregnated mesoporous silica (0.500 g, 2.46 mmol of Mg^{2+} per gram, 1.23 mmol Mg^{2+}) was suspended in water (15 mL) and THF (15 mL) with H_4dhtp (0.14 g 0.707 mmol) and briefly stirred. The mixture was sealed in an autoclave and heated to 383 K for 3 days. The resulting solid was recovered by filtration and washed with methanol before drying. Typical recovered solid 0.285 g.

3.3. Synthesis of STAM-1

STAM-1 was synthesised using the method published by Mohideen *et al*.[5] A typical synthesis involved dissolving $Cu(NO_3)_2.3H_2O$ (9.62 g, 40 mmol) and trimesic acid (8.42 g, 40 mmol) in a mixture of MeOH and water (400 mL, 50:50) and stirred at ambient temperature for 15 minutes in a Teflon 600 mL autoclave liner. The liner was then sealed in the autoclave and heated at 383 K for 7 days. The autoclave was then cooled to ambient temperature and the product recovered by filtration, where it was washed with methanol and acetone. Typical yield, 9.5g (28 mmol, 70%).

3.4. Synthesis of Cu(EtOip)

Synthesis[6] of Cu(EtOip) was undertaken by combining 5-ethoxy isophthalic acid(0.440 g, 2 mmol) and copper acetate monohydrate (0.4g, 2 mmol) in a Teflon lined autoclave in water (30 mL) and heated at 383 K for three days. The autoclave was then cooled and the solid recovered by filtration before being washed with ethanol and dried at ambient temperature. Typical yield (0.603 g, 1.9 mmol, 95% yield).

3.5. Armoured MOF Process - General Procedure

Procedure adapted from work on other MOFs.[7] MOF material (1 g) was dispersed in a methanolic solution (63 mL) of polyvinylpyrrolidone (PVP, 0.6 g) and heated with stirring to 328 K in a polypropylene bottle for 1 hour. The solution was then cooled to room temperature. A separate solution of water (198 mL), methanol (63 mL) and sodium acetate trihydrate (3.0 g, 22 mmol) was prepared and added to the cooled MOF suspension.

When the solutions are combined, the pH was measured and adjusted to 8.5 by dropwise addition of aqueous sodium hydroxide solution (1 M). To the resulting solution, cetyltrimethylammonium chloride solution (25%wt in water, 3.3 mL, 0.88 mmol CTACl) was added and stirred for 30 minutes. Then TEOS (2.4 mL, 10.75 mmol) was added dropwise to the solution while stirring continuously. The bottle was then sealed and the mixture left to stir for 3.5 hours. The resulting solid was recovered by filtration and washed with acetone. To remove the template from the pores of the mesoporous silica, the material was placed in a Schlenk flash and placed under reduced pressure before heating to 523 K using a Buchi furnace for 4-16 hours.

3.6. Ball Milling Procedure

MOF material (2 g) was dispersed in *iso*propylalcohol (30 mL) in a 125 mL polypropylene bottle. Grinding media was added (280 g, 0.3 mm YTZ grinding media) and the bottle sealed and checked for leaks. The bottle was then rotated on a “rolling-road” apparatus at approximately 110 rpm for 16 hours. After 16 hours, the bottle was opened and the material recovered by removing the solution via pipette, and the grinding media washed in a further 30 mL of solvent. The two batches of solvent are combined and rotary evaporated to dryness. The solid was then ground in a pestle and mortar before being sieved through 120 and 250 mesh sieves. Material that does not pass through the sieves was reground and sieved again before being dehydrated in a Buchi furnace at 423 K under dynamic vacuum for 16 hours and sealed in an argon atmosphere for later use.

3.7. Desolvation Procedure

Samples were weighed individually into glass ampoules and placed inside a Schlenk flask attached to a vacuum manifold and placed in a Buchi furnace. The flask was sealed with a Subaseal and evacuated by a rotary vacuum pump. Once under vacuum, the temperature of the flask was increased to 423K for CPO-27-Ni and STAM-1, or to 523K for CPO-27-Mg. Once temperature was reached and the solvent from the pores and surface of the material was removed, the pressure was further decreased by means of a diffusion pump to remove any solvent bound to metal centres. The flask was kept under vacuum and at elevated temperature until suitably low pressure was shown, typically in the order of 10^{-3} mTorr over the course of 16 hours. Once this pressure was reached, the flask was flushed with argon and the ampoules were flame sealed to preserve the sample.

3.8. Nitrogen Adsorption, CO_2 Adsorption, BET Surface Area

Samples were ground in pestle and mortar and transferred into a pre-weighed sample tube with frit. The tube and contents were weighed and sealed with the frit. To remove solvent, the sample was placed under reduced pressure, at an evacuation rate not higher than 7 mmHg/s and heated in two stages. The samples were heated in vacuo in two stages, rising to 383K at 5 K/min and remaining at this temperature for one hour. After that the temperature was raised at 2 K/min to appropriate temperature for the MOF being examined. Typically this temperature is 423 K, with the exception of CPO-27-Mg, which was heated to 523 K. For the nitrogen adsorption, the sample was dosed incrementally with increasing volumes of nitrogen until atmospheric pressure was reached. The pressure in the tube was then reduced incrementally to less than 0.00001 atmospheres.

3.9. Ammonia Micro-breakthrough

Ammonia micro-breakthrough was conducted under test flow of 30 ml/min, 30mg sample size, packed in a 4mm i.d. glass tube between plugs of cotton wool. Test concentration was 500ppm, generated by adding a known flow of ammonia, selected by mass flow controller into a known flow of dry air. The ammonia output is measured via photoionisation detector, which ionises molecules by use of high-energy photons. The ionised molecules interact with the detector, creating an electrical current which is measured via an ammeter. The equivalent concentration for that current is then displayed by the detector.

3.10. VT PXRD

Samples examined under variable temperature PXRD were placed in an alumina disc, mounted on the detector apparatus and held in place with an aluminosilicate ring. Data was then collected on the sample over 2θ of 2.5-25 with a molybdenum source. The initial data was collected under ambient conditions before the chamber was evacuated and the data was collected at 25°C intervals rising to 250°C at a rate of 10°C/min with a 15 minute equilibration period allowed once temperature was reached. The sample was then cooled to room temperature in 25°C intervals at a rate of 10°C/min with a 15 minute equilibration time, and data collected at each interval. Once the temperature returned to ambient conditions, the sample was recovered. In the case of STAM-1 and isophthalic-acid derived MOFs, the sample was then re-examined under ambient conditions on a 2θ range of 5-50° on a copper radiation source.

3.11. Water Adsorption

Water adsorption was undertaken on a DVS Advantage 2 gravimetric system. The sample (~30 mg) was placed on a microbalance and the chamber was exposed to increasing levels of humidity. Samples were considered to have reached equilibrium uptake with the level of humidity when it displayed less than a 0.002%/min.

3.12. TGA Procedure

The sample was placed in an aluminosilicate or platinum crucible inside the TGA apparatus and the starting weight logged. The sample was put under gas flow (air in the case of all samples in this project) and the temperature was increased at a fixed rate of 10 K/min to 9. Once the sample was cooled, it was then disposed of.

3.13. ICP Procedure

Samples for ICP-MS analysis were weighed using a sensitive microbalance and then added to concentrated nitric acid with stirring. The liquid was transferred to the ICP-MS and the metal content of the samples analysed. The remaining silica was recovered, washed with water and dried and weighed again. The amounts of MOF and solvent water present in the hybrid materials were then calculated using the mass of recovered silica and the amount of metal determined from ICP-MS experiments.

3.14. References

1 P. D. C. Dietzel, P. A. Georgiev, J. Eckert, R. Blom, T. Strassle and T. Unruh, *Chem. Commun.*, 2010, **46**.

2 P. D. C. Dietzel, B. Panella, M. Hirscher, R. Blom and H. Fjellvåg, *Chem. Commun.*, 2006, 959–961.

3 P. D. C. Dietzel, V. Besikiotis and R. Blom, *J. Mater. Chem.*, 2009, **19**, 7362–7370.

4 Y.-K. Seo, J. W. Yoon, U.-H. Lee, Y. K. Hwang, C.-H. Jun and J.-S. Chang, *Microporous and Mesoporous Materials*, 2012, **155**, 75–81.

5 M. I. H. Mohideen, B. Xiao, P. S. Wheatley, A. C. McKinlay, Y. Li, A. M. Z. Slawin, D. W. Aldous, N. F. Cessford, T. Düren, X. Zhao, R. Gill, K. M. Thomas, J. M. Griffin, S. E. Ashbrook and R. E. Morris, *Nat Chem*, 2011, **3**, 304–310.

6 L.J. McCormick, S.A. Morris, M.J. McPherson, D.B. Cordes, A.M.Z. Slawin, S.J. Teat and R.E. Morris, *Manuscript in Preparation.*

7 Z. Li and H. C. Zeng, *J. Am. Chem. Soc.*, 2014.

Chapter 4 Ammonia Uptake and Stability of STAM-1 in Humid Conditions.

4.1. Background

In 2011, Mohideen *et al* published their findings with regards to the production of a new MOF, STAM-1, which was synthesised from trimesic acid and copper salts, which would typically be used to produce HKUST-1.[1] When the solvent system of ethanol and water was replaced with a methanol and water system, an esterification reaction took place at the carboxylic acid groups. When the mono-esterified ligand came into contact with the copper ions in solution, it formed a two-dimensional framework which has a dual-pore system (Figure 19), comprising pores where the methyl ester protrudes into one pore, creating a hydrophobic channel and a separate channel without methyl groups facing into it, creating a hydrophilic channel.

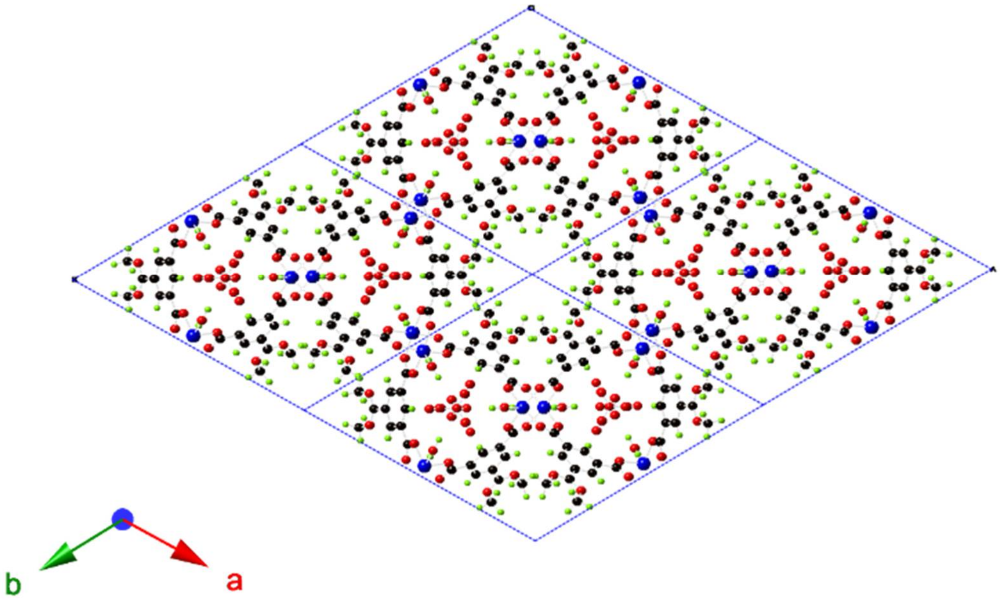

Figure 19: STAM-1 showing hydrophobic and hydrophilic pores. Cu = Blue, O = Red, C= Black, H = Green.

The hydrophobic channels provide a natural starting point for adsorption of toxic gases from a humid atmosphere, as they exclude water without any further modification. The hydrophilic channels can also be evacuated of the solvent molecules present and the water molecules bound to the copper acetate lanterns present in the structure can be removed to provide open-metal sites that are suitable for the adsorption of toxic gases. Compared to the related and well-studied HKUST-1 structure, comparatively little work has been done on STAM-1, in part due to the relative difficulty of synthesis, as the product is contaminated with small quantities of HKUST-1, which, if not removed, will affect the measured properties of the material. STAM-1, however, has shown surprising resilience to conditions that cause HKUST-1 to experience pore collapse and lose structural integrity, such as increasing temperature and relative humidity. The investigation of the long term stability of STAM-1 when exposed to humid conditions and its ability to continue to remove toxic gases, particularly ammonia, from the environment will shed light on the ammonia adsorption mechanism and the overall viability of the MOF as a potential respirator cartridge material.

4.2. STAM-1 Synthesis and Characterisation

STAM-1 is produced for laboratory analysis by solvothermal synthesis in a Teflon-lined steel autoclave. While HKUST-1 is made from the same two components, a copper salt and trimesic acid and has been produced via a number of different techniques (including several “low-solvent” or “no-solvent” methods), STAM-1 relies on the presence of methanol to allow for a mono-esterification reaction to occur at one of the carboxylic acid moieties on the ligand.

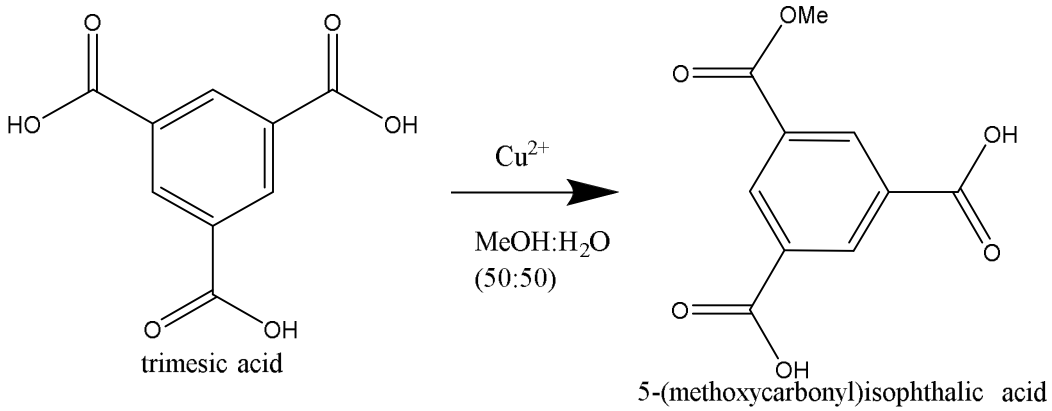

Figure 20: Mono-esterification of trimesic acid in the presence of Cu(II) in a methanol: water solvent mixture leads to the production of mono-methyl ester.

There is no reported method in the literature to directly produce the mono-ester in preparative yield, with the reaction proceeding directly to the tri-ester, which is then transformed to the mono-ester by use of hydrochloric acid.[1,2] The mono-ester can also be recovered from several MOFs including STAM-1 by discorporating the structure and the recovered ligand can then be used in other reactions. This method was used to explore further STAM-1-like structures, leading to STAM-2 and several others in the STAM MOFs.[3]

The typical yields of STAM-1 produced by solvothermal reaction were high, with 85%+ being typical (based on quantity of ligand used). Small quantities of HKUST-1 contaminate the reaction due to the relative ease with which it begins to form when trimesic acid is in contact with a Cu(II) ion, which has been shown to occur even when extremely small quantities of solvent are present or with ball milling, where solvent is not required during the reaction and is only used to remove unreacted reagents after recovery of the solid. The powder XRD pattern below shows the contamination alongside the separate predicted patterns for STAM-1 and HKUST-1.

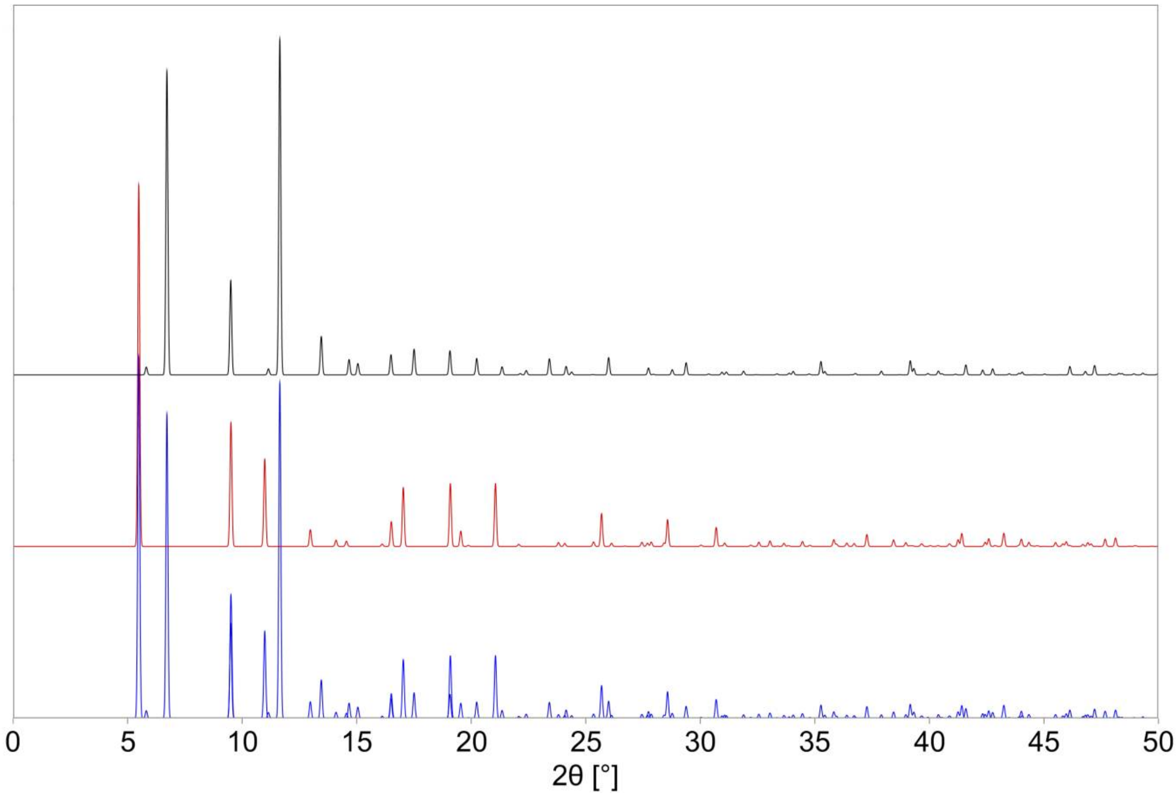

Figure 21: PXRD showing STAM-1 as synthesised with HKUST-1 contamination (blue), STAM-1 simulated pattern (red) and HKUST-1 simulated pattern (black).

In cases where purification is necessary, stirring the solid in water for a short period results in the collapse and disintegration of HKUST-1, after which the STAM-1 can be filtered off and washed with organic solvent to remove trimesic acid. As described below, STAM-1 was subjected to a process which would deposit a shell of mesoporous silica around the MOF with potential to improve the mechanical properties of the MOF which involved stirring in basic aqueous conditions for an extended period and heating to 250°C, both of which have severe effects on the structure of HKUST-1, leaving only STAM-1.

4.3. Characterisation of STAM-1

STAM-1 was produced using existing syntheses and analysed by powder XRD to determine if the correct phase had been obtained. As with the previous published results by Mohideen[1,3], STAM-1 was obtained with HKUST-1 contamination shown in Figure 22 below.

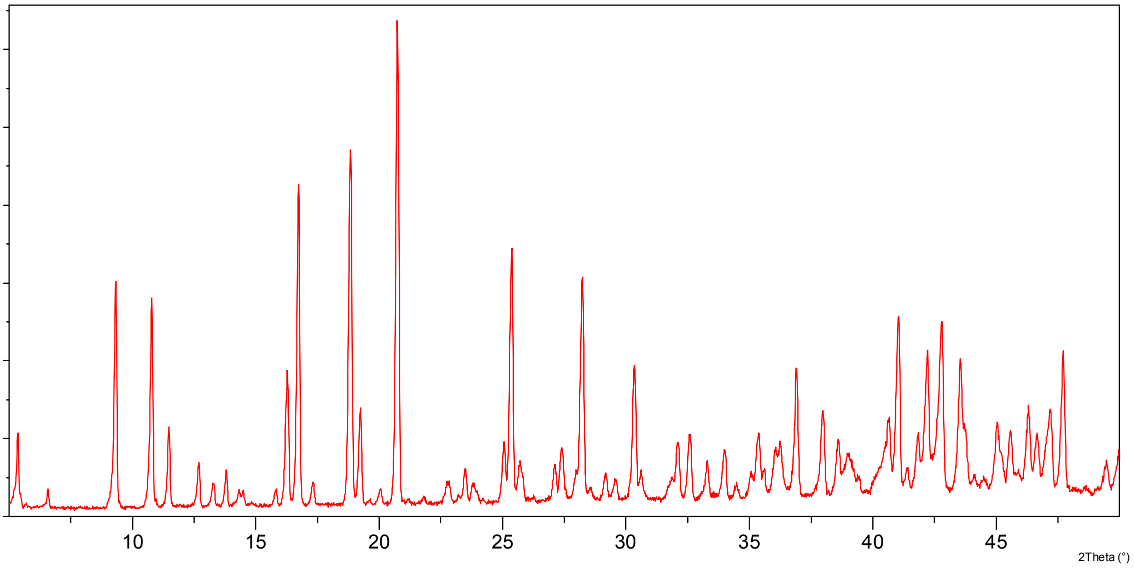

Figure 22: PXRD of STAM-1 contaminated with HKUST-1.

The amount of HKUST-1 present in the sample was considered negligible for the purposes of analysis with the expectation that the processing steps that STAM-1 was subjected to would result in the discorporation of the HKUST-1 and the resultant metal and ligand being removed into the solution phase.

As this project largely focussed on the ability of the MOF to separate gases from the nitrogen/oxygen mix of the air, surface area measurements were taken on each produced batch of STAM-1 to ensure viability. Surface area measurements were conducted on a Micromeritics ASAP2020. A powdered sample was heated under reduced pressure to remove solvent from the pores for sixteen hours before being tested for surface area and porosity using both nitrogen at cryogenic temperatures and carbon dioxide at 25°C. Traditional BET calculations using data points obtained in the region of 0.05-0.3 P / P_0 give a surface area of 130-212 $m^2\ g^{-1}$, which is consistent with the values reported by Mohideen.[3]

As a material being explored for its toxic gas removal properties, STAM-1 was tested using a micro-breakthrough method to determine its performance against a commonly encountered small molecule toxic gas, ammonia.[4–6] In order to gauge the performance of STAM-1, HKUST-1 was selected as a general comparison material due to its chemical similarities to STAM-1. HKUST-1 is perhaps one of the most well studied MOFs in recent years, due to its ease of manufacture and production on industrial scale allows for commercial purchase of consistent, high-quality material.

4.4. Optimisation of Ammonia Breakthrough Testing

The micro-breakthrough experiments initially operated on a fixed weight of sample being packed into a column with glass wool and placed under a flow equivalent to 500 ppm ammonia in dry or humid air (80% relative humidity) at a rate of 30mL/min. This produces a breakthrough curve which plots time on the x-axis and the concentration of ammonia along the y-axis. The point on the graph where the rise begins indicates the breakthrough time and the area above the curve of the graph represents the total capacity of the material.

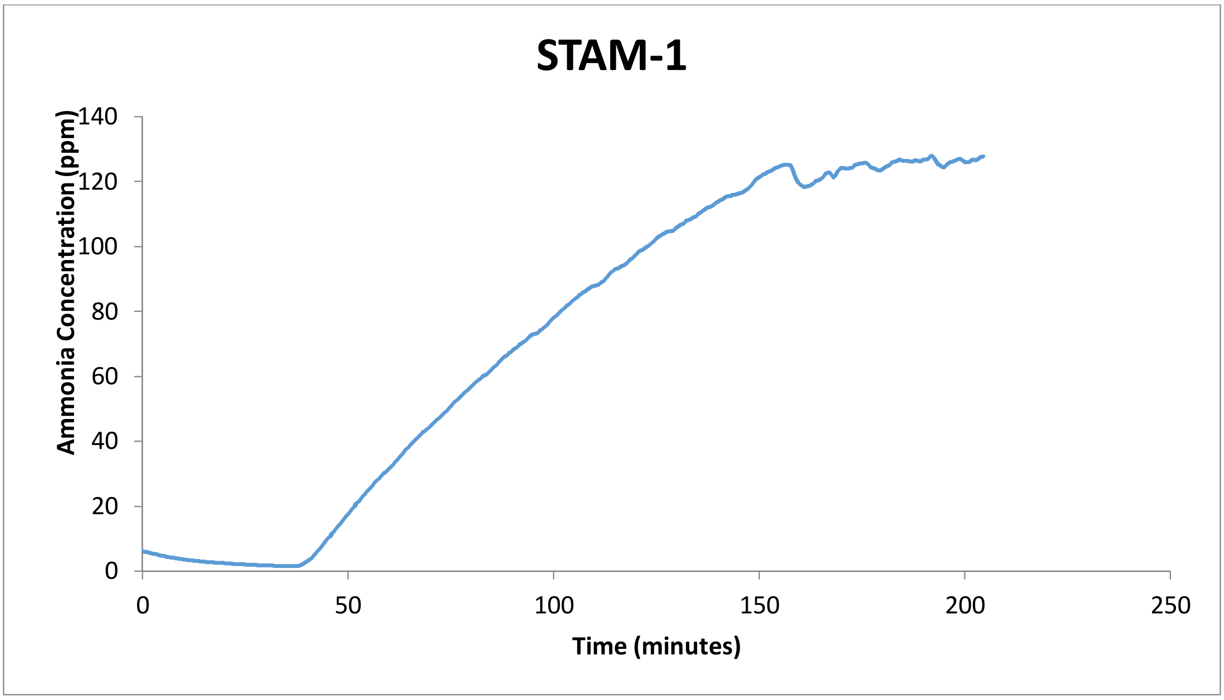

Figure 23: Breakthrough time of STAM-1 in dry conditions. This has not been adjusted and reflects the raw output of the breakthrough apparatus. The above-zero start of the isotherm is attributed to improper packing of the material. This was rectified in later tests.

While working with the material for breakthrough purposes, it was noted that results for the material were inconsistent from sample to sample. Unlike previous samples and currently operating materials, the greatly increased breakthrough time of the material necessitated the samples to run unattended for extended periods. After inconsistent results, continuous visual inspection of the samples revealed a problem. During the preparation of the samples, consistent packing was found to be problematic which had not been observed with other MOFs tested in this manner. This resulted in the gas flow moving through incompletely packed samples via the “path of least resistance” creating an uneven flow through the materials, allowing most of the ammonia to bypass the sample altogether. This was attributed to the varied particle size of STAM-1, which ranges from sub-micrometre to hundreds of micrometres without any additional processing of the material.

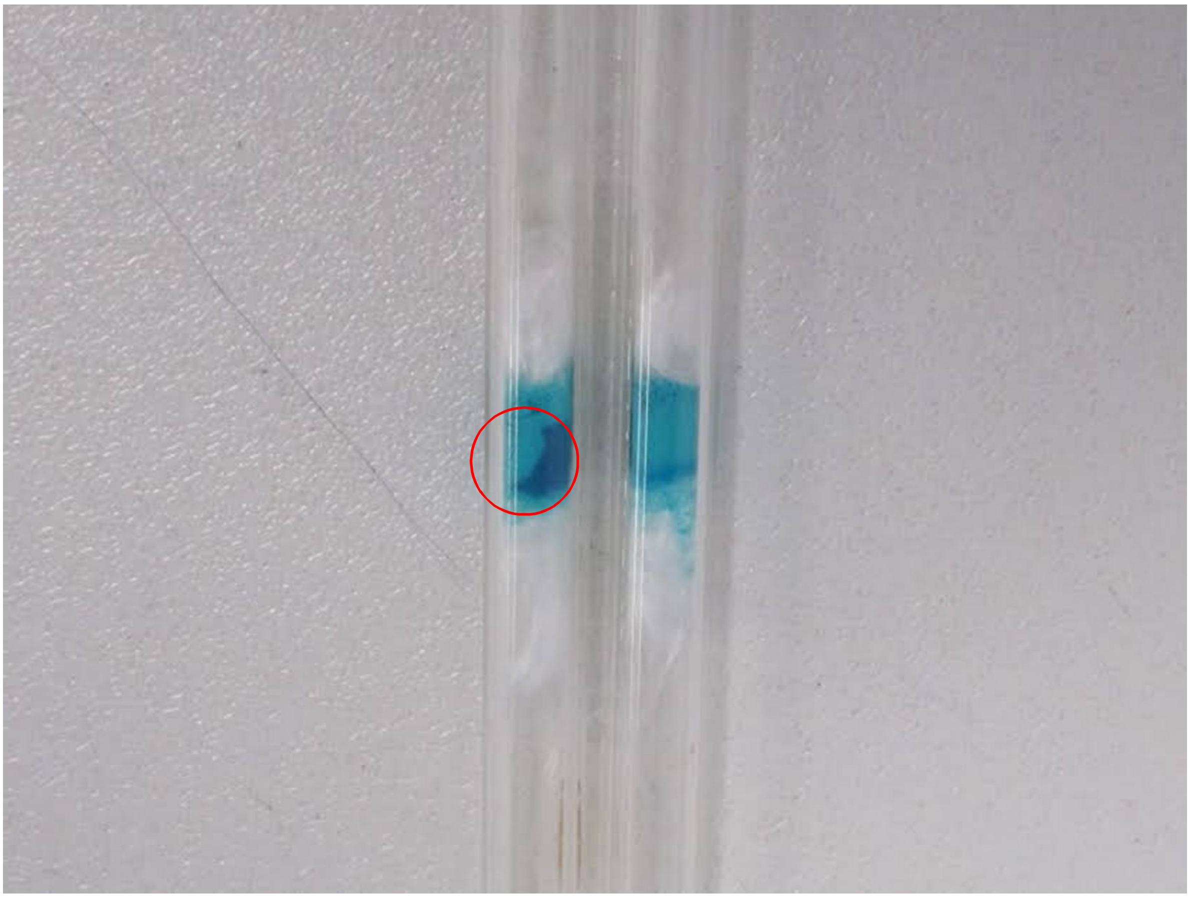

Figure 24: Packed columns of STAM-1 material after ammonia breakthrough. Note the uneven travel path of the challenge gas through the material on the left (circled), versus the roughly even transfer through the material on the right.

As a large proportion of the material was sometimes being bypassed by the challenge gas, the ammonia breakthrough times between samples even from the same batch of material could provide vastly differing results. The poor packing was investigated with different samples and with ball-milling of samples, which still continued to produce inconsistent results. Finally, the problem was determined to be the result of the glass wool used to pack the samples. This was unexpected as glass wool is inert to the uptake of ammonia and should not have affected the reported uptake and subsequent breakthrough times. The glass wool did not provide a suitable surface for the test sample to pack onto, resulting in an artificially lowered breakthrough time for samples of STAM-1 that were tested with it. The replacement of the glass wool with cotton wool was found to produce consistent results across multiple tests of the same material with only minor corrections applied to the values obtained to account for the amount adsorbed by the cotton wool.

Alongside the adjustments made for consistency, samples were then corrected for the weight in order to give a weighted value. As analysis continued the system was examined, resulting in corrections to the gas flow rate to take into account the “dead time” of the apparatus, the time taken for the 500 ppm ammonia mixture to flow through the system. Applying all of the corrections obtained gives us the results shown in Figure 25. An example of the calculation applied to data from the apparatus can be found in the Appendix.

4.5. Ammonia Breakthrough of STAM-1

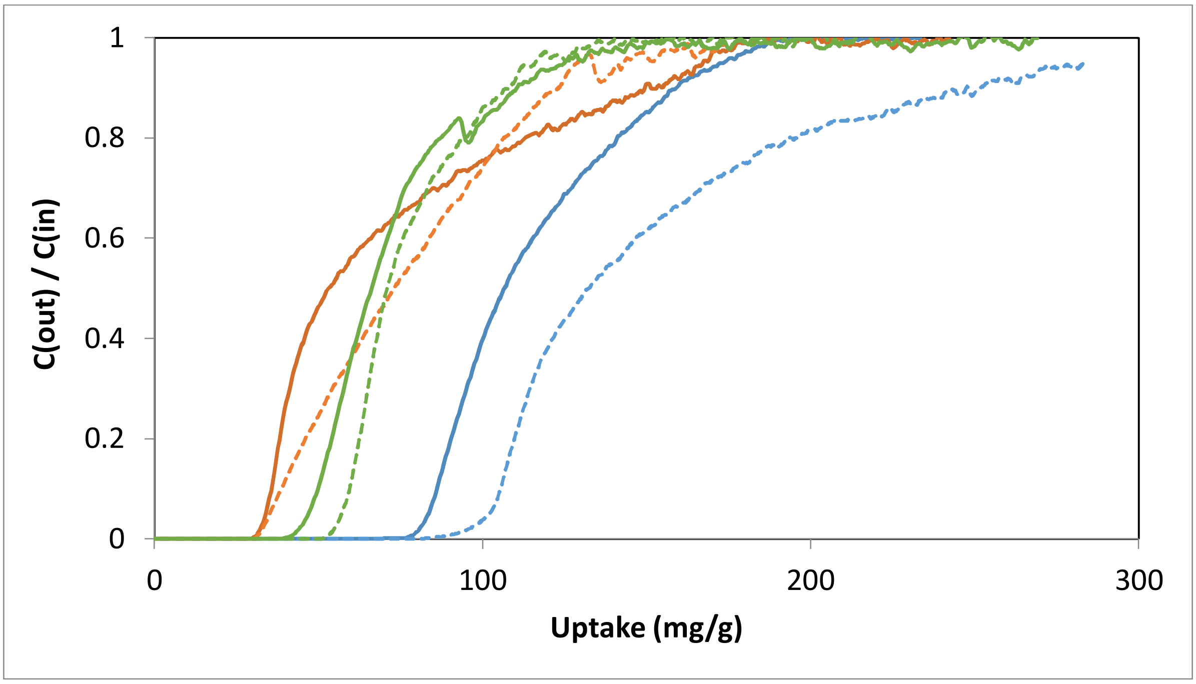

Figure 25: Ammonia breakthrough times of various MOF samples. Blue lines indicate HKUST-1, green and orange lines indicate different batches of STAM-1. Dotted lines indicate repeat runs of a new sample from the same batch of material.

Initial tests on STAM-1 using a 30 mg sample under 30 mL/min flow rate produced breakthrough times of around 80 minutes before calibration of the system to account for the above factors. As can be seen from Figure 25, HKUST-1 shows a larger uptake which corresponds to a larger breakthrough time. Research by Peterson *et al* shows that HKUST-1 breaks down during the adsorption of ammonia, forming suspected copper diamine and ammonium salts of the BTC ligand, causing complete loss of the MOF structure.[7] The relative instability of HKUST-1 was further investigated and compared to that of STAM-1 by water adsorption and ageing studies. This work was carried out at Edgewood Chemical and Biological Centre in Maryland, USA.

In order to produce an analogue to material that had been improperly stored or behaved like an unsealed cartridge that had been attached for a respirator for an extended period, samples of the

MOF were placed in a heated chamber at 45°C with a relative humidity of 90% for 72 hours. This is approximately equivalent to a canister being aged for several weeks at 25°C.

The resulting samples were then tested for ammonia breakthrough capability against unaged samples from the same synthesis. The results of this experiment are shown in Figure 26 and Table 2.

Table 2: Ammonia loading of samples of HKUST-1 and STAM-1 in various conditions.

Sorbent	Conditions	Loading Capacity (mol/kg)
HKUST-1	As-Synthesised	9.4
	Aged	1.0
	Humid	9.5
STAM-1	As-Synthesised	3.3
	Aged	3.1
	Humid	5.9

The as-synthesised samples were exposed to a stream of dry ammonia (2000 ppm concentration), the humid samples were exposed to a stream of humid ammonia (2000 ppm ammonia in a relative humidity of 80%) and the aged samples were exposed to a stream of dry ammonia after the ageing process detailed above.

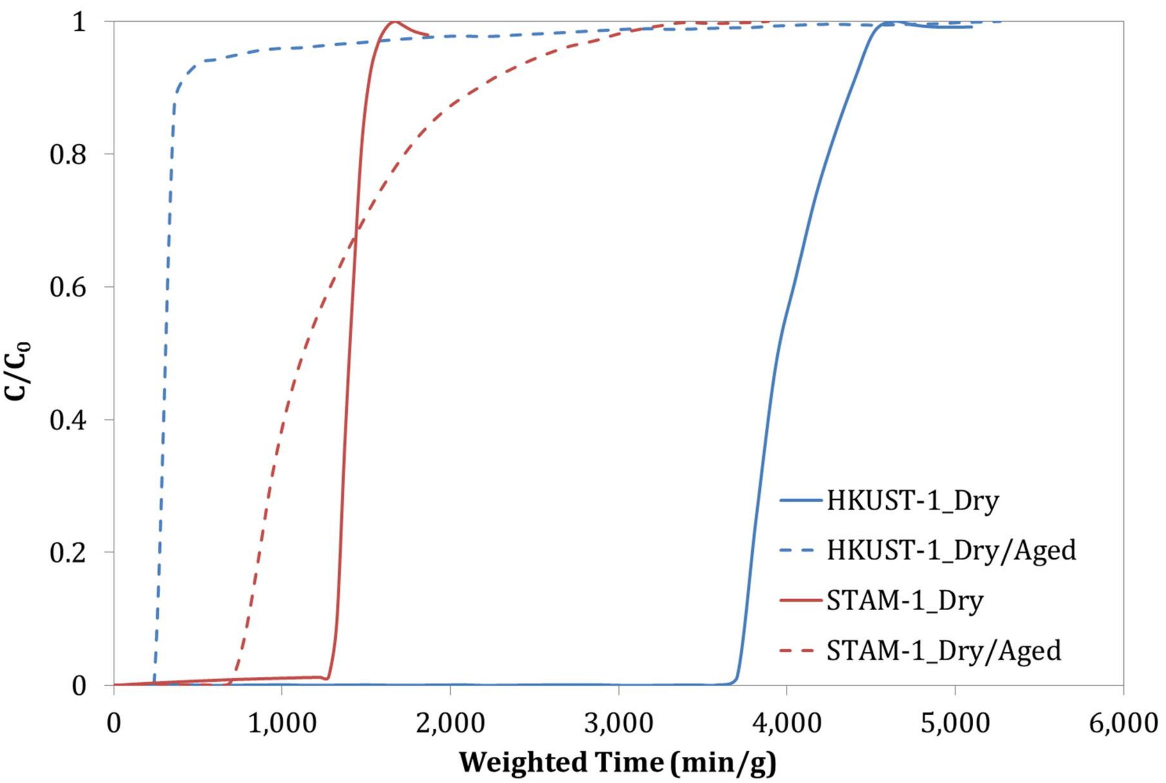

Figure 26: Weight corrected Ammonia Micro-breakthrough on dry and aged samples of HKUST-1(blue) and STAM-1(red). The weighted time (min/g) refers to the number of minutes before the breakthrough of gas occurs for a gram of material. This value is adjusted for the weight of each sample to allow for comparison across samples.

The weighted uptake for as-prepared HKUST-1 is shown to be approximately 3 times greater than that of STAM-1, but there is a 90% loss of capacity after ageing. This has been confirmed by powder diffraction and IR of the MOF before and after the ageing process which shows a complete change in the phase of the material and is consistent with previously reported ammonia adsorption studies of HKUST-1.[6,7]

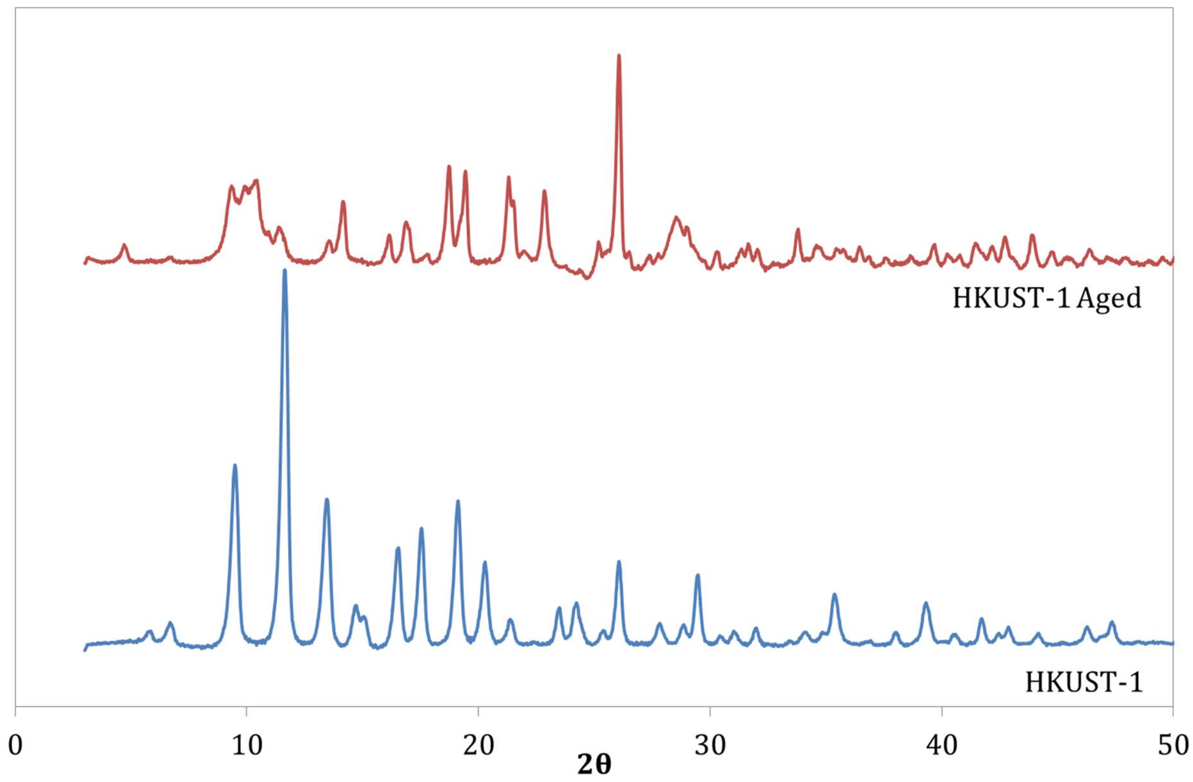

Figure 27: Powder Diffraction of HKUST-1 before and after ageing in elevated temperatures and high humidity.

The same analysis was conducted on STAM-1 (Figure 28), which has largely retained the original powder pattern, though some loss of crystallinity is shown by the broadening of the peaks. This shows STAM-1 has far greater resilience to humid conditions than HKUST-1 and may be a more suitable MOF candidate for a filter material when storage of the filters for extended periods is likely.

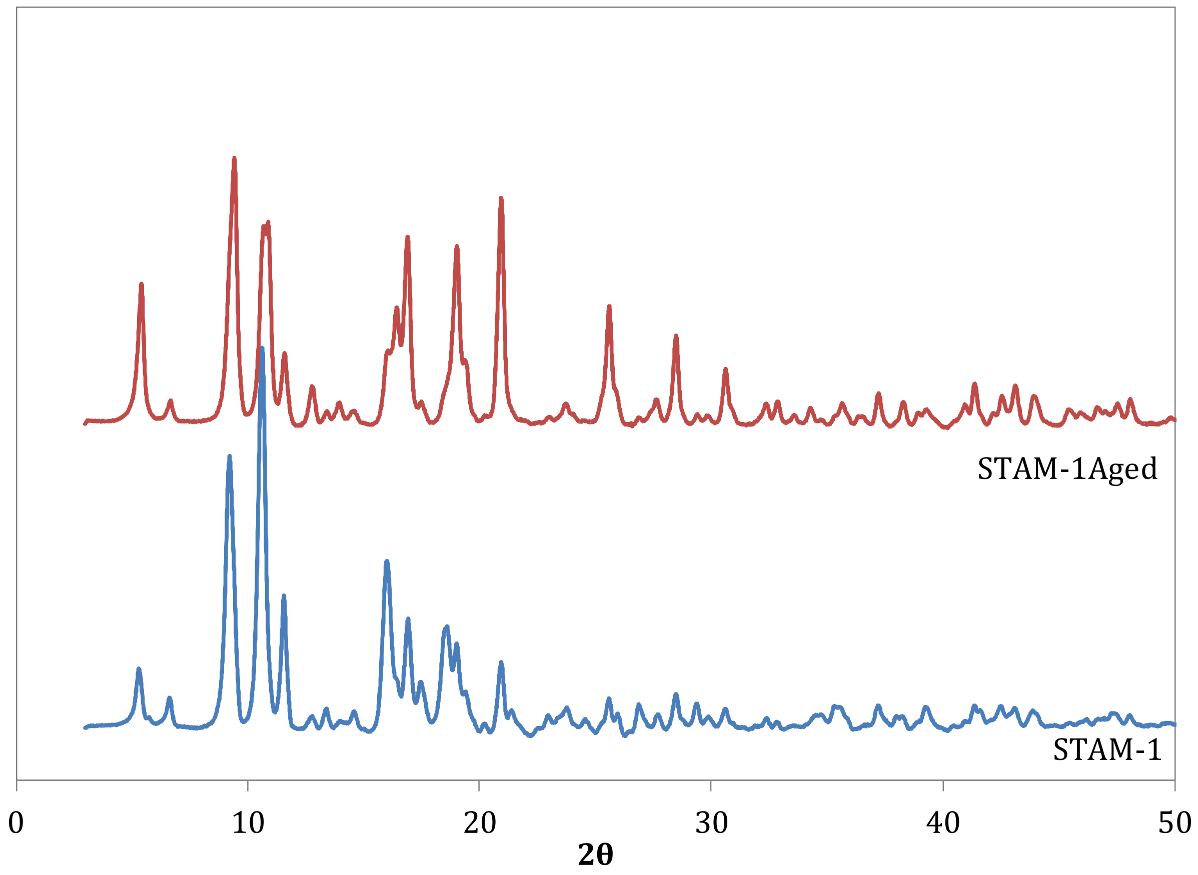

Figure 28: Powder XRD of both as-synthesised and artificially aged STAM-1.

4.6. Enhanced Ammonia Uptake in STAM-1 under Humid Conditions

During the course of the examination of STAM-1 by ammonia micro-breakthrough, an interesting anomaly was noted where unlike most MOFs, the capacity of STAM-1 was found to increase by almost 100% when the adsorption of ammonia on dry samples was conducted under humid conditions compared to those conducted on dry samples in dry conditions.

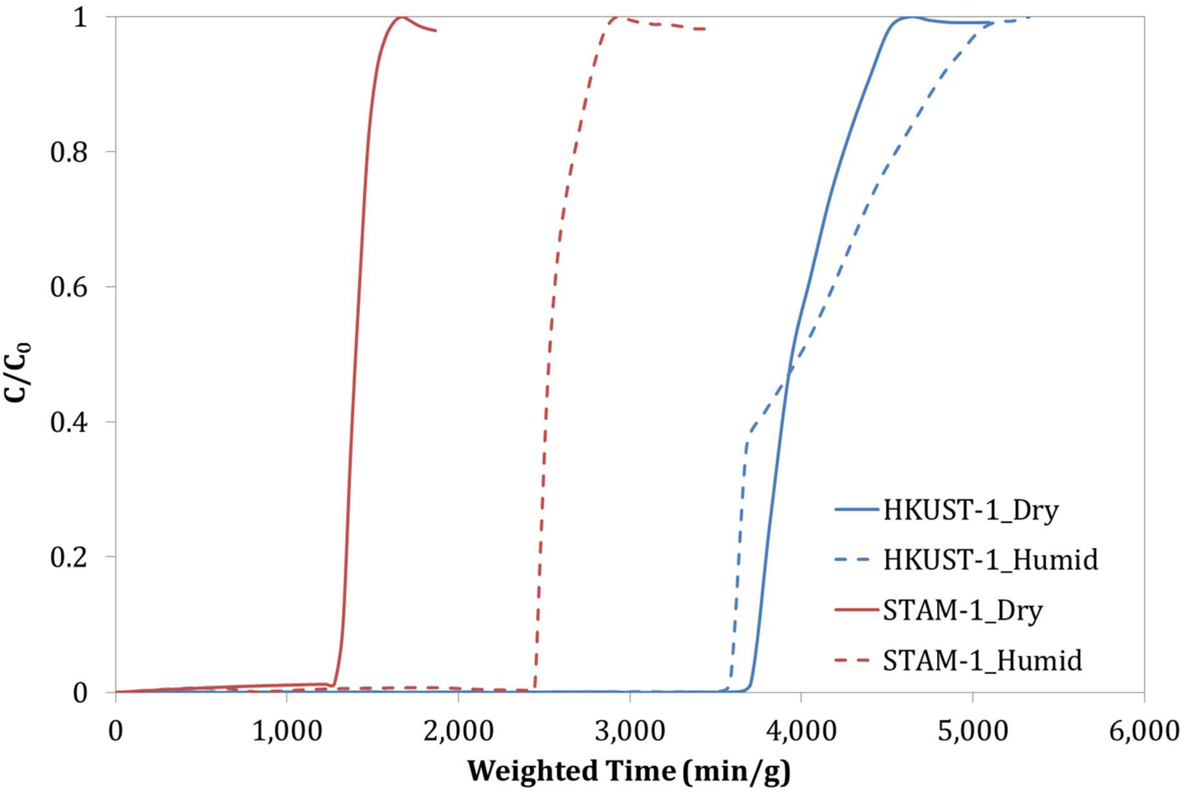

Figure 29: Adsorption of Ammonia in HKUST-1 and STAM-1 in dry (solid) and humid (dotted) conditions.

This result has been replicated over two different breakthrough systems with multiple different batches of STAM-1, indicating that this is a permanent feature of the MOF. It has so far not proven possible to view what has occurred in a single-crystal environment as the crystals degrade too rapidly in the presence of ammonia while in the beamline to continue diffracting. A theory on the mechanism of the ammonia adsorption is presented in section 4.8.

4.7. FTIR Analysis of Ammonia Adsorption in STAM-1

In an effort to further understand the mechanism behind the pronounced increase in ammonia uptake on STAM-1 under humid conditions, investigation into the adsorption of ammonia and other gases was undertaken. The use of in-situ IR measurements of ammonia adsorption was provided by Professor Barbra Gil and her group of Jagiellonian University in Krakow, Poland. This equipment allows for a sample of porous material to be put under vacuum, heated to remove solvent in the pores and then exposed to controlled atmospheres of gases. The solid is monitored by IR spectroscopy and changes in the IR spectrum as a result of gases binding to the structure and gases being removed can be visualised.

First, establishing that ammonia was being adsorbed by the MOF was investigated by comparing the IR pattern of STAM-1 to the patterns of HKUST-1 and to Cu-ZSM-5, a zeolite that has been infused with copper. When exposed to ammonia, the copper in Cu-ZSM-5 begins to form copper diamine complexes which can be observed by the appearance of peaks in the 3400-2800cm^{-1} region of the spectrum.

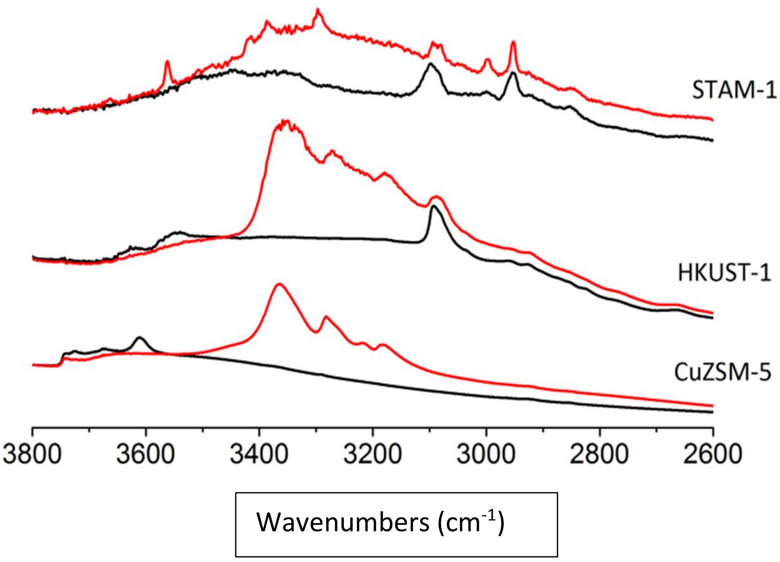

Figure 30: IR Spectrum of Cu-ZSM-5, HKUST-1 and STAM-1 after exposure to an ammonia atmosphere. The black lines represent the dehydrated sample and the red lines indicate the samples that had been exposed to ammonia.

As can be seen in Figure 30, a broad band is visible in the region of 3400-2600 cm^{-1} in the spectra of samples that have been exposed to ammonia. The two MOFs also show an appearance of a broad signal, however the individual peaks that are generated indicate that a different process may be occurring in STAM-1, perhaps indicating potential binding modes that are not accessible in HKUST-1. There is also a sharp peak occurring at 3590 cm^{-1}, which would normally be indicative of gaseous ammonia E-type vibrations, which has one stretching N-H, one oscillating N-H bond and the third N-H bond is functionally stationary. Interestingly, this signal persists even after the IR chamber was evacuated post-ammonia exposure, suggesting that ammonia remains within the structure. In order to obtain more information about the state of bonding within the pores, further analysis by IR required the use of deuterated ammonia (ND_3) to be able to determine further information about the binding of ammonia to the copper centres in STAM-1.

When the samples of STAM-1 were de-solvated by heating under reduced pressure (150°C), the initial IR shows bands that indicate the continuing presence of water. However, upon the introduction of the ammonia, these bands are no longer present, suggesting that the ammonia is capable of displacing water from the copper sites, which is surprising given that typically in the case of MOFs, water has the highest binding affinity for the metal centres. It is also possible that the ester group present inside the pores is participating in a reaction where the ammonia reacts with the carbonyl group in the presence of water which results in the formation of an amide and the production of methanol.

The appearance of the wide band over the region of 3400-3200cm^{-1} is characteristic of ammonia being present and bonded to a copper atom in the structures used. However there are several distinct peaks, different to those that appear in the known samples, which suggest that the binding mode occurring in the samples is not exactly the same as those in HKUST-1 and Cu-ZSM-5. In order to determine if the binding is physisorption or chemisorption, samples were exposed to an ammonia atmosphere, then they were placed under vacuum and the temperature of the chamber was raised in an attempt to remove the ammonia from the structure. After first placing the ammonia-loaded sample under vacuum, the temperature was then progressively raised from ambient conditions to 150°C. The results of this are shown in Figure 31.

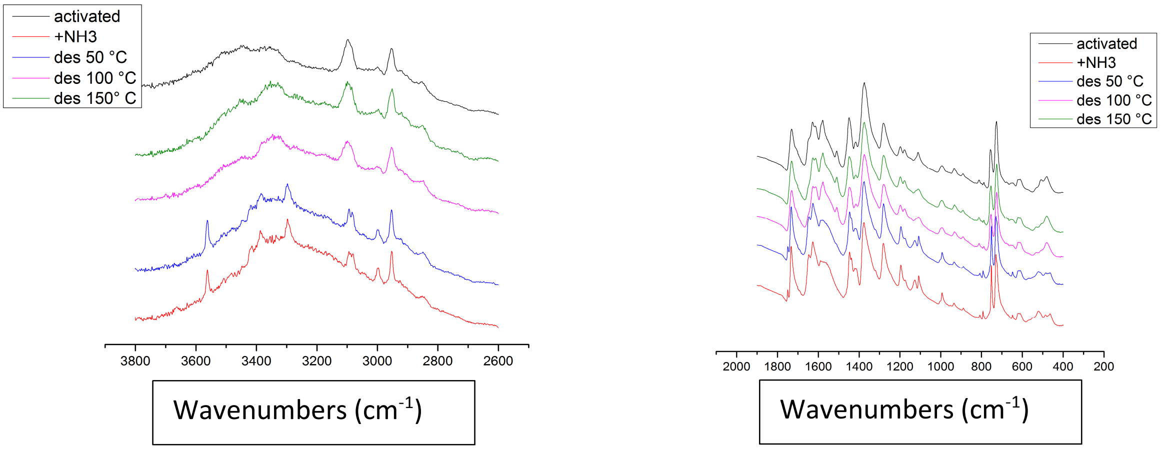

Figure 31: FTIR Spectrum of STAM-1 before and after ammonia exposure, with temperature programmed desorption of ammonia at 50° C, 100° C, and 150° C. High frequency region (left) and low frequency region (right).

After initial ammonia loading, the new peaks at 3000-3400cm^{-1} appear as previously described. Upon heating of the exposed samples, there is little change observed at 50°C, indicating that the ammonia is still bound to the copper centres and is unlikely to be displaced by other atoms in the pores of the material. As the temperature is raised to 100°C, the peaks indicating ammonia adsorption are no longer seen. This suggests the removal of ammonia from the copper centres, though there is still a general broad band apparent that was not present in the dehydrated samples suggesting that even if the ammonia has desorbed from the metal centres, a structural change has occurred in the material. This may be due to incomplete desorption of the ammonia but it is difficult to quantify the amount of ammonia present as the organic portions of STAM-1 occupy the same bands as ammonia's IR signal, making it difficult to determine if other ammonia signals are present and being masked by those of STAM-1.

To further investigate the strength of the bond now formed between the nitrogen and copper atoms, the material was exposed to a humid atmosphere for twenty minutes before being examined by IR. Due to the ease with which water binds to metal centres, if the ammonia is loosely bound, it will be displaced by the water molecules and subsequently removed by evacuation of the chamber.

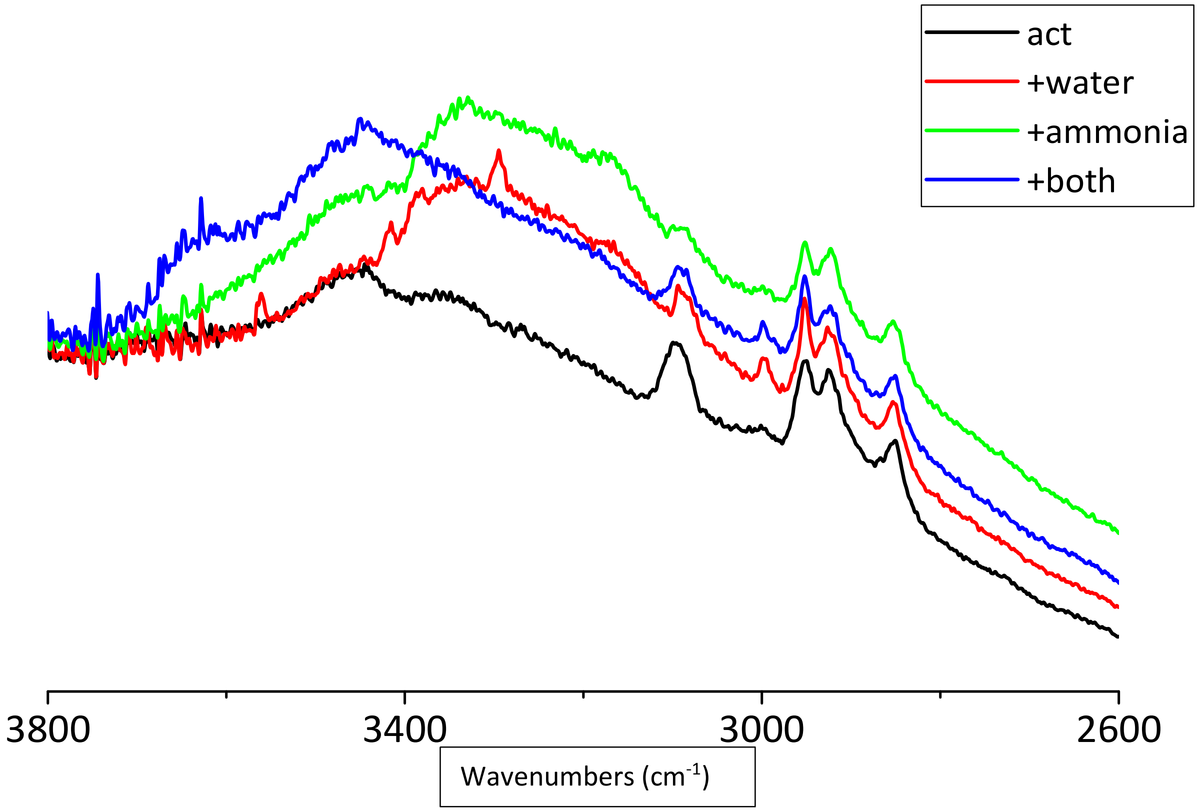

Figure 32: FTIR Bands of sample of STAM-1 ammonia and water uptake and ammonia and water co-adsorbed into the sample.

Figure 32 shows the results of this experiment with the changes in the observed bands. The difference between the activated material and the adsorption of ammonia and the adsorption of water is quite clear, where both generate a broad band over the 3400-3800cm^{-1} region. The material that has been exposed to ammonia then water in sequence shows a broader band with a shift in the position of the peaks alongside the loss of a sharp band around 3300cm^{-1}. This is indicative of both types of molecules being present in the structure at the same time and as such that the ammonia is not displaced by the water, meaning that the interaction between the copper centre and the ammonia is a chemical bond rather than a physical interaction.

This could also be attributed to the hydrophobic and hydrophilic pores providing two different environments for the uptake of ammonia and subsequent interaction with water to occur. As such, this does not further the understanding of the method by which the ammonia is binding to the material. As it was not possible to determine the binding mode with the use of NH_3, the use of deuterated ammonia (ND_3) was considered instead, which gives different bands when measured under IR compared to NH_3 as a result of the increased atomic weight. Due to the shift of the bands that occurs during the use of isotopes, this can potentially allow us to see signals that were previously obscured by signals generated by STAM-1 with normal ^1H atoms.

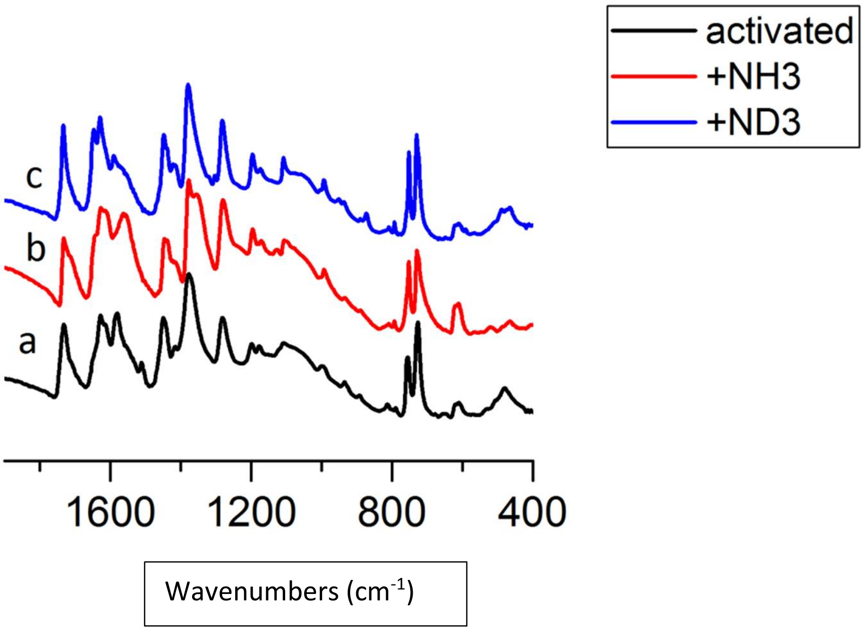

Figure 33: Comparison of adsorption of NH_3 and ND_3 in STAM-1 in the low frequency region.

The comparison between the adsorption of NH_3 and ND_3 is shown in Figure 33, where only small differences related to the position of the framework occur in the low-frequency region. These small discrepancies do not give any further information regarding the binding of ammonia or ND_3 in the structure. As such, it is concluded that both the high-frequency region and the low-frequency region of IR are unsuitable for observing the binding of ammonia. The only remaining region that has not been fully investigated so far is the region of 2800-1600cm^{-1}.

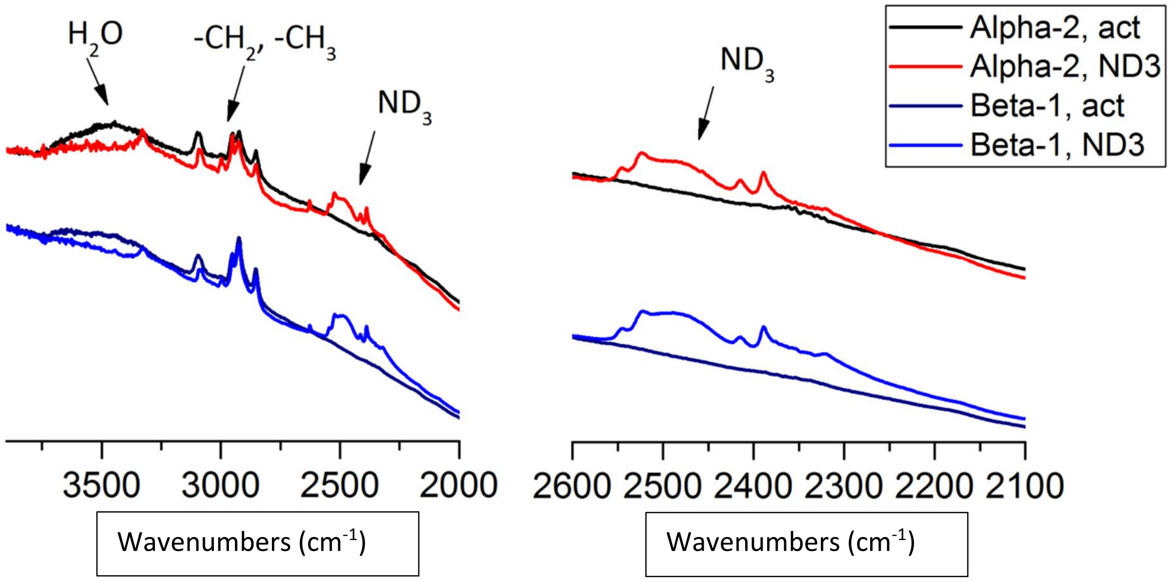

Figure 34: Comparison of STAM-1 with residual water peaks and ammonia loaded samples of same STAM-1 in the high frequency regions.

The comparison of the two regions above gives us some insight into whether the material is truly taking up ammonia and displacing water to do so. In the high-frequency region, the broad signal cantered at 3500 cm^{-1} indicates some residual water remains in the structure after evacuation. In the ND_3 exposed samples, the spectra no longer indicates the presence of water in the material after evacuation. The exposed material however displays an ammonia signal which is visible in the 2600-2400 cm^{-1} region and is not observed in the activated material. This signal persists through evacuation of the chamber, indicating a strong binding of deuterated ammonia to the metal-centre. This persistence through the evacuation of the chamber is evidence of a stronger bond than the physisorption of water molecules to the metal-centre, indicating this is a chemisorptive process that produces a chemical bond that will require elevated temperature and reduced pressure to remove the ammonia from the material. As a respirator material, this is an important property which will ensure the safety of those wearing the apparatus from accidental gas release.

A thermo-desorption of the ammonia exposed material was done under IR to determine whether the ammonia was likely to be easily removed from the STAM-1 material in conditions it is likely to be exposed to in “real-world” applications.

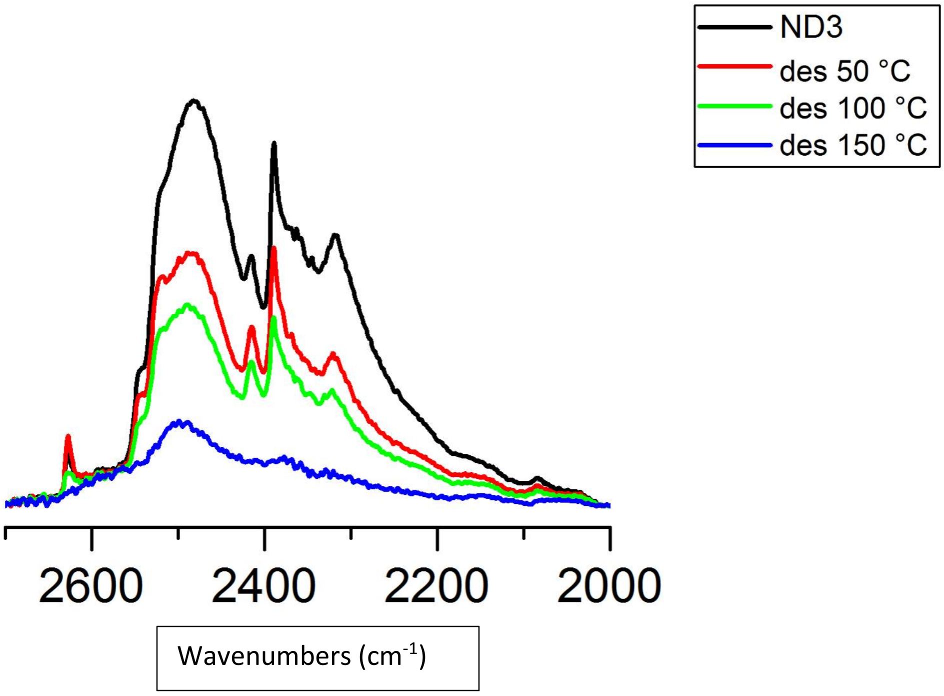

Figure 35: Thermo-desorption of ammonia from STAM-1 exposed to ammonia atmosphere.

The signal observed for the ammonia loaded material displays a high intensity, which shows a minor decrease as the temperature is raised to 50℃ and still displays a signal approximately half as intense at 100℃ indicating a large proportion of the ammonia bound in the structure remains. The rapid degradation of the signal at 150℃ suggests that the ammonia has been removed from the structure at this temperature. As part of further testing the capabilities of the material, the sample was loaded with ammonia and then exposed to a humid atmosphere to determine the effect of additional water on ammonia in the structure (Figure 36).

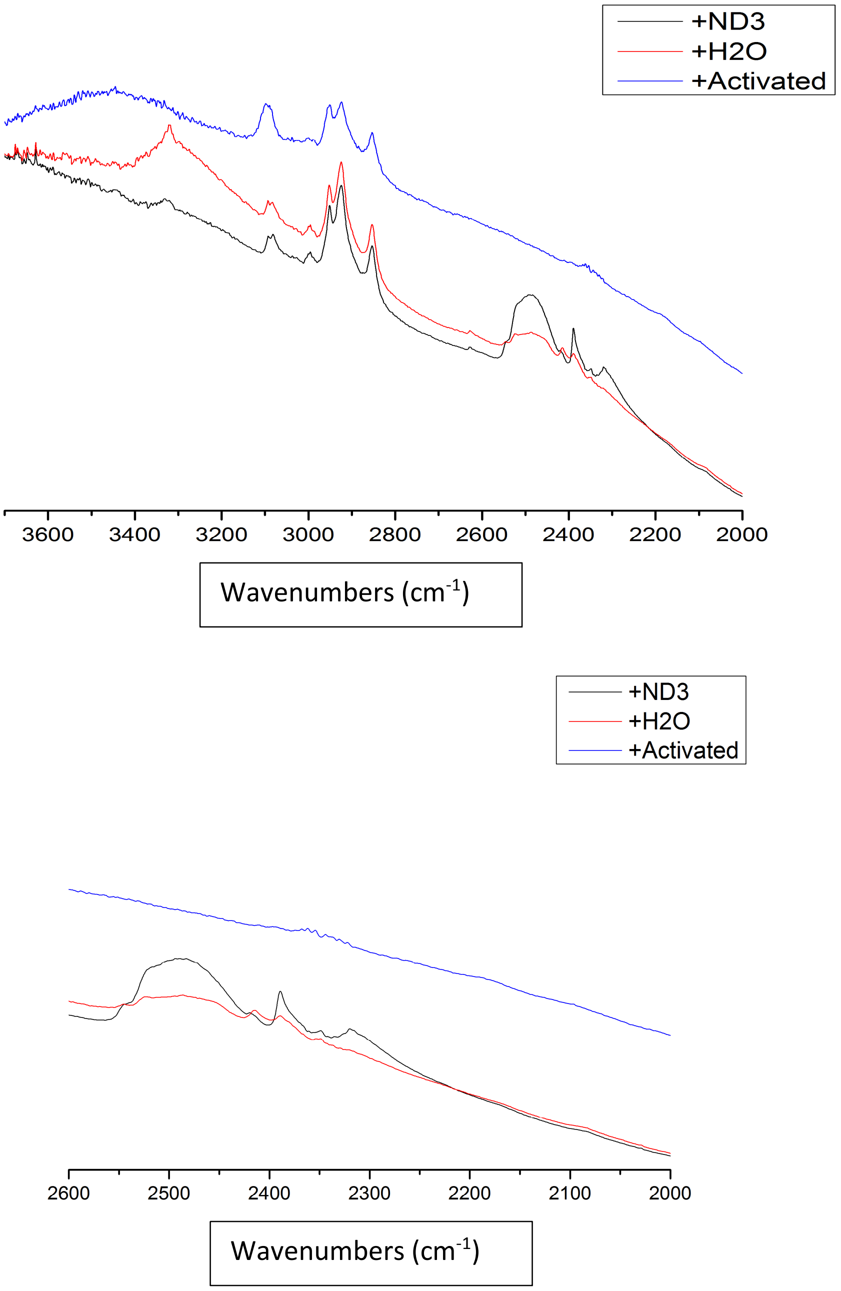

Figure 36: FTIR spectra of H_2O and ND_3 co-adsorption, spectra at 50℃. First, ND3 excess is adsorbed and shortly evacuated then H2O excess is adsorbed and shortly evacuated.

There is a noticeable decrease in the ammonia signal, suggesting that not all ammonia is permanently bonded to the structure. This would be consistent with a lack of availability of open metal sites in the dehydrated material which would have quantities of free ammonia within the pores which would be displaced easily by the incoming water. The remaining ammonia in the hydrophobic pores evacuates more slowly due to the kinetic gating mechanism of the hydrophobic pore.

While the work done here gives strong evidence for a strong bond forming that is unlikely to release significant quantities of ammonia from the structure after adsorption even when exposed to other molecules, this method of binding is not conclusively proved.

4.8. Mechanism of Ammonia Uptake and Improvement in Humid Conditions

The improved capacity of STAM-1 for ammonia in humid conditions represents an interesting shift in the adsorption of gases from humid air. In HKUST-1, initially, water appears to improve ammonia uptake, as the ammonia dissolves in the water but as adsorption continues, the framework collapses, leaving $Cu(OH)_2$ and $(NH_4)_3$btc.[8] The post-ammonia uptake XRD indicates the framework remains intact in the case of STAM-1 in humid and aged samples and in the case of both dry and aged samples, there is little variation in the capacity for ammonia uptake, suggesting a single avenue for storage in dry and aged samples. While our FTIR work has shown that in certain conditions it appears that ammonia can displace water from metal-centres, it is more likely the breathable properties of STAM-1 are the most likely area to explain the large increase in observed ammonia capacity of the MOF.

STAM-1 was originally reported as showing a “breathing” of the structure when transferring between the hydrated and dehydrated states.[1,3] This was originally posited to be the hydrophobic pores opening and closing but this has been revised to indicate that when the hydrophilic pores are fully evacuated, a structural change occurs in the material which results in the copper acetate lanterns of the material changing their orientation, causing the hydrophilic pores to “breathe” shut. With 67% of the pores of the material closed, the ammonia uptake is restricted to only the void volume in the hydrophobic channels.

The ammonia uptake displayed by this material is reasonably effective compared to other MOFs examined during the course of this project and has produced consistent results when the material is fully dehydrated. In the trials run under humid conditions the material shows excellent uptake of ammonia, increasing almost by 100% over dry conditions and consistently giving a strong uptake in humid conditions that have been shown to degrade HKUST-1 over time. After the use of *in-situ* FTIR did not elucidate a full mechanism, further experiments were attempted to verify the mechanism by which ammonia was being taken up in the structure using synchrotron crystallography, and MAS NMR studies.

4.9. Variable Temperature PXRD on STAM-1 and Related Compounds

The “breathing” of the channels in STAM-1 has yet to be fully visualised under single-crystal conditions due to a loss of single-crystal character when the sample is dehydrated. The process can be observed using variable temperature PXRD. The technique is identical to standard PXRD except the chamber that the sample is mounted in can be controlled in both temperature and atmosphere.

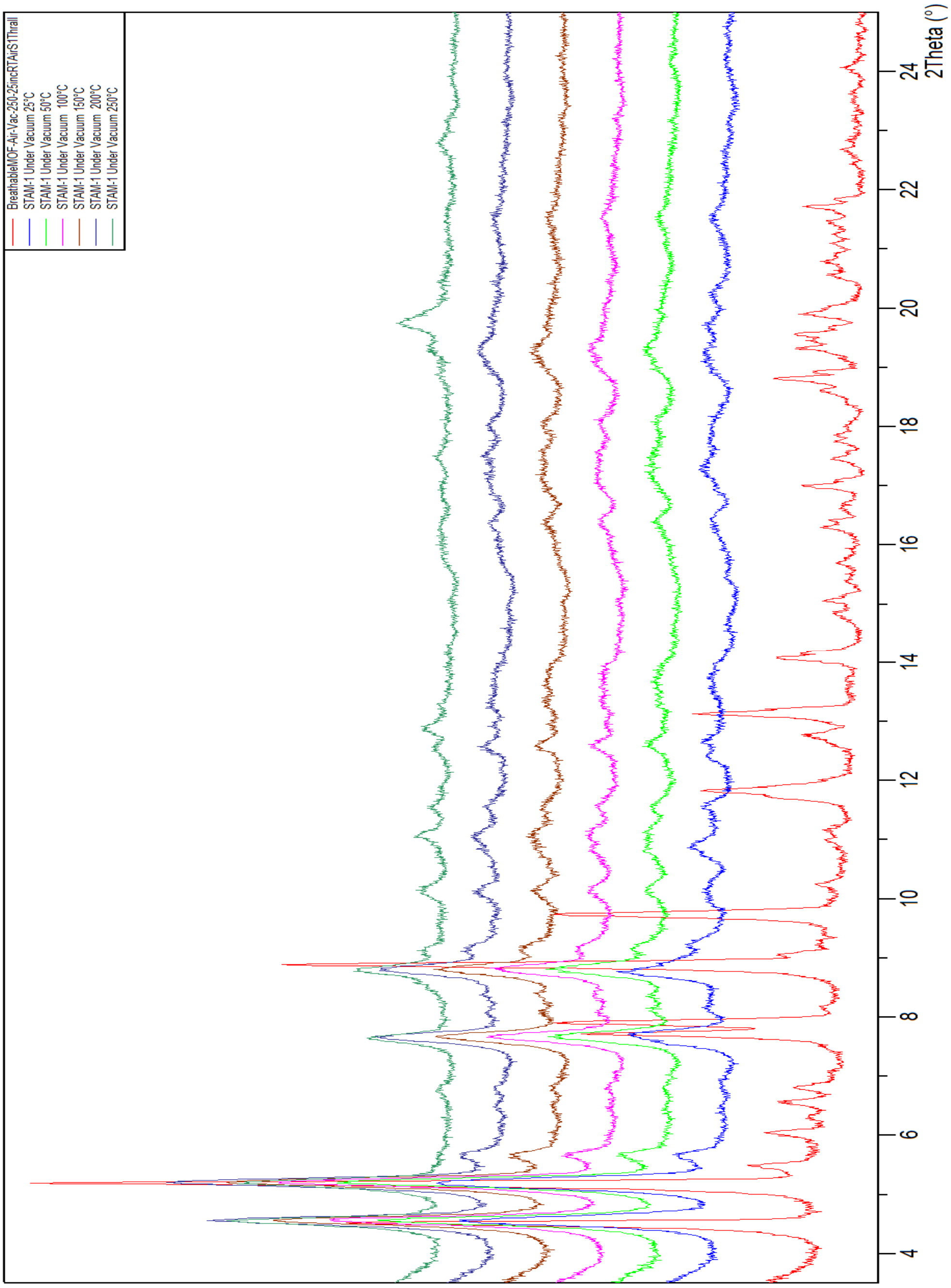

Figure 37: VT PXRD of STAM-1 under vacuum from RT to 250 rising. The "breathing" rearrangement occurs as soon as the material is placed under vacuum.

The material undergoes an immediate change when it is placed into a low pressure environment and maintains it throughout the rising temperature. Due to the low vacuum used, the sample begins to burn at 250°C causing the appearance of a copper oxide peak at 20°.

Being able to visualise the structural rearrangement in PXRD while useful, ultimately did not allow us to speculate on a potential mechanism for the uptake of ammonia by STAM-1 in humid conditions. Within the REM Group, Dr. Laura McCormick had produced a series of related compounds which produced a Kagome lattice arrangement similar to that of STAM-1. These new MOFs are produced by the use of 5-isophthalic acid derivatives.

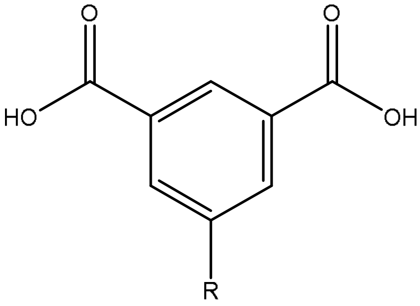

5-isophthalic acid

Figure 38: A series of new MOFs using functionalised 5-isophthlaic acid derivatives have been produced and show the same structure as STAM-1.

A sample of one of these new MOFs Cu(EtOip)(H_2O) which uses 5-ethoxyisophthalic acid (H_2EtOip) as the organic ligand, was synthesised and examined using VT PXRD with the same conditions as those used on STAM-1 (Figure 39).

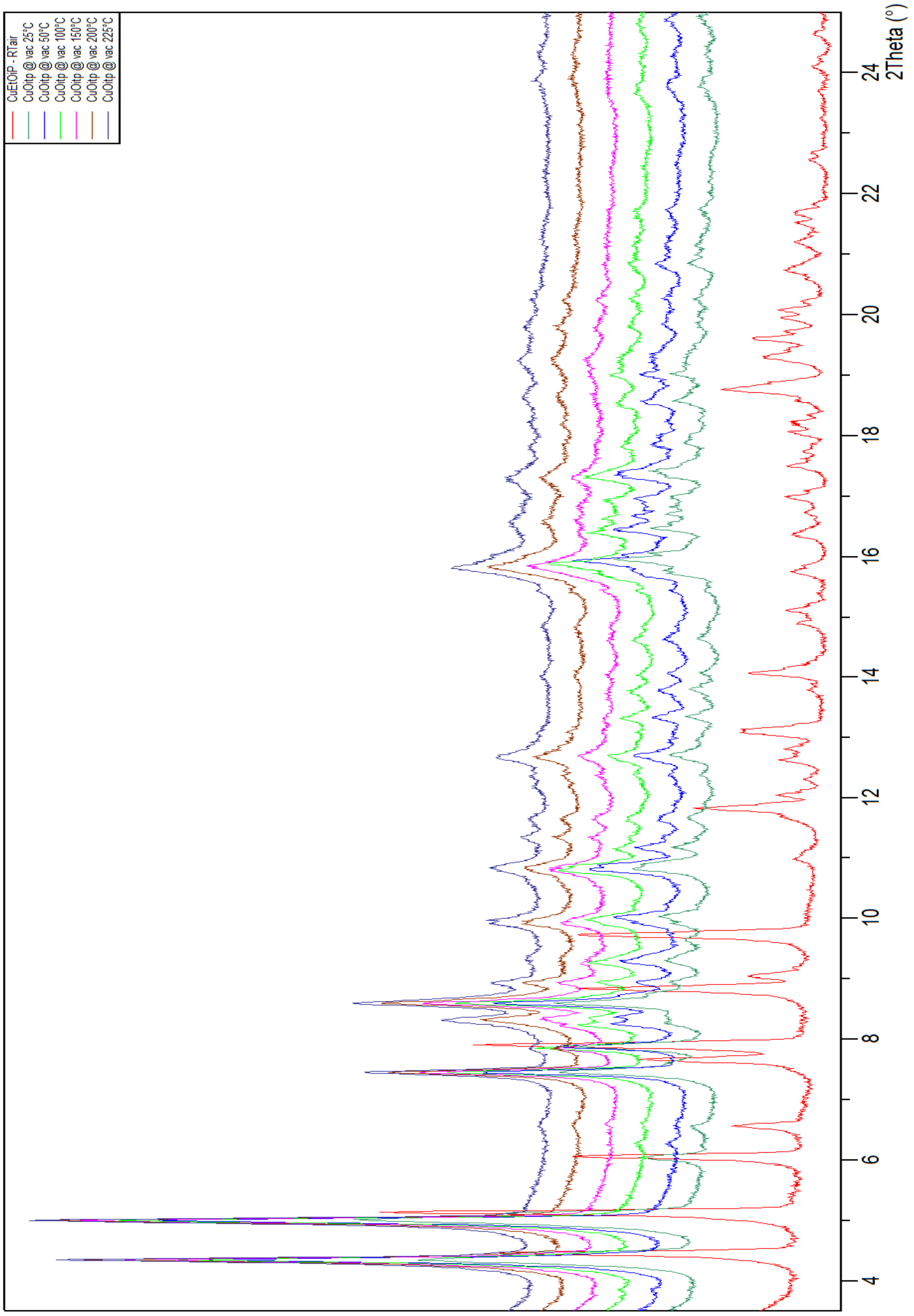

Figure 39: VT PXRD of Cu(EtOip)(H_2O) MOF being heated from ambient temperature to 523K in 25, displaying the same breathing change as STAM-1.

The material undergoes the same rearrangement as STAM-1 but as can be seen in (Figure 40) also returns to the previous arrangement after exposure to a flow of nitrogen with 10%RH. Under ambient conditions, the return to the hydrated phase is slower.

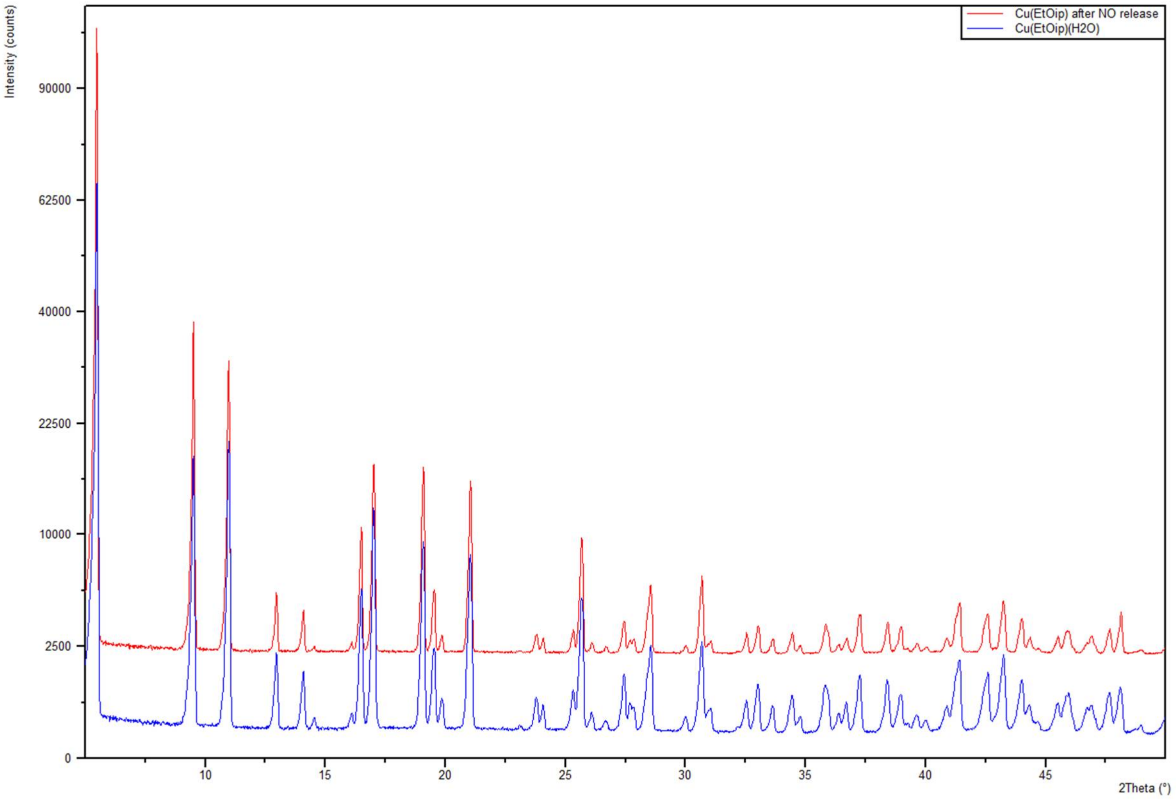

Figure 40: Pre and Post VT PXRD patterns of Cu(EtOip)(H_2O). Sample was allowed to rehydrate under ambient conditions.

What is perhaps most interesting about this material is that when it enters the rearranged phase, it retains enough single-crystal character for the altered structure to be observed.

4.10. Single Crystal Diffraction of similar Kagome lattice MOFs for visualisation of structural rearrangement.

The structure of STAM-1 was obtained and found to be identical to that reported by Mohideen *et al*.[1]

The work was undertaken at the Advanced Light Source in Berkeley, California at the 11.3.1 beamline by Dr Simon Teat who developed a gas cell in collaboration with Dr Phoebe Allan and Dr Catherine Renouf which allows for the *in-situ* observation of crystals exposed to static atmospheres of different gases.

The crystal of STAM-1 was placed mounted into the beamline and a structure obtained before partial evacuation of the chamber was attempted in order to introduce ammonia into the gas cell. The low pressure environment causes the structure to undergo a rearrangement which as previously reported results in the loss of single-crystal character. Due to the limitations of the gas cell setup which in order to achieve a flow through the cell which could allow the binding of ammonia in the “open” state would have required the venting of gas into an area occupied by personnel. As a result, the safety risk was deemed too high to successfully image the material using this apparatus.

This work attempts to generate a satisfactory explanation of the changes that occur within STAM-1 during the structural rearrangement, comparisons were made with an analogous series of MOFs derived from 5-alkyl or alkoxy isophthalic acids that have been recently developed in the Morris group by Dr Laura McCormick.[9] These ligands when reacted with copper acetate, produce a series of MOFs which are iso-structural with STAM-1, exhibiting the same dual-pore system and breathing behaviour. There is a growing series of 5-substituted isophthalate MOFs which exhibit this same Kagome-lattice pore arrangement, modified with a series of functional groups including alkoxy,[10,11] alkyl[12], azido[13], sulfonate[14] and alkyl-amino.[14]

The 5-ethoxy isophthalic acid derivative was examined using single-crystal XRD and was found to crystallise in the trigonal space group $P\bar{3}m1$. The structure and crystallographic information for the material are shown below (Figure 41).

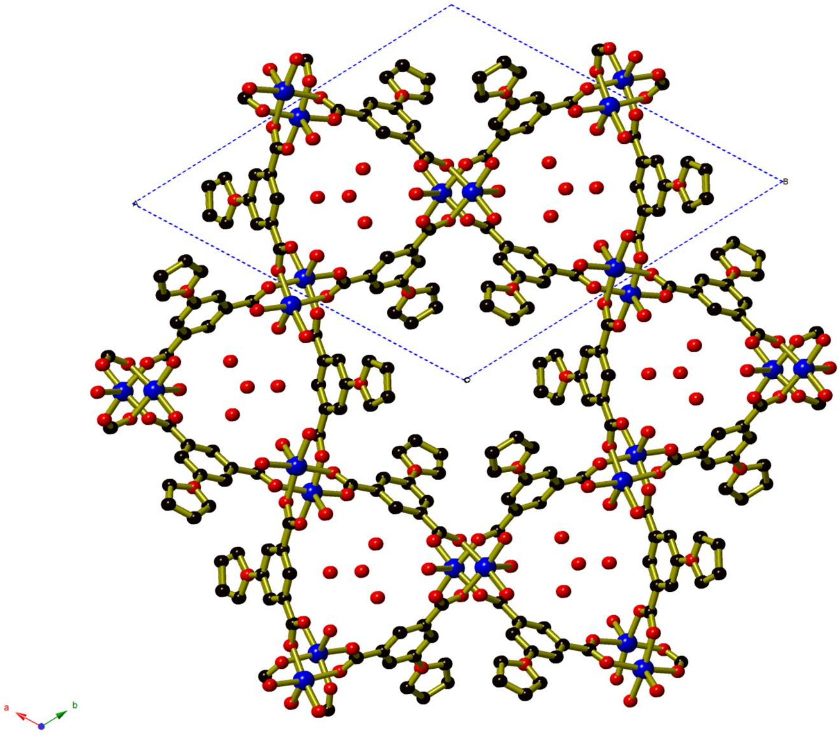

Figure 41: Copper 5-ethoxy isophthalate 2D MOF displays Kagome lattice topology with hydrophobic and hydrophilic pores. Key: C: Black, O: Red, Cu: blue. Hydrogen atoms omitted for clarity.

This material is isostructural with STAM-1. All copper centres and all ligands are crystallographically equivalent. The ethyl chain projects into the hydrophobic channel and is disordered over two symmetry relate sites.

The hydrophilic channels are occupied by disordered water molecules. The structure is made up of parallel sheets which are held together by hydrogen bonds between the coordinated H_2O molecules and the carboxylate group oxygen atoms.

Table 3: Crystal Structure Data for Cu(EtOip) Frameworks[9]

	Cu(EtOip)(H_2O)·0.67H_2O	Cu(EtOip)
Molecular formula	$C_{10}H_{11.33}CuO_{6.67}$	$C_{10}H_8CuO_5$
Temperature (K)	300	300
λ (Å)	0.77490	0.77490
Crystal system	Trigonal	Trigonal
Space group	$P\bar{3}m1$	$P31m$
a (Å)	18.5676(12)	33.028(3)
b (Å)	18.5676(12)	33.028(3)
c (Å)	6.8056(6)	5.20147(6)
V ($Å^3$)	2031.9(3)	4917.0(10)
Z	6	18
ρ_{calcd} (g cm^{-1})	1.479	1.652
μ (mm^{-1})	2.060	2.529
F(000)	922	2466
GoF	1.059	1.101
Reflections collected/ unique/parameters	26279/2174/95	26548/4168/188
R_{int}	0.0673	0.0955
Final *R* indices ($I>2\sigma(I)$)	$R1 = 0.0384$ $wR2 = 0.1023$	$R1 = 0.1503$ $wR2 = 0.3249$
Final *R* indices (all data)	$R1 = 0.0496$ $wR2 = 0.1087$	$R1 = 0.1666$ $wR2 = 0.3362$

This crystal data is in the process of being published.[9] This structure is different to STAM-1 in that while it undergoes the structural rearrangement that was confirmed by VT PXRD (Figure 39), it does not lose single crystal character in the dehydrated state, allowing for a structure to be elucidated. The dehydrated form has a significantly different structure to the original hydrated material (Figure 42).

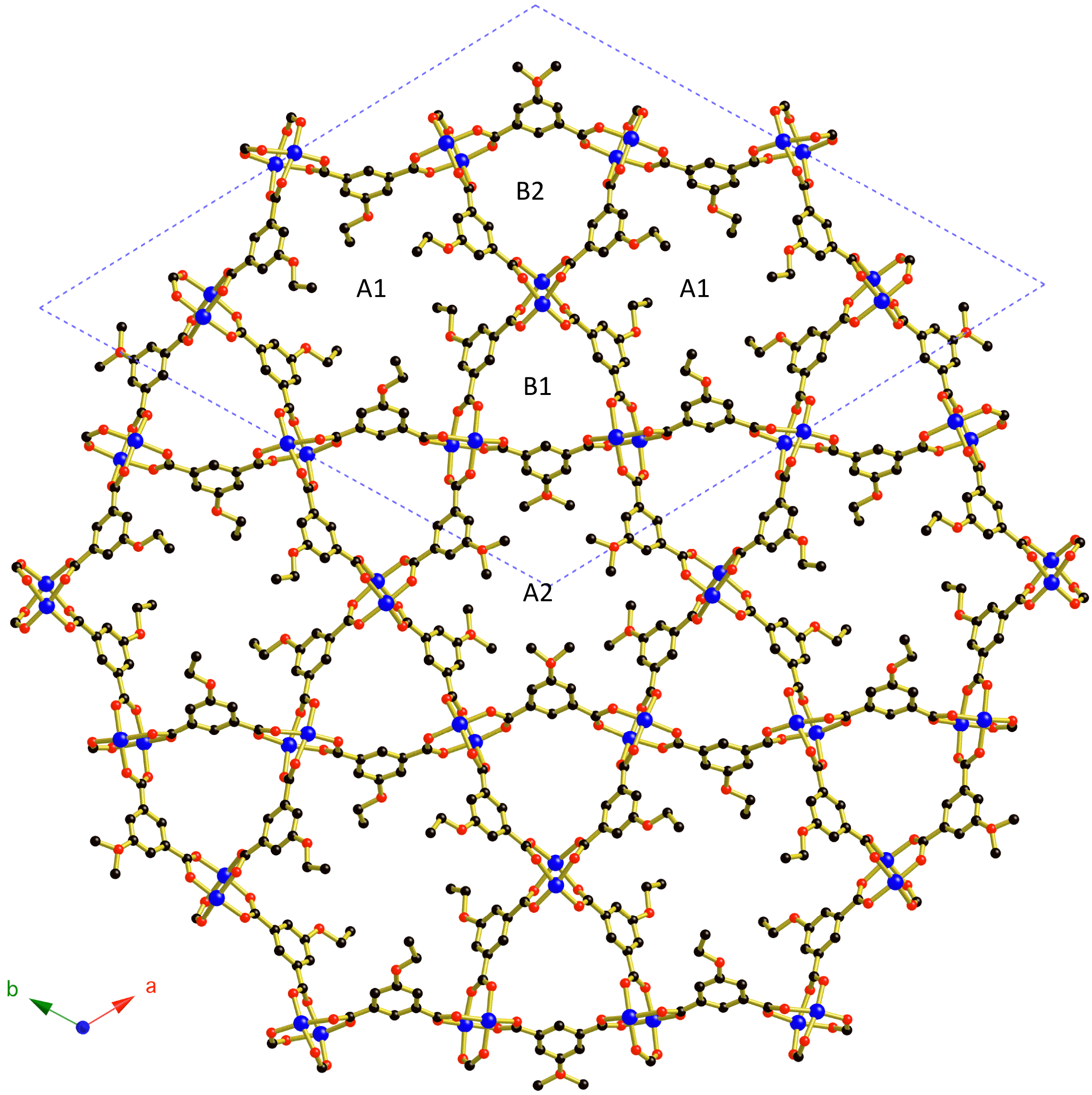

Figure 42: Dehydrated structure of CuEtOip. Pores are labelled to indicate hydrophobic (A) and hydrophilic (B) character. Key: C: Black, O: Red, Cu: blue. Hydrogen atoms omitted for clarity.

There are now four different types of channel present in the structure, with two crystallographically distinct hydrophobic and hydrophilic channels in the material and four distinct copper-centres arranged in two distinct copper acetate lantern units. The removal of the coordinated water molecules generates a vacant coordination site on every copper centre. On one of the copper acetate units, a carboxylate oxygen atom from an adjacent sheet binds to this vacant co-ordination site, cross-linking the Kagome sheets into a 3D coordination framework. This vacant site on the remaining copper acetate dimer remains unoccupied as neighbouring type 2 dimers are misaligned due to the deformation of the Kagome lattice below the water molecules are shown with hydrogen bonding. The difference in coordination environments of the copper acetate units of the hydrated and dehydrated crystals may be seen by comparison of Figure 43 and Figure 44 respectively. When the structure is hydrated, hydrogen bonds form between the co-ordinated water molecules and carboxylate oxygen atoms of copper acetate units on adjacent sheets (Figure 43).

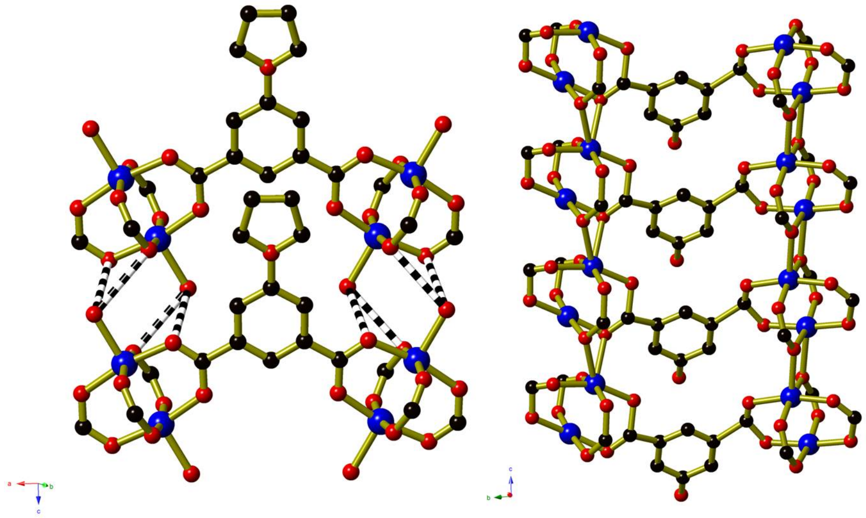

Figure 43: The hydrated (left) and dehydrated (left) arrangement of the copper acetate lanterns in Cu(EtOip). Hydrogen bonds are shown as black and white striped bonds. Key: C: Black, O: Red, Cu: blue. Hydrogen atoms omitted for clarity.

When the structure is dehydrated, the new local structure is shown in Figure 44.

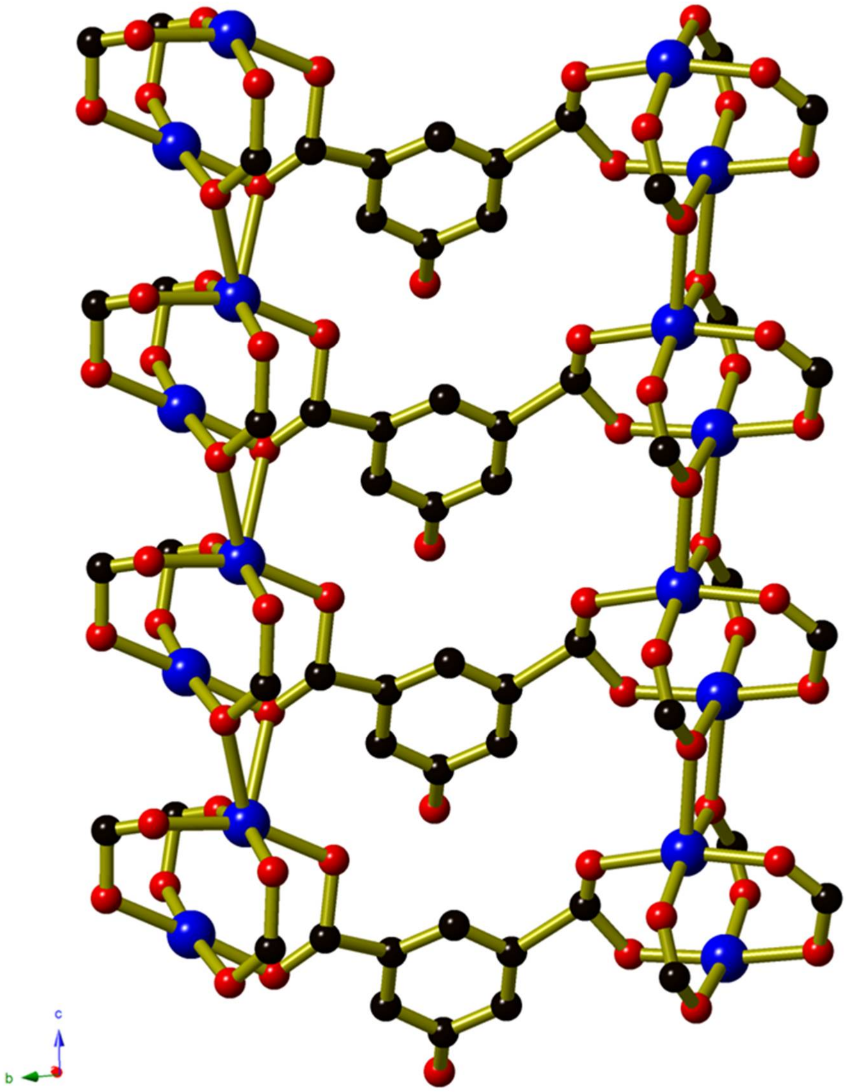

Figure 44: The deformed copper acetate lanterns of the Cu(EtOip) crystals. Key: C: Black, O: Red, Cu: blue. Hydrogen atoms omitted for clarity.

Without the water molecules providing hydrogen bonding, one of the carboxylate oxygen atoms binds in the Jahn-Teller elongated coordination site. This causes deformation of the sheet, which then causes the pores of the material to effectively close. The difference between the closed and open pores of the material is shown below in Figure 45 & Figure 46.

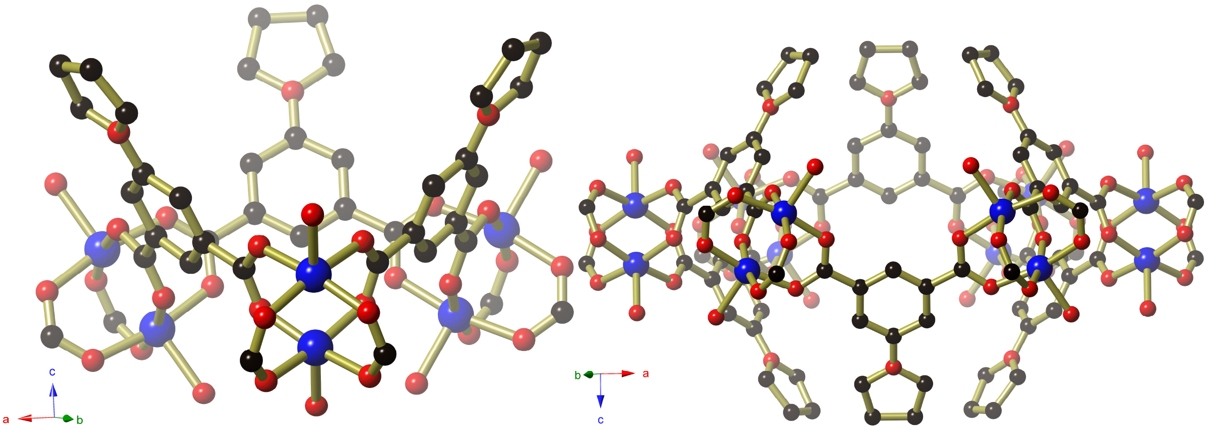

Figure 45: A side-on view of the channels in the hydrated structure of Cu(EtOip)(H_2O). Key: C: Black, O: Red, Cu: blue. Hydrogen atoms omitted for clarity.

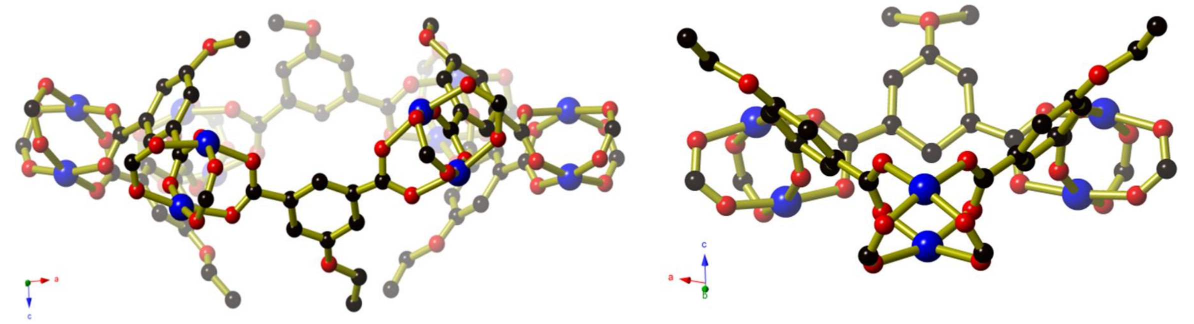

Figure 46: A side-on view of the channels in the dehydrated Cu(EtOip) structure. The hydrophilic pore is blocked by the ethoxy groups, restricting gas molecule passage. Key: C: Black, O: Red, Cu: blue. Hydrogen atoms omitted for clarity.

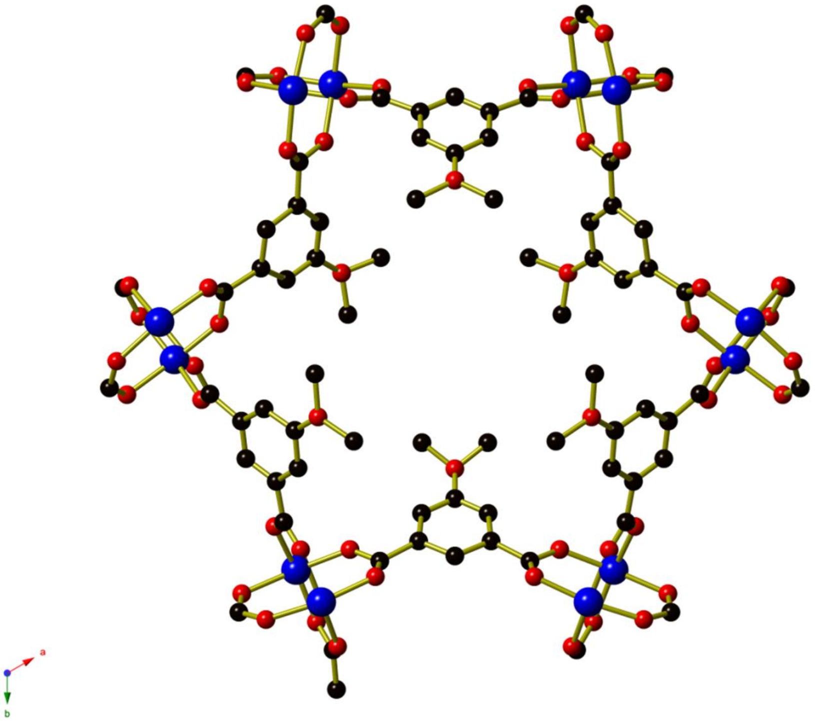

Figure 47: Hydrophobic pore of CuEtOip. Alkyl groups are disordered over two sites. Key: C: Black, O: Red, Cu: blue. Hydrogen atoms omitted for clarity.

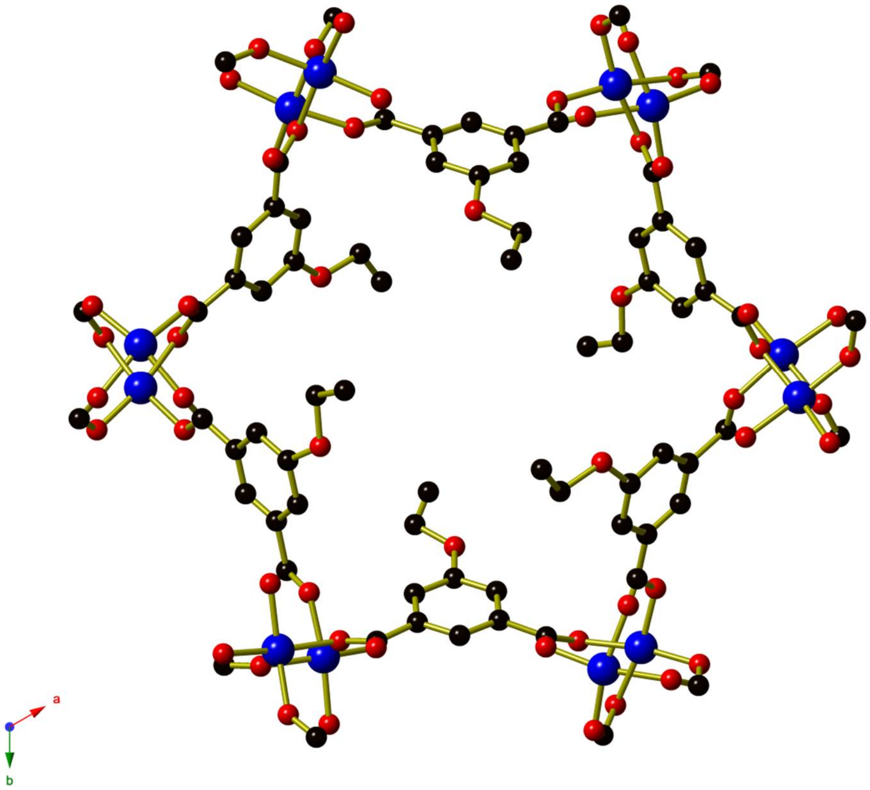

Figure 48: Second distinct hydrophobic pore in CuEtOip. The ethyl chain can be clearly seen in this pore. Key: C: Black, O: Red, Cu: blue. Hydrogen atoms omitted for clarity.

In the dehydrated structure, the loss of pendant water molecules results in a rearrangement, causing the ligand to obscure both pores, which reduces the effective pore diameter of both pores to the point where gas molecules cannot enter into the hydrophilic pores. As water molecules move into the dehydrated structure, they bind back to the copper-acetate lanterns, which results in the alkoxy groups being removed from blocking the pores, restoring the original Kagome framework, opening up the pore for gases to enter.

4.11. Mechanism of Ammonia Uptake in Kagome Lattice MOFs

Based on the changes in structure observed in the MOFs discussed earlier in the chapter and the published work of Kitigawa *et al*[13] which examines CO sorption in the 5-azido-isophthalate derived MOF, a mechanism has been proposed for the uptake of ammonia in these MOFs. This is shown in Figure 49. In the dry MOF (Figure 49.b), exposed to dry ammonia (Figure 49.c), the hydrophilic pores are constricted by the change in the coo-ordination environment of the copper acetate lanterns described in Section 4.10. This is an effective change of approximately 0.4 Angstroms in the 5-ethoxy-isophthalate MOF. Given that the kinetic diameter of ammonia is smaller than the remaining opening which is approximately 4.8 Angstroms,[9] this would suggest that the pore is not truly closed and the effect is largely kinetic , resulting in the material appearing to reach breakthrough and saturation, due to the flow rate outpacing the uptake by the MOF.

Conversely when the material begins to take up a humid ammonia stream, the pores begin to relax into their open (hydrated) state, which reduces the kinetic effect on ammonia and water uptake. Based on the FTIR studies conducted, it appears that the ammonia can also displace water from the copper-site, suggesting the hydrophilic pores are filled with a mixture of ammonia and water as the gas stream continues to open the pores for transport (Figure 49.d). As the displacement occurs, the ammonia binds to the copper centres, releasing water. This explains the increased breakthrough time for the material in humid condition. Where the material is already saturated with water, the rate of ammonia uptake into the hydrophilic pores is greatly reduced but the hydrophobic pores are still able to take ammonia into their void, accounting for the maintained capacity in aged material (Figure 49.e)

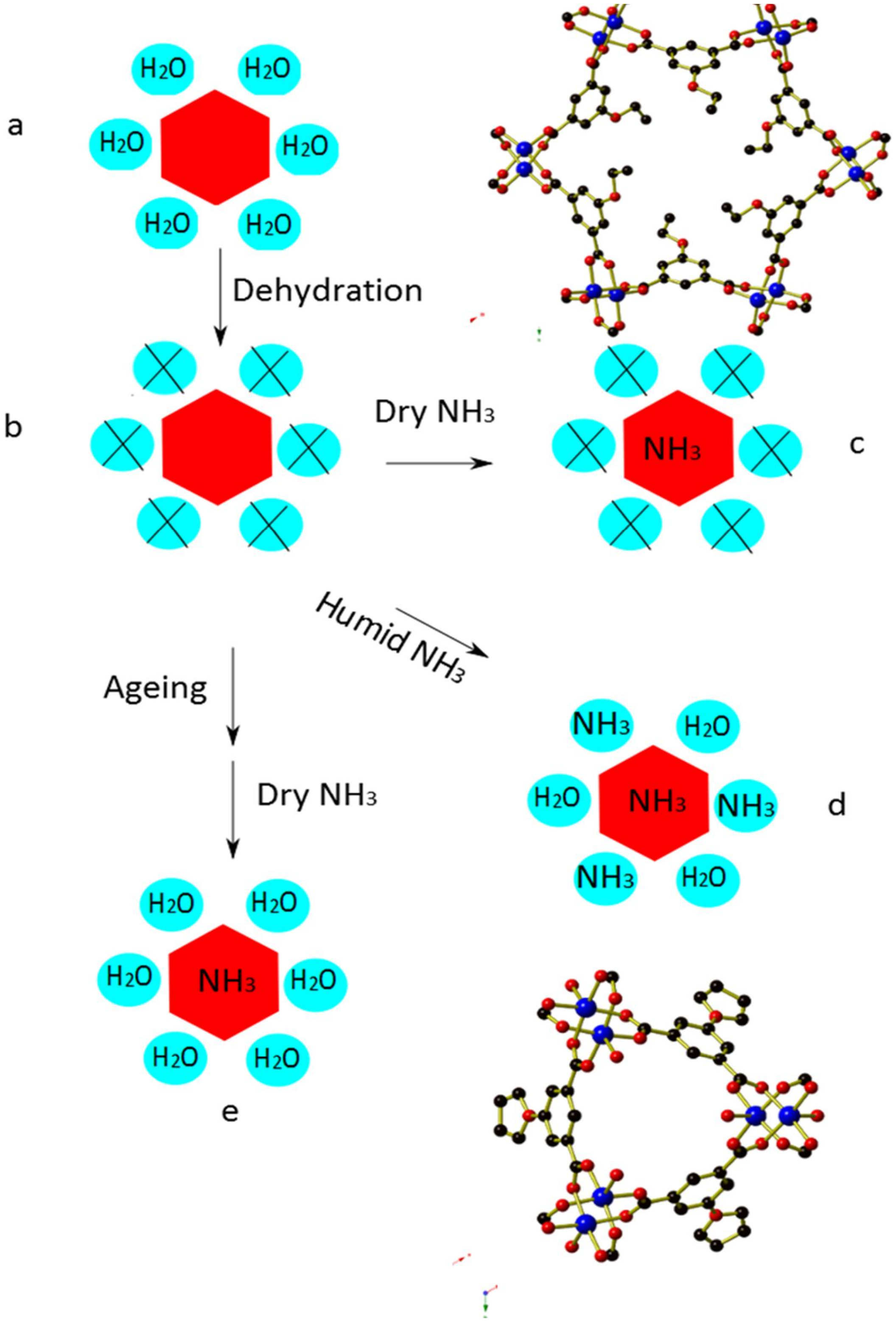

Figure 49: Proposed Mechanism of Ammonia Uptake in Kagome Lattice MOFs. The red hexagons indicate a “hydrophobic” pore and the blue circles indicate “hydrophilic” pores.

4.12. Solid State NMR Analysis of STAM-1 and 5-isophthalate derivatives.

To further characterise the adsorption of ammonia in STAM-1 and the iso-structural derivatives produced by McCormick *et al*,[9] MAS solid state NMR was used to attempt to determine the binding mode of ammonia in the samples. This work was carried out in collaboration with Dr. Daniel Dawson and final year project student Charlotte Sansome. Initial spectra on as-synthesised STAM-1 is shown below (Figure 50)

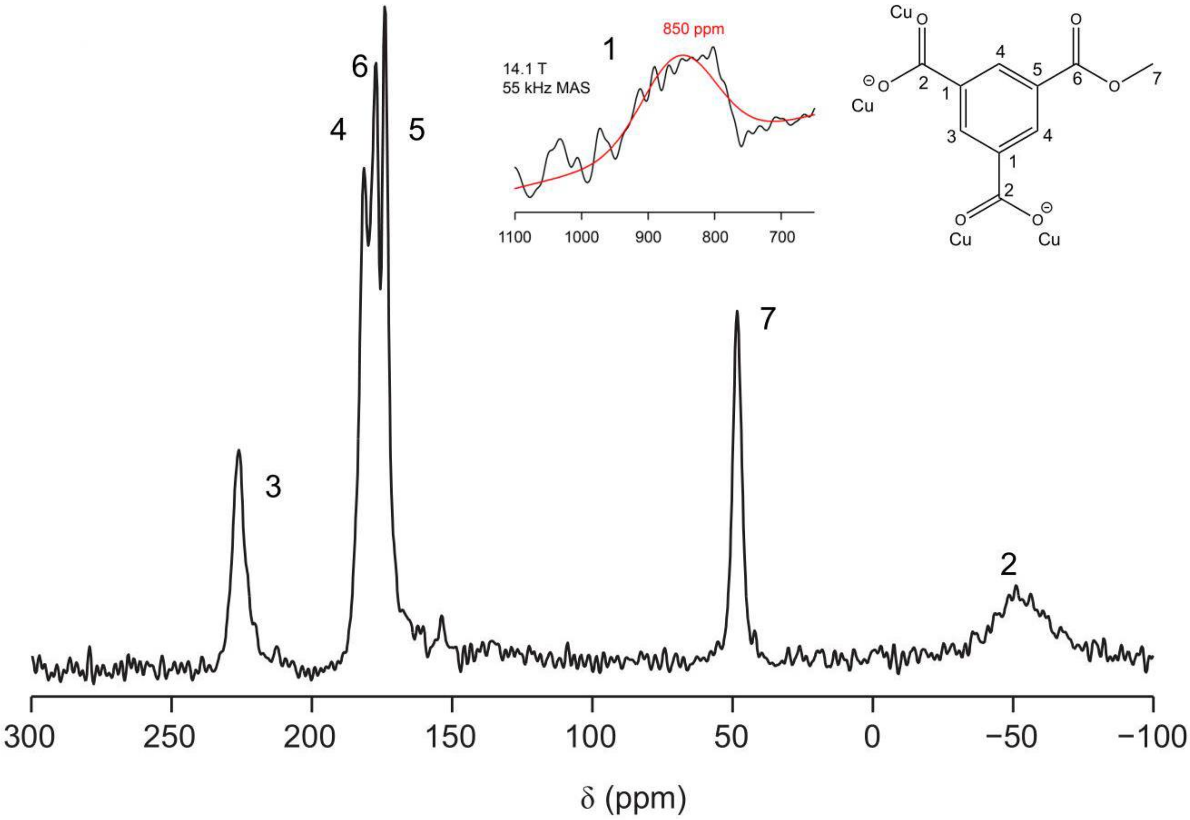

Figure 50: ^{13}C (9.4 T, 37.5 kHz DP-MAS Spin-echo pulse sequence) NMR spectrum of STAM-1 with inset showing peak at 850 ppm. Inset peak was recorded under 14.1 T at 55 kHz DP-MAS.

The spectrum of STAM-1 is shown in Figure 50. The benzene ring carbon atom (C1) connected to the carboxylate-Cu bond display a peak at 850 ppm and shown in the inset. Previous work on high resolution MAS NMR on STAM-1 and dealing with the challenges of characterisation of a para-magnetic copper containing material has been published by Dawson *et al* and contains full characterisation of HKUST-1 and STAM-1.[15] Spinning sidebands have been minimised by use of high speed spinning.

The MAS NMR spectrum of the novel structure of McCormick *et al*[9] is shown in Figure 51.

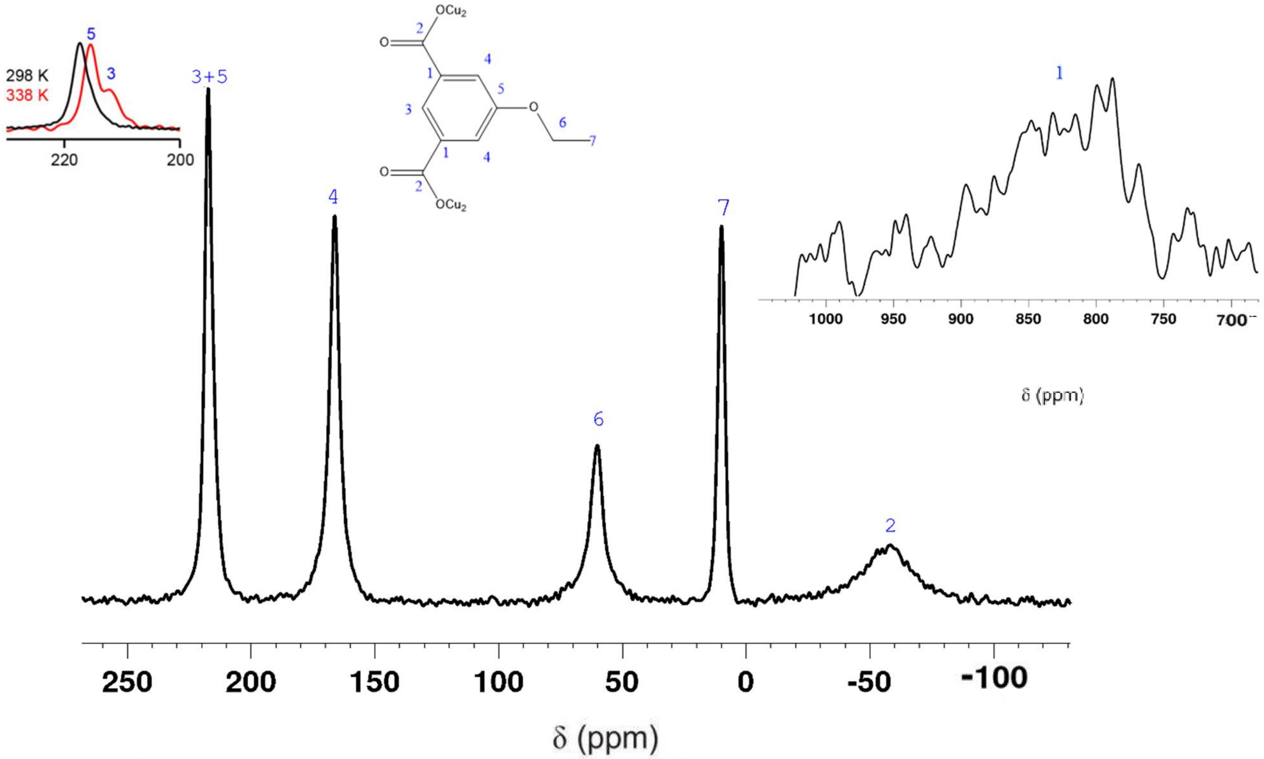

Figure 51: ^{13}C (9.4 T, 37.5 kHz DP-MAS with spin-echo pulse sequence) NMR spectrum of CuEtOip MOF and comparison of 298K vs 338K in left inset. Right inset shows broad signal over 830 ppm indicating C1 atom. Inset ^{13}C (14.1 T 55 kHz DP-MAS).

Table 4: Peak positions, integrals and assignments for CuEtOip.

δ_{iso} (ppm)	Integral	Suggested Assignment
830	N/A	C1
217	2	C3+C5
166	2	C4
60	1	C7
10	2	C6
-58	N/A	C2

The carbon atoms are assigned in Table 4 and display a slight shift from that observed in STAM-1 but is explained by the proposed theory that carbon atoms close to paramagnetic Cu^{2+} centres exhibit a higher temperature-dependent shift differences.[15,17] Although there are similarities between the two spectra, there has been a considerable shift for some peaks, attributed to the change of the carbonyl methyl ester to an ethyl ether in the 5-isophalate derivative. Particularly notable are movement of the peak representing C5, which is now located at 217 ppm and can only be observed by conducting experiments at increased temperature (Figure 51, left insert). To support the evidence that the 5-

ethoxy isophthalate derivative material undergoes a structural shift when fully dehydrated, an NMR was collected on the dehydrated material. This is shown in Figure 52.

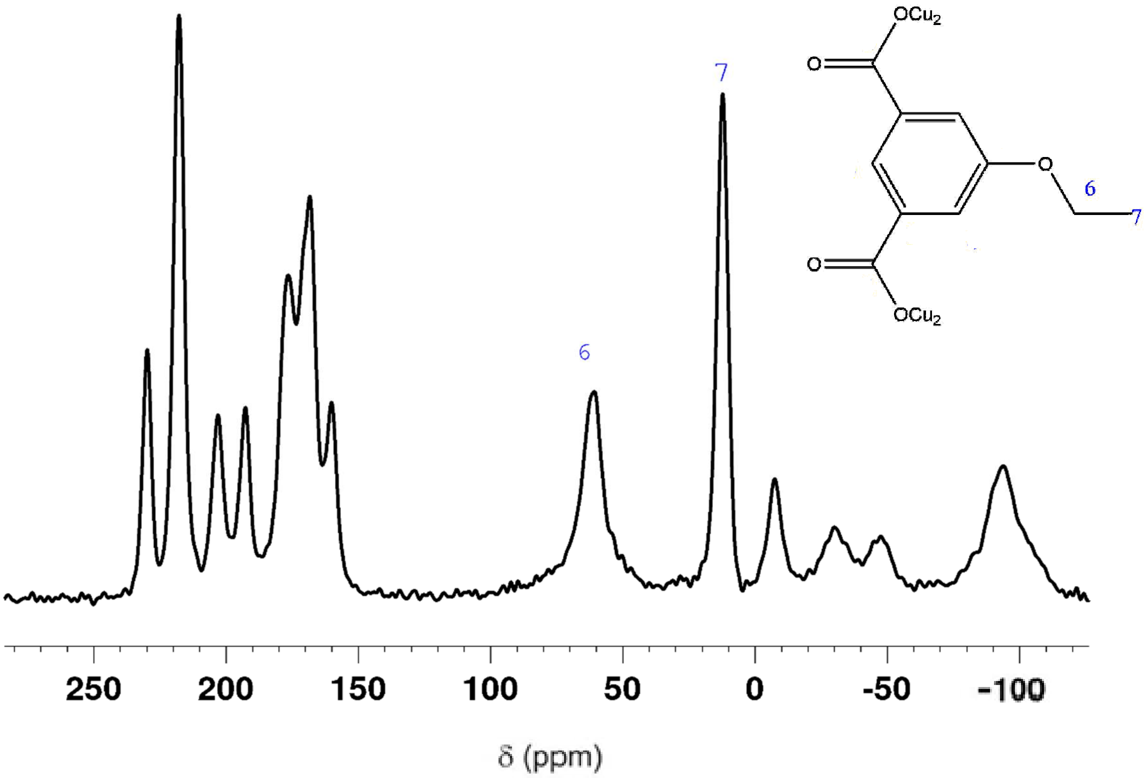

Figure 52: ^{13}C (9.4 T, 37.5 kHz DP-MAS with spin-echo pulse sequence) NMR spectrum of CuEtOip MOF in dehydrated state. Carbons C6 and C7 are still visible but carbons C2-5 have split into multiple peaks. The C1 peak has not yet been recorded in the dehydrated material.

The splitting of the signals representing C2-C5 correlate with the deformation of the structure that occurs as a result of dehydration. The two distinct copper acetate lanterns, which give rise to four unique copper centres result in the carbons C2-C5 each having a unique environment. With the current data, it is not possible to assign the peaks to specific carbon atoms. In an attempt to determine the assignment of the peaks, cross-polarisation was used.

A CP experiment was carried out, using a contact time of 100 µs on the ethoxy isophthalate derivative, shown as a comparison in Figure 53. Relaxation times were determined by use of inversion recovery experiments.[16]

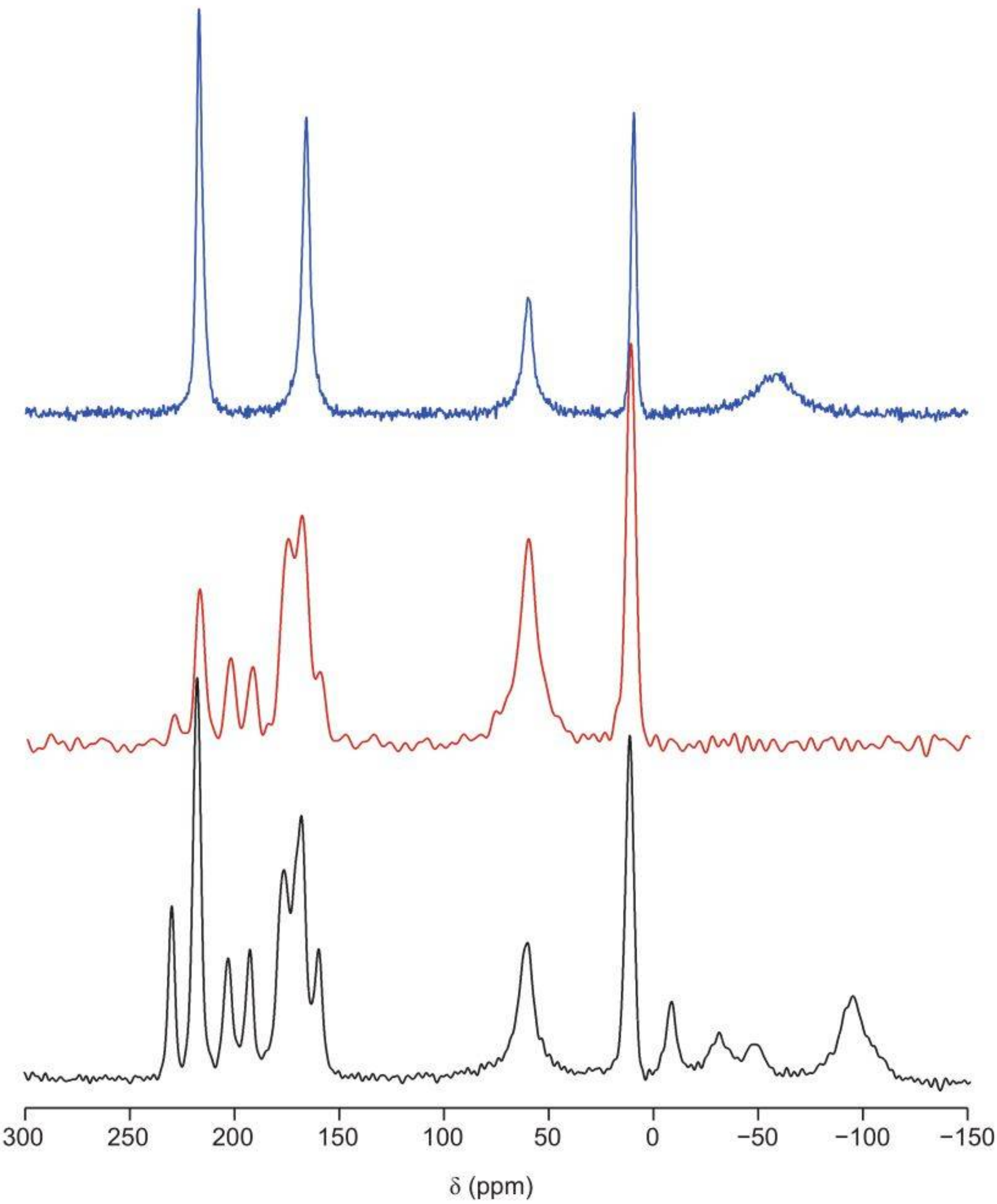

Figure 53: Comparison of ^{13}C (9.4 T, 37.5 kHz DP-MAS) NMR spectrum of dehydrated ethoxy isophthalate MOF (black), ^{13}C (9.4 T, 37.5 kHz CP-MAS) of dehydrated ethoxy isophthlate MOF (red) and 13C (9.4 T, 37.5 kHz DP-MAS) hydrated ethoxy isophthalate derived MOF (blue).

The CP-MAS NMR shows a loss of the signal for peaks below 0 ppm, indicating they represent quaternary carbon atoms and in this structure likely represent the carbonyl carbon (C2). Integration of these peaks shows a 1: 1: 1: 3 integrated intensity ratio. The peaks, integration and relaxation times are shown in Table 5. As mentioned earlier in the chapter, the dehydrated structure displays four unique copper arranged in two copper acetate lanterns, which gives six unique carboxylate (C2) carbon environments, matching the assignment detailed below. Further evidence for the assignment is suggested by the reduction of the signal intensity of peaks at 230 ppm and 218 ppm, which are reduced by over 90% and 67% respectively, indicating the presence of a quaternary carbon (C5) within these peaks. The incomplete removal of the 218 ppm peak suggests that a CH environment carbon (C3) is present as this would not be reduced by use of CP. Peaks in the region 176 ppm – 160 ppm also do not exhibit any intensity loss, again indicating a CH environment and occupying the same region as the C4 carbon in the hydrated MOF, suggesting that this region also shows the C4 carbon in the dehydrated MOF. Peaks in the range of 230 ppm – 193 ppm show an integrated intensity ratio of 1: 3: 1: 1: 6. Assignment of the peaks to these values is supported by the T_1 relaxation constants, with larger T_1 for C4 and C5 containing peaks. Due to the quaternary nature of C1, CP reduces the signal intensity and it cannot be observed in CP experiments.

Table 5: Peak positions, relative integrals (rounded to nearest integer), T_1 values and tentative assignment of dehydrated ethoxy isophthalate derivative MOF.

δ_{iso} (ppm)	T_1 / ms	Integral	Assignment
230	23.6	1	C5
218	26.1	3	C3/C5
203, 193	12.9, 13.2	1, 1	C3
176, 170,168 , 160	N/A, 16.3, N/A, 19.2	6 (total)	C4
61	N/A	N/A	C6
12	N/A	N/A	C7
-8, -30, -47, -93	N/A	N/A	C2

This assignment of the dehydrated 5-ethoxy isophthalate derived MOF will aid in the potential derivation of the structure of STAM-1 and is to be investigated in future work.

Investigation of the uptake of ammonia by STAM-1 was also examined by MAS solid-state NMR. A comparison of the as-synthesised material compared to the loaded material is shown below (Figure 54).

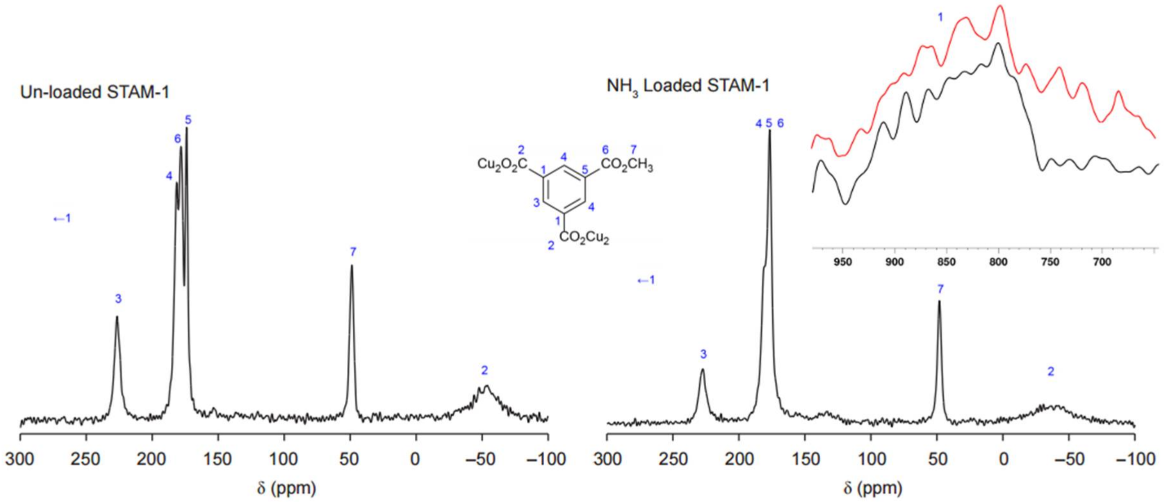

Figure 54: ^{13}C (9.4 T, 37.5 kHz DP-MAS with spin-echo pulse sequence) NMR spectrum STAM-1 (left) and ammonia loaded STAM-1 (right). The ammonia loaded material shows shifts in the peaks. Inset shows C1 peak in STAM-1 (black) and ammonia loaded STAM-1 (red). High region collected using ^{13}C (14.1 T 55 kHz DP-MAS).

The signals for STAM-1 shift when exposed to ammonia, causing the peaks for C4, C5 and C6 to merge together. C2 appears to diminish in signal and there is some variation in the C1 peaks, suggesting an effect on the copper atom. This suggests that the ammonia is binding to the copper centre but it cannot be proved definitively with this experiment alone. A possible assignment of the peaks is given in Table 6

Table 6: Peaks, Integrals and tentative assignment of carbon atoms for ammonia loaded STAM-1

δ_{iso} (ppm)	Integral	Assignment
830	N/A	C1
227	1	C3
176	4	C4, C5, C6
48	1	C7
-30	N/A	C2

An attempt to determine the mechanism of binding using MAS ^{15}N NMR was attempted but no signal for ^{15}N was observed. This may be due to the low sensitivity of ^{15}N as a result of the negative gyromagnetic ratio it possesses or could be due to the free motion of ammonia in the pores of the MOF or the material not being successfully loaded with ammonia. Future experiments would require the use of a more sophisticated gas loading apparatus to ensure successful loading and making use of the Insensitive Nuclei Enhanced by Polarization Transfer (INEPT) pulse sequence[18] may be necessary to improve the signal-to-noise ratio so that the ^{15}N signals can be observed.

4.13. Conclusions

STAM-1's previously reported breathing mechanism allows it to take up a significantly increased amount of ammonia from contaminated airstreams under humid conditions and after extended ageing that destroys the supramolecular structure of HKUST-1, which is widely researched for toxic gas uptake. These properties have been investigated by FTIR and MAS NMR, along with single-crystal XRD on iso-structural analogues due to the loss of single crystal character displayed by STAM-1 when dehydrated. FTIR gas-loading experiments point towards a strong chemisorptive uptake of ammonia by the structure. MAS NMR also indicates that uptake occurs around the copper centre, as evidenced by the shifting occurring on ammonia loaded samples of STAM-1 in NMR experiments.

STAM-1 and the iso-phthalate derivatives represent an interesting future study for toxic hydride removal in conditions adverse to MOFs and for potential future industrial production. Further NMR studies would help to shed light on the final location of ammonia that has been taken up into the STAM-1 and *iso*phthalate derivatives, along with in-situ gas loading powder XRD at a synchrotron source will definitively prove the mechanism behind the uptake of ammonia in these MOFs.

4.14. References

1 M. I. H. Mohideen, B. Xiao, P. S. Wheatley, A. C. McKinlay, Y. Li, A. M. Z. Slawin, D. W. Aldous, N. F. Cessford, T. Düren, X. Zhao, R. Gill, K. M. Thomas, J. M. Griffin, S. E. Ashbrook and R. E. Morris, *Nat Chem*, 2011, **3**, 304–310.

2 P. J. M. Stals, P. A. Korevaar, M. A. J. Gillissen, T. F. A. de Greef, C. F. C. Fitié, R. P. Sijbesma, A. R. A. Palmans and E. W. Meijer, *Angew. Chem. Int. Ed.*, 2012, **51**, 11297–11301.

3 M. I. H. Mohideen, Thesis, University of St Andrews, 2011.

4 J. B. DeCoste and G. W. Peterson, *Chemical Reviews*, 2014, **114**, 5695–5727.

5 G. W. Peterson, G. W. Wagner, A. Balboa, J. Mahle, T. Sewell and C. J. Karwacki, *J. Phys. Chem. C*, 2009, **113**, 13906–13917.

6 G. W. Peterson, D. K. Britt, D. T. Sun, J. J. Mahle, M. Browe, T. Demasky, S. Smith, A. Jenkins and J. A. Rossin, *Ind. Eng. Chem. Res.*, 2015, **54**, 3626–3633.

7 G. W. Peterson, G. W. Wagner, A. Balboa, J. Mahle, T. Sewell and C. J. Karwacki, *J Phys Chem C Nanomater Interfaces*, 2009, **113**, 13906–13917.

8 E. Barea, C. Montoro and J. A. R. Navarro, *Chem. Soc. Rev.*, 2014, **43**, 5419–5430.

9 L.J. McCormick, S.A. Morris, M.J. McPherson, D.B. Cordes, A.M.Z. Slawin, S.J. Teat and R.E. Morris, *Manuscript in Preparation.*

10 J. J. Perry, G. J. McManus and M. J. Zaworotko, *Chem. Commun.*, 2004, 2534–2535.

11 A. Mallick, B. Garai, D. D. Díaz and R. Banerjee, *Angew. Chem. Int. Ed.*, 2013, **52**, 13755–13759.

12 X.-F. Wang, L. Li, Y.-M. Kong and Y. Liu, *Inorganic Chemistry Communications*, 2012, **21**, 72–75.

13 H. Sato, W. Kosaka, R. Matsuda, A. Hori, Y. Hijikata, R. V. Belosludov, S. Sakaki, M. Takata and S. Kitagawa, *Science*, 2014, **343**, 167–170.

14 X. Li and Q. Liu, *Z. anorg. allg. Chem.*, 2013, **639**, 1815–1820.

15 D. M. Dawson, L. E. Jamieson, M. I. H. Mohideen, A. C. McKinlay, I. A. Smellie, R. Cadou, N. S. Keddie, R. E. Morris and S. E. Ashbrook, *Phys. Chem. Chem. Phys.*, 2012, **15**, 919–929.

16 P. Hore, J. Jones and S. Wimperis, 2000.

17 D. M. Dawson, Thesis, University of St Andrews, 2014.

18 G. A. Morris and R. Freeman, *J. Am. Chem. Soc.*, 1979, **101**, 760–762.

Chapter 5 Hydrophobic Mesoporous Silica Impregnated with CPO-27 MOFs for Ammonia Uptake and Toxic Gas Removal

5.1. Introduction

When separating any mixture of compounds, the selectivity of the filtering material is one of the most important factors to consider. The filter material will not perform adequately if a common harmless molecule has a stronger binding affinity with the material than the toxic molecules that pose a threat. In MOFs, this particular problem is most often encountered with water. In a laboratory setting and even in some industrial settings, the ability to control water content of the synthesis is available and while adding a degree of complexity and expense to some processes; it is possible to remove water to the extent that it does not affect the uptake of toxic gases by the adsorbent. In a situation like that of a gas mask filter, the element of control is completely removed and the mixtures that the filter material will encounter will vary widely and rapidly depending on the current situation. Due to exposure to humidity, it has been reported in literature and confirmed in Chapter 5, that HKUST-1, a popular MOF for gas sorption studies, has its performance degrade rapidly in the presence of 20% relative humidity.

Other MOFs, such as the CPO-27 series, while not as unstable in the presence of water, have their open-metal sites occupied by water molecules. Water displays an extremely high affinity for these metal atoms and non-ambient conditions are required to remove water molecules bound to metal-centres and free the sites up for interaction with toxic gases and other contaminants. To modify a MOF's structure to be resistant to these conditions risks altering the properties and effectiveness of the material at adsorption. Instead, the strategy of placing a barrier between the water and the MOF allows the MOF to act as intended and rely on the barrier material to keep the water from filling the MOF pores.

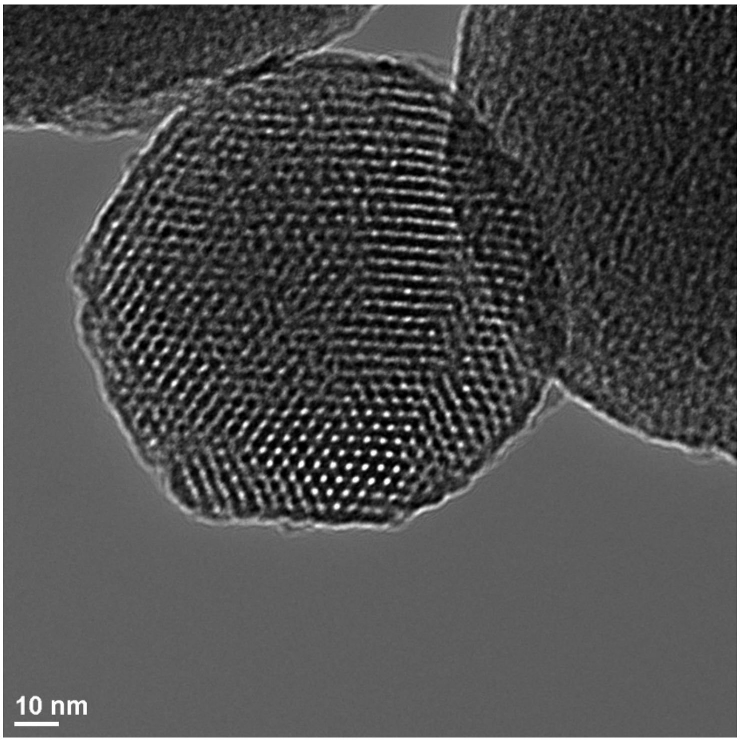

Figure 55: TEM Micrograph of a mesoporous silica particle. Public Domain Image.[1]

The first choice of material for this task is mesoporous silica. Mesoporous silicas are made by the use of a silicon source dispersed in a solution of a structure directing agent (SDA) which forms micelles in the solution. The silicon source then hydrolyses around the micelles, forming a solid. Addition of acid or base affects how the silica source is hydrolysed and changes the structure of the produced material. The resulting material is then calcined at high temperatures to remove the SDA and leave a porous structure with pores between 2-50 nm.

5.2. Synthesis and Characterisation of Mesoporous Silicas

Initial silica synthesis followed the procedure published by Seo et al.[2] The conditions used by Seo et al produce a solid with two different pore sizes of approximately 11 nm and 30 nm, which will be large enough to still allow impregnation of the silica with metal salt and ligand following the post-synthetic functionalisation of the silica. The silica is functionalised by the addition of 4-(triethoxysilyl)butronitrile during the initial condensation phase resulting in a silica featuring–RCN groups throughout the structure. These were oxidised to carboxylic acid groups by the addition of 48% sulfuric acid at elevated temperature, which also removes the templating co-block polymer, P123. Typically the polymer would be removed by calcination at 823K if the post-synthetic functionalisation was not being carried out. The resulting product of the reaction of the silica with sulfuric acid is designated mesostructured cellular foam-carboxylic acid (MCF-COOH). In an attempt to minimise the interference of surface silanol groups present on the surface of the silica from disrupting the formation of the MOF, where the metal ions are tethered to the silica by the –COOH functionality, the MCF-COOH was further reacted with methyltriethoxysilane (MES) in reflux. The additional methylation of the silanol groups acts to prevent them from competing with the ligand to bind to the metal ions when the crystallisation of the MOF is taking place. The resultant white powder is designated as carboxylic acid functionalised, Mesostructured Cellular Foam (Methylated)-COOH (MCF(M)-COOH).

To prepare the MCF(M)-COOH for the incorporation of the MOF, a solution of 0.2M of nickel acetate or magnesium nitrate in 4:1 w/w methanol:water was prepared, mixed with the powdered MCF(M)-COOH and then slowly evaporated until only dry solid remains. This material is then used in the preparation of the MOF in place of the metal salt.

The nitrogen adsorption isotherms of the mesoporous silica, as-synthesised (Figure 56), after removal of the template (Figure 57) and post-functionalisation (Figure 58) are shown below. A sample of the as-synthesised silica was calcined at 723K to obtain a surface area of the sample without the SDA affecting measurements. The measured surface area for MCF-CN is 653 m^2/g. It displays a distorted Type II isotherm.

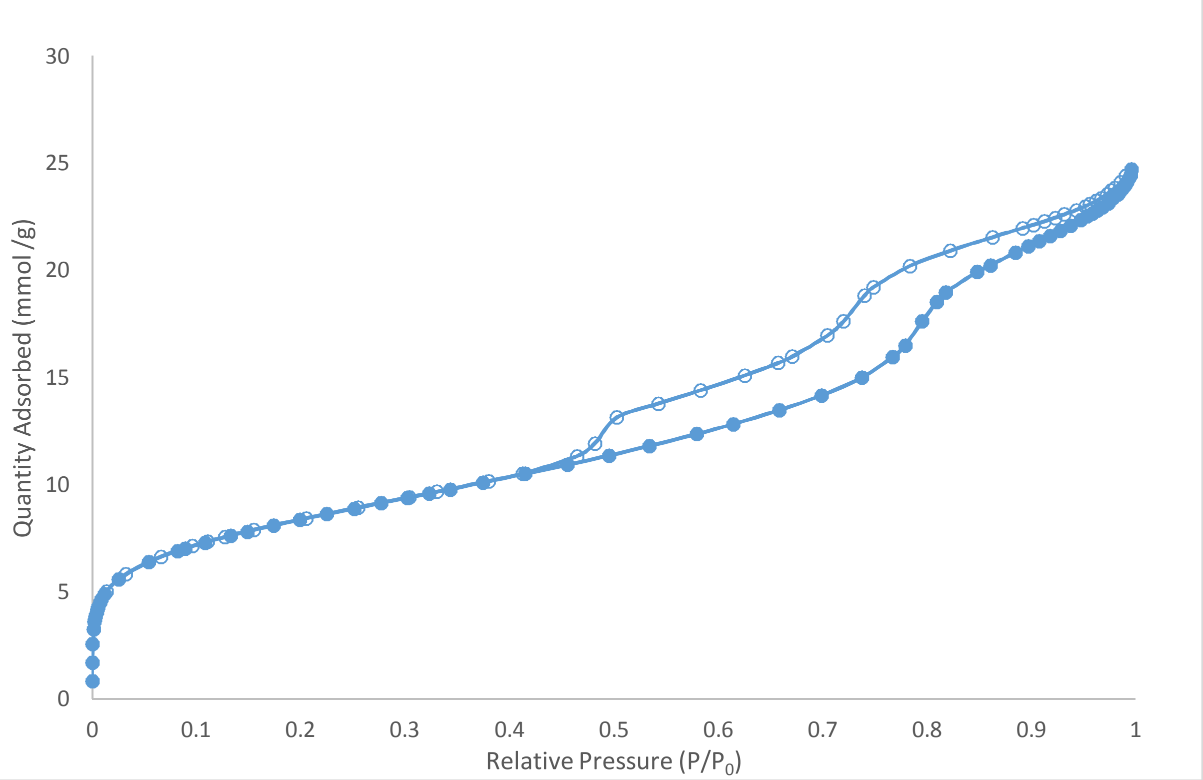

Figure 56: Nitrogen Adsorption Isotherm of MCF-CN. Solid points indicate adsorption, hollow points indicate desorption.

Once the as-synthesised silica was treated with sulfuric acid, another surface area measurement was taken (Figure 57). MCF-COOH shows a decrease in surface area to 480 m^2/g.

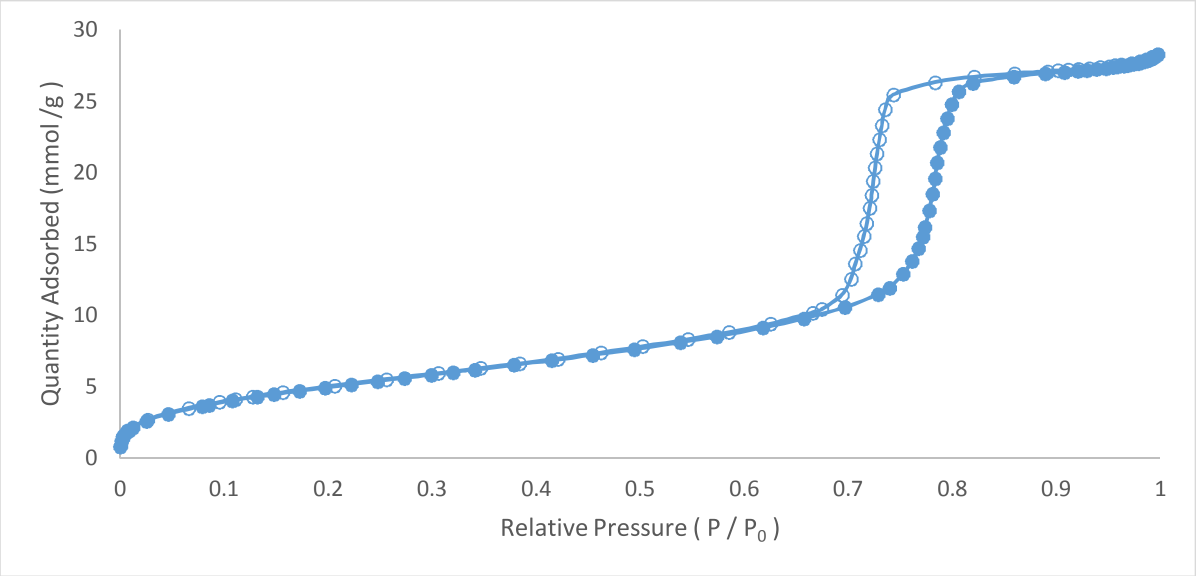

Figure 57: Isotherm of MCF-COOH after treatment with 48% H_2SO_4. Solid points indicate adsorption, hollow points indicate desorption.

There is a slight decrease in available surface area in the silica when it is methylated but a high degree of porosity remains (Figure 58). The MC(M)-COOH has a measured surface area of 387 m^2/g.

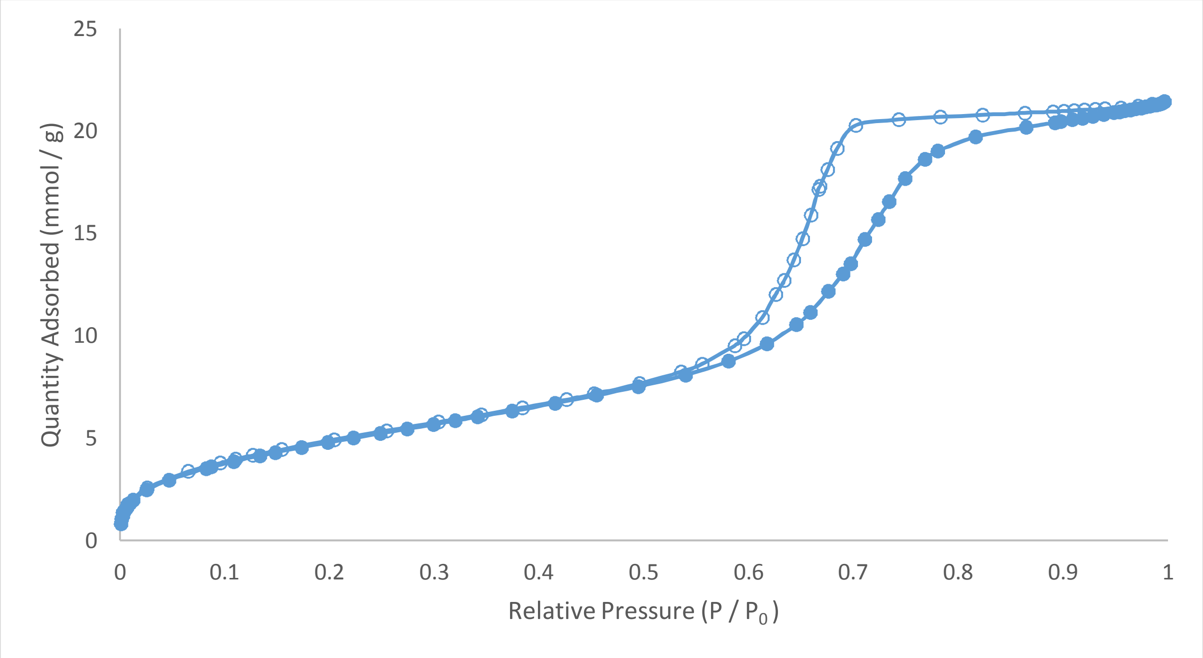

Figure 58: Nitrogen Adsorption of Methylated Silica (MCF(M)-COOH). Solid points indicate adsorption, hollow points indicate desorption.

5.3. Synthesis of CPO-27 Series and Nano-hybrid Materials.

CPO-27-M is a three dimensional MOF that is comprised of metal atoms that have an octahedral coordination environment consisting of six oxygen atoms, five atoms being deprotonated oxygen atoms from the dhtp^{4-} ligand and the remaining site is occupied by a solvent molecule. The pores of the 3D structure are hexagonal and are approximately 11Å in diameter (determined by analysis of the crystal structure) with the coordinated solvent molecules projecting into the pores. Upon activation by heating in vaccuo, the solvent molecules are released, leaving co-ordinatively unsaturated metal-centres to which other molecules may bind.

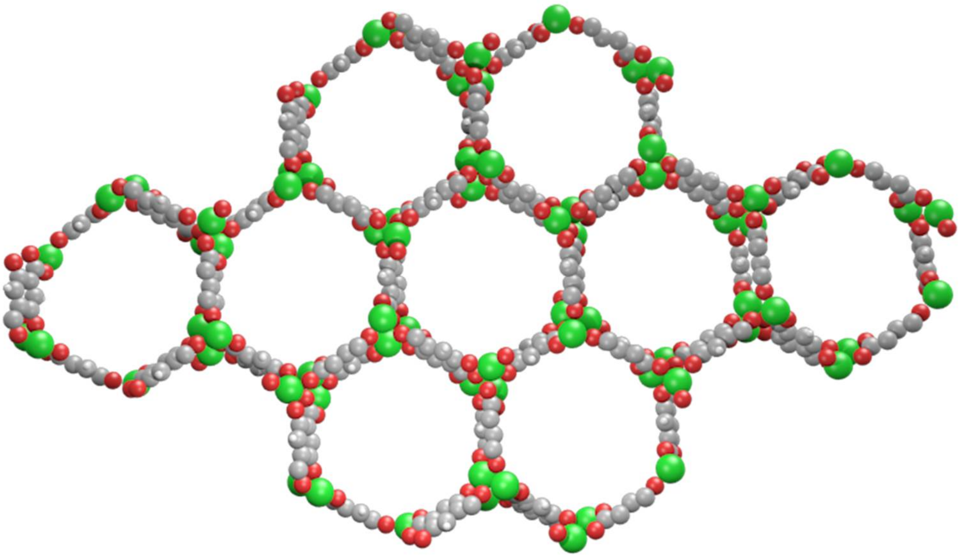

Figure 59: The structure of CPO-27. The honeycomb structure extends in three dimensions. The individual channels are one dimensional and molecules cannot pass between them. Metal atoms (green) oxygen (red) and carbon (grey) are shown. Hydrogen atoms omitted for clarity.

The CPO-27 series (also known as MOF-74) is an isostructural series of MOFs constructed from 2,5-dihydroxyterephthalic acid (2,5-H_4dhtp), with a variety of different metal cations. This makes for a highly versatile MOF, which can be tailored to suit the task required of it. The known structures of the CPO-27 series include nickel,[3] cobalt,[4] magnesium,[5] zinc,[6] and copper[7] iso-structural variants, all of which are stable in air and are capable of being desolvated to produce co-ordinatively unsaturated metal sites. Iron and manganese variants have also been reported, however they are not stable in air and as such, are unsuitable for this project.[8,9] For the purposes of this thesis, these will be referred to as CPO-27-M, (where M signifies the metal in the structure), all of which are analogous to their MOF-74-M descriptions in some references and literature.

For this project, the nickel and magnesium CPO-27 variants were investigated for their ability to remove ammonia from a gas stream for the purposes of air purification. These materials were supplemented by the addition of mesoporous silica foam, which acts as a support for the material, enhancing its mechanical stability and providing a surface upon which any post-synthetic functionalisation can be made to tailor the hydrophobicity and gas separation properties of the silica-MOF hybrid.

CPO-27-Ni can be prepared by a variety of methods,[10,5,11] but for the silica-MOF hybrids, a mixture of nickel acetate and 2,5-H_4dhtp were dispersed in a 50:50 mixture of tetrahydrofuran and water, producing a yellow-brown powder. The predicted pattern from a published CIF file and powder diffraction of the obtained compound is shown below (Figure 60).

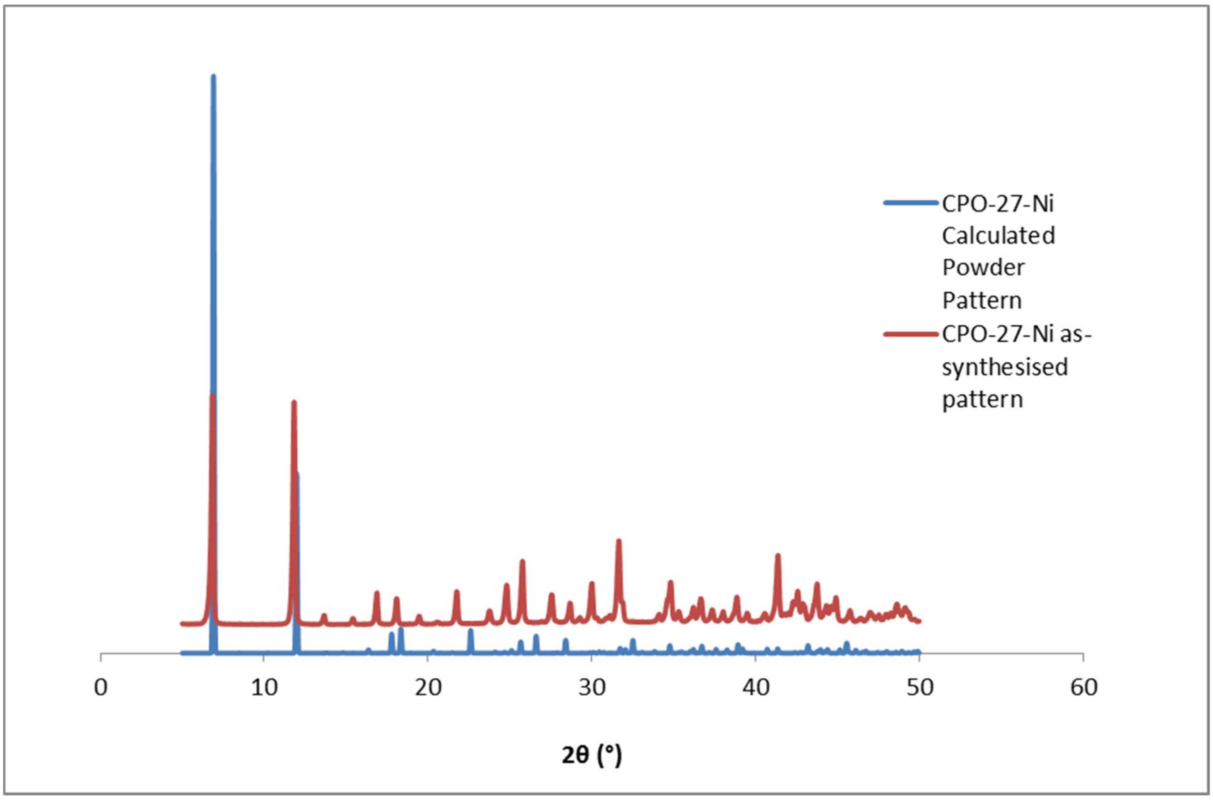

Figure 60: Predicted PXRD pattern of CPO-27-Ni compared with the as-synthesised.

The resultant powder pattern shows it to be a phase-pure CPO-27. The crystallites produced are too small for single crystal X-ray diffraction studies, however, the powder pattern shown is a direct match for other CPO-27 structured materials, such as CPO-27-Co, which do have reported single crystal structures.

To produce the MOF-impregnated silica, a variation of the synthetic procedures was used in which the Ni-loaded silica replaced the nickel salt (nickel acetate). A suspension of the Ni-loaded silica in a solution of 2,5-H_4dhtp was heated either in an autoclave in a conventional oven or by microwave irradiation. The resulting hybrid solid was collected for further analysis.

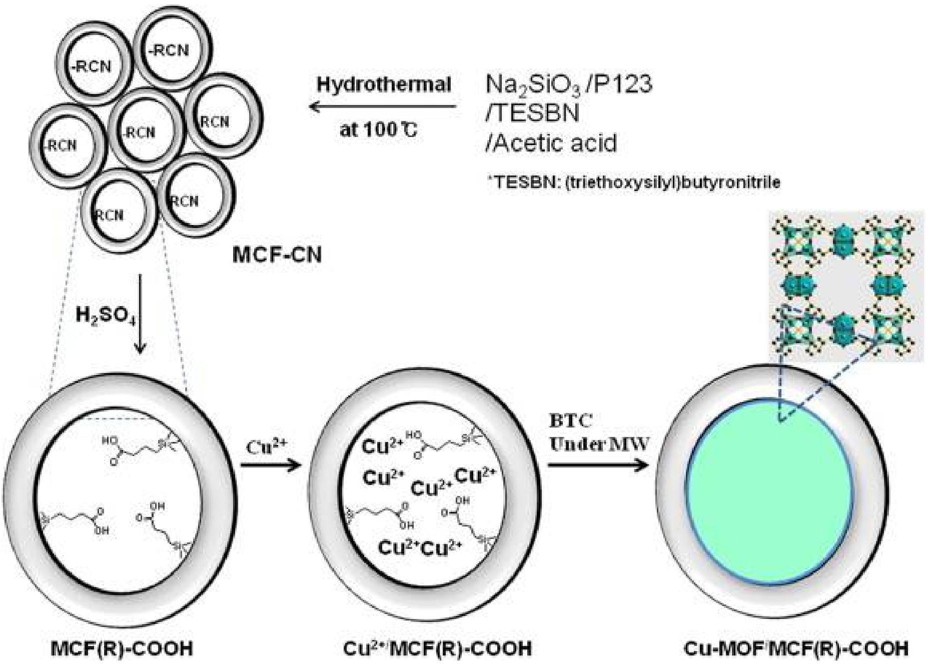

Figure 61: Schematic Diagram of reaction process involved in making MOF-Silica nano-hybrids, in this instance HKUST-1.[2]

Samples of CPO-27-Ni-impregnated silica prepared by microwave-heating for times of less than 1 hour only displayed the amorphous signal of the silica in the reaction mixture, suggesting formation of the MOF did not occur and no crystalline MOF had been deposited. It is likely that the interference of the silica and short reaction time limited formation of the MOF in those samples. Reaction times were increased to promote synthesis of the MOF.

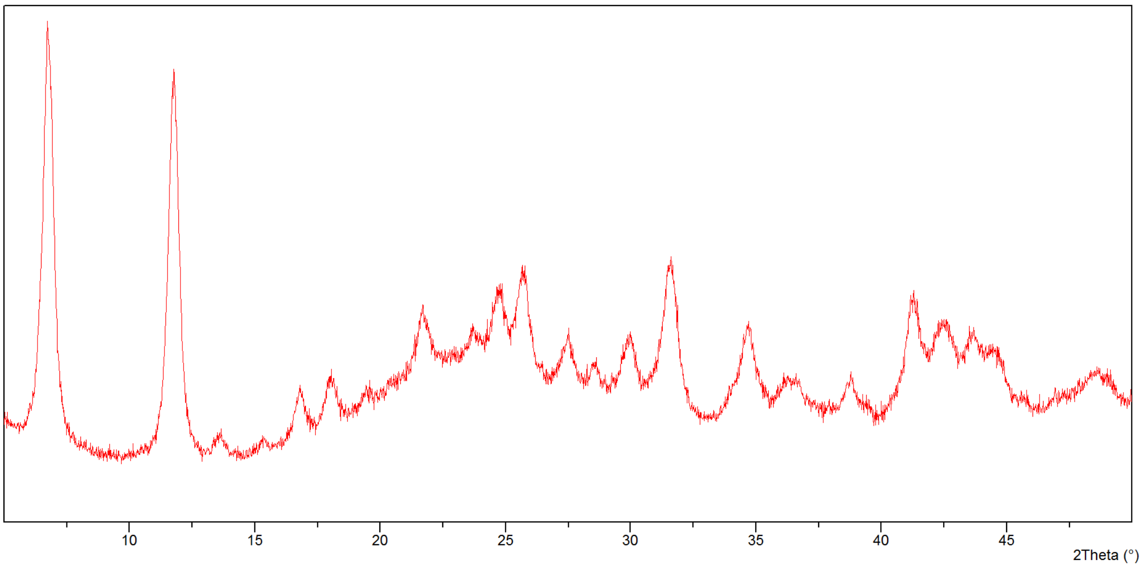

Figure 62: PXRD of CPO-27-Ni Hybrid. The signal for the MOF is super-imposed on the broad signal of the amorphous silica.

Hybrid materials synthesised in the microwave for four hours produce a PXRD pattern (Figure 62) in which peaks corresponding to the presence of CPO-27 could be identified, which shows MOF's XRD pattern super-imposed on the amorphous signal of the silica.

To attempt to ascertain if the MOF within the silica shell was still suitable for the adsorption of gas molecules, CO_2 adsorption was used instead of the standard nitrogen adsorption as the conditions observed at 77K would not be representative of those occurring at "room-temperature". Due to the nature of having two porous materials which could both potentially have impaired porosity as a result of the process, the use of CO_2 as a probe molecule will only detect the metal sites of the MOF, as the silica itself has no sites which will allow the gas to adhere. Literature reports[12] suggest that CPO-27-Ni adsorbs between 5-6 mmol of CO_2 per gram at standard temperature and pressure (STP), corresponding to 1 molecule of CO_2 being adsorbed for every nickel centre present in the material. The materials produced here adsorb 2 mmol/g after activation at 150°C for 12 hours.

Based on gas sorption measurements, the percentage MOF present the hybrid material is around 35-40%.[12] Adsorption testing on the hydrophobic silica has shown that it adsorbs negligible quantities of CO_2 and as a result it does not factor into these calculations.

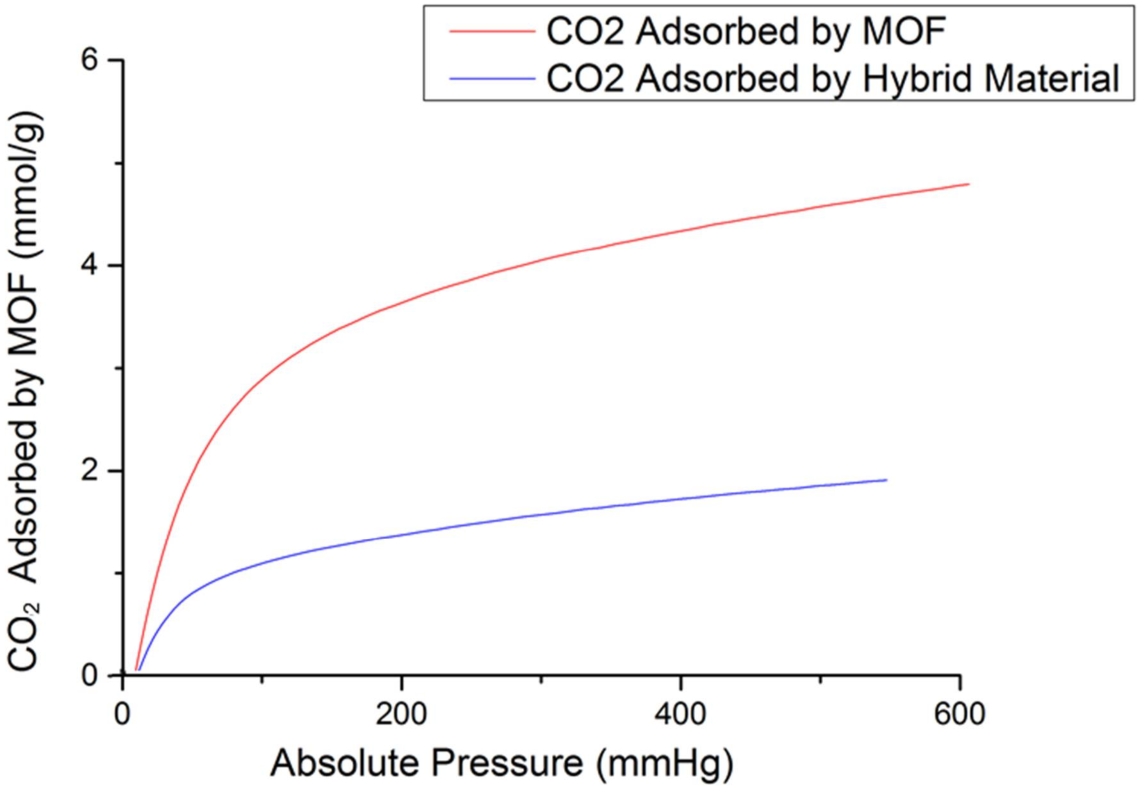

Figure 63: Graph of effective CO2 adsorption in CPO-27-Ni vs the hybrid material CPO-27-Ni-impregnated silica.

When the additional mass of silica is taken into account, these results suggest that there is little to no effect on the adsorptive capability of the MOF when hybridised in this manner. With this reported capacity, CPO-27-Ni is comparable to an existing industrially produced adsorbent, Zeolite 13X. Zeolite 13X is a common component in respirator cartridges which has a reported maximum loaded weight of 4.7 mmol/g of CO_2, suggesting that CPO-27-Ni is at least on a par with other available CO_2 adsorbents.[13] At the time of synthesising these materials, access to a method of determining the quantity of MOF present was unavailable.

To compare the behaviour of the hybrid materials to that of the MOF, TGA was undertaken with samples being heated at 10 K/min to 973K to determine solvent release and decomposition of material. The results are shown in Figure 64

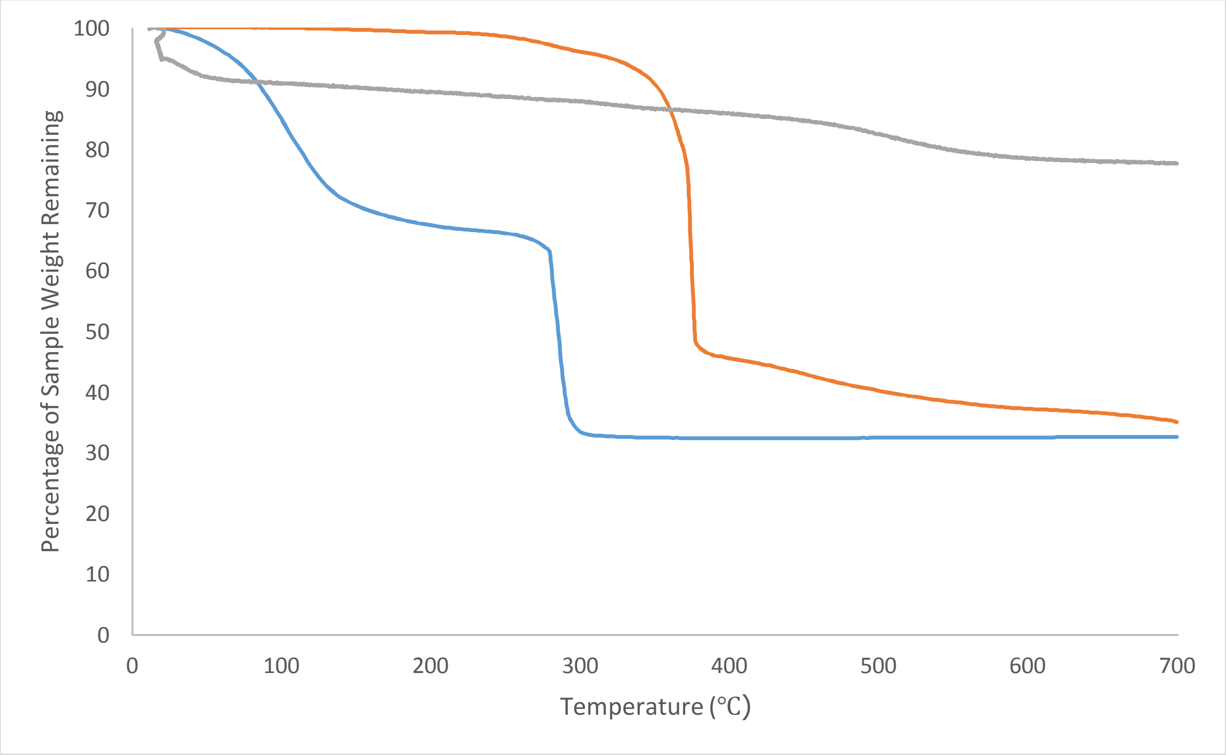

Figure 64: TGA Trace of CPO-27-Ni (blue), the CPO-27-Ni silica hybrid (red) and the mesoporous silica (green) heated to 700°C.

The as-synthesised solid shows a gradual loss of solvent weight up to 200°C and then structural integrity is lost after 300°C when heated in air. This data is in agreement with other published works on CPO-27-Ni.[4,12] In contrast, the silica-MOF hybrid material exhibits a vastly different trace pattern when it is exposed to high temperatures. The TGA trace of the unloaded silica is provided for comparison purposes.

When compared to the trace of CPO-27-Ni, very little weight loss occurs over the course of the heating to nearly 400°C before a rapid loss of weight indicates that decomposition has occurred. There is also a prolonged decrease in mass after the initial collapse of the MOF structure as the organic molecules are oxidised. This suggests that a large increase in the thermal stability of the MOF has been obtained as a result of hybridisation with the mesoporous silica. An increase in the temperature range over which the MOF is stable may allow for the material to be regenerated after physisorption of gases to the metal centres. Further research was deemed to be outwith the scope of this study, due in part to the disposable nature of gas mask cartridges.

5.4. CPO-27-Mg and Silica Hybrids

Variations of the aforementioned synthetic procedure were used to prepare CPO-27-Mg. The general process is the same, with the combination of the magnesium source with the ligand in a Teflon-lined steel autoclave in various solvent mixtures with reaction times of 24-72 hours. The protocol from the previous synthesis of CPO-27-Ni was used as a starting point for microwave syntheses.

Table 7: Synthesis Conditions of CPO-27-Mg [10,11]

Magnesium Source	Solvent Mixture	Ligand Molecule	Temperature of Reaction	Additional Reagents	Reaction Time In oven
$Mg(NO_3).6H_2O$	$DMF/EtOH/H_2O$ in ratio 15:1:1 mL	2,5-H_4dhtp	110°C	1M NaOH	24 hours
$Mg(NO_3).6H_2O$	$THF/H_2O/NaOH$ in ratio 7:3:2 mL	2,5-H_4dhtp	110°C	1M NaOH	24 hours
$Mg(NO_3).6H_2O$	$THF/H_2O/NaOH$ in ratio 7:3:2 mL	2,5-H_4dhtp	110°C	1M NaOH	72 hours

A few attempts were made to produce CPO-27-Mg under microwave irradiation where reactions times of up to eight hours were used and each attempt produced only a clear yellow solution. This solution was removed by rotary evaporation, giving a fine yellow powder, which was shown by PXRD to be an amorphous solid and non-porous to nitrogen adsorption.

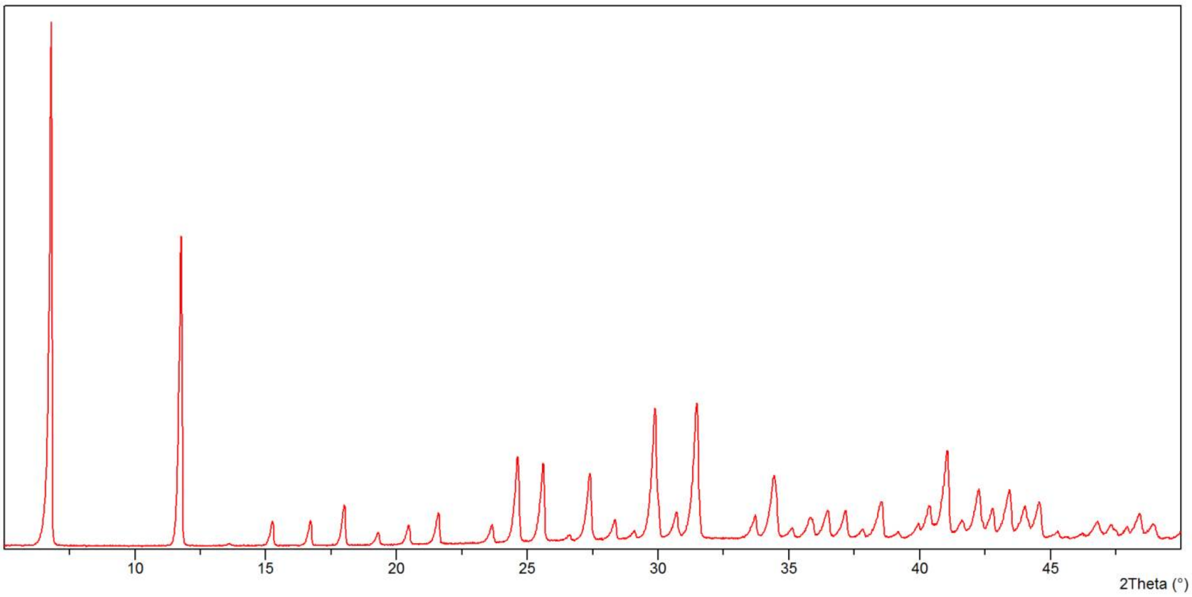

Figure 65: Powder Pattern of CPO-27-Mg MOF produced by solvothermal synthesis.

Samples produced under solvothermal conditions have shown a powder pattern (Figure 65) which matches those published in literature[14] and produce larger crystallites than the CPO-27-Ni syntheses mentioned before. TGA analysis shows a more protracted release of solvent for CPO-27-Mg than CPO-27-Ni and a higher decomposition temperature is observed (Figure 66).

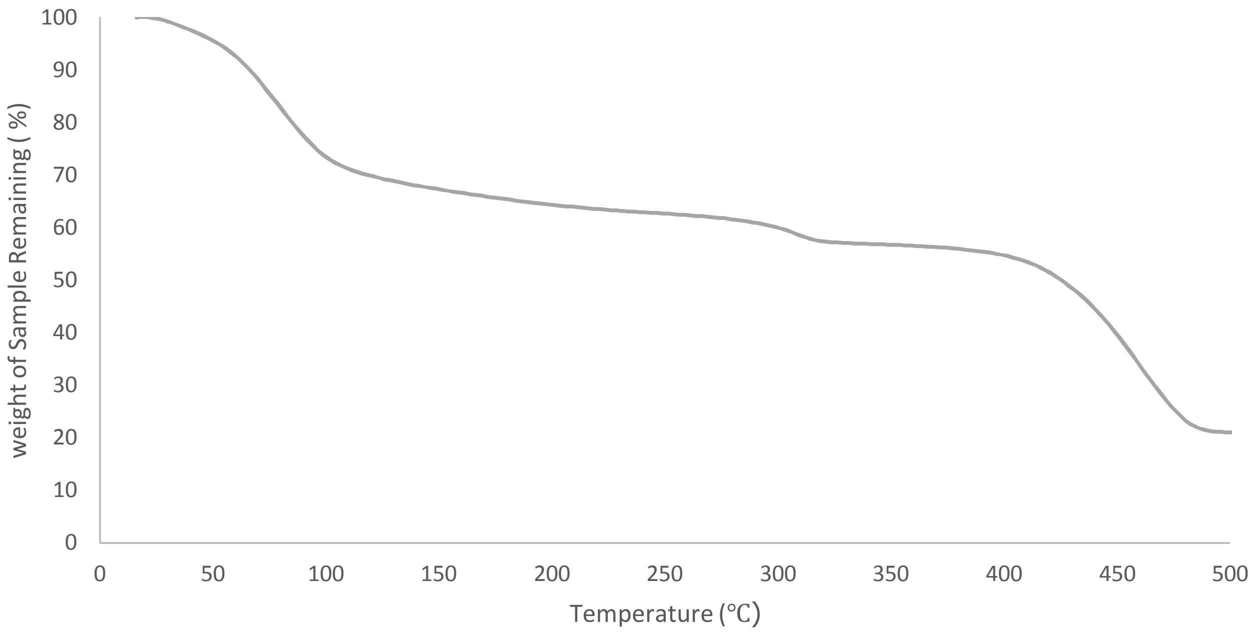

Figure 66: TGA of CPO-27-Mg (solvothermal synthesis).

The structure also shows excellent gas adsorption properties for both carbon dioxide and nitrogen. The material takes up 6 mmol/g of CO_2 at approximately 1 bar of CO_2, representing a 26wt% uptake within the structure.[15] This value increases further as pressure is increased to over 36 atmospheres where there have been reported capacities of 68% being attainable at 278 K with no apparent effect on the structure of CPO-27.[15] The high level of stability and capacity shown make CPO-27-Mg an ideal candidate for the potential rigors to be faced during toxic gas adsorption. Adsorptions conducted on the materials produced using the DMF based synthesis (Table 7) require a lengthy solvent exchange process where the material is stirred under methanol for up to 7 days, with fresh methanol added to the material every twenty-four hours. In contrast to this, the materials produced using THF/EtOH/H_2O solvent mixtures have produced inconsistent yields and inconsistent levels of porosity. An alternate synthesis was proposed by Dr. Paul Wheatley, which has since been patented,[16,17] which makes a sodium salt of 2,5-H_4dhtp to enhance its solubility and allow for synthesis outside of an autoclave.

5.5. Synthesis of Na_xH_{4-x}dhtp

One of the considerations that must be made for any compound being used in this project is that it will require an industrial-scale synthesis if it is to be viable for use in a respirator cartridge. The small-scale methods detailed in previous sections rely on solvothermal synthesis in autoclaves, which are difficult to scale to industrial quantities without significant investigation of how to optimise the synthesis. The solvothermal syntheses also made extensive use of DMF and THF, which have environmental concerns attached to their use.

By contrast, water and ethanol are plentiful, inexpensive and in the case of ethanol, produced on an industrial scale globally and far less damaging to the environment. As part of an effort to produce CPO-27-Mg on a large scale for experiments and for later industrial scale production, sodium salt of the 2,5-H_4dhtp ligand was used to increase the solubility and allow the reaction to take place more easily in a reflux environment, a common industrial scale process. With increased water solubility of the sodium salt of the dihydroxyterephthalic acid over the acid itself, a transition to a solvent mixture composed of water and ethanol was possible.

To produce this sodium salt, 2,5-dhtp is reacted with a four equivalents of sodium hydroxide under refluxing ethanol. For short reaction times, this produces a mixed-phase green and yellow solid that is soluble to varying degrees in water. By increasing the reaction time from one hour to sixteen hours, this produces a fluffy pale yellow solid that shows a highly hygroscopic nature and immediate solubility in water. While elemental analysis and mass-spectrometry of samples of the have been inconclusive as to the exact protonation state of the dhtp unit, it is suspected that the materials that appear over the course of the reaction correspond to different levels of protonation of the dhtp unit. This Na_xH_{4-x}dhtp salt is then heated to reflux with $Mg(NO_3)_2$ in aqueous ethanol to produce CPO-27-Mg. The details of this synthesis were published by D. Cattaneo et al.[17]

The PXRD of CPO-27-Mg produced by this reflux method is shown below with a comparison to CPO-27-Mg that was synthesised using literature procedures (Figure 67).

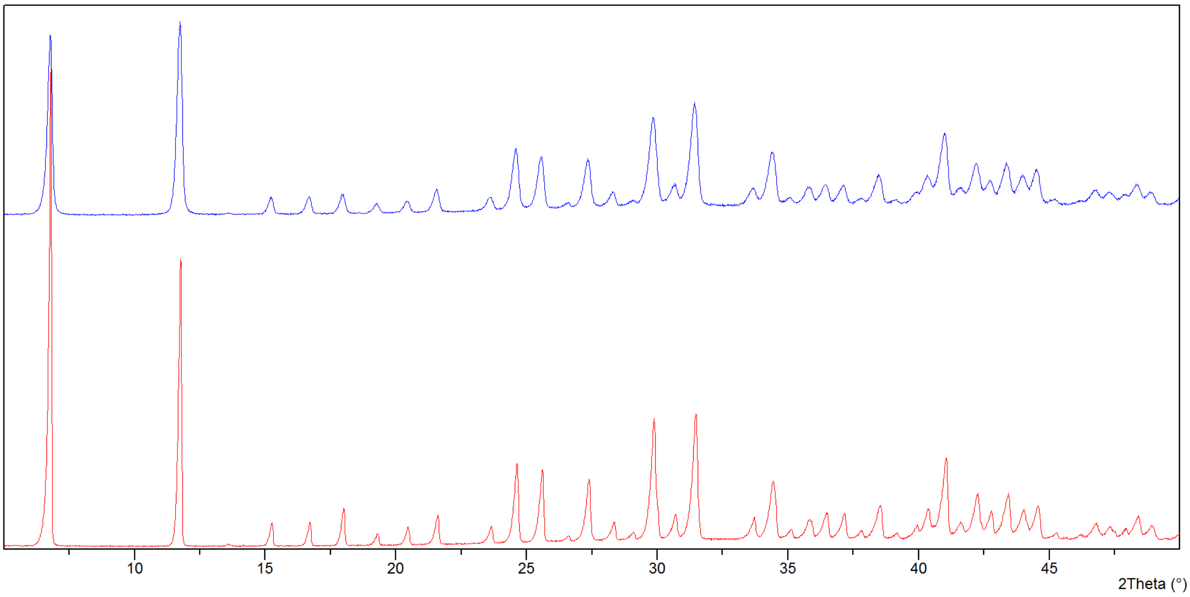

Figure 67: Comparison of CPO-27-Mg made by solvothermal synthesis (blue) and reflux-based synthesis using Na_xH_{4-x}dhtp (red).

The powder patterns of materials produced by different methods are a good match for each other although viewing of the samples by microscope examination shows that the crystallites are far smaller when produced by the reflux method. The materials were also examined by carbon dioxide gas sorption and reported an excellent uptake of CO_2 of around 6 mmol/g, which is consistent with published reports of CO_2 adsorption by CPO-27-Mg.[18] This capacity was obtained without any prior solvent exchange of the as-synthesised MOF. The samples that were tested for CO_2 required only the normal desolvation of being heated at 250°C for 12 hours in vacuo, compared to the three to seven day solvent exchange procedure required to produce comparable adsorption in the material produced using DMF.

5.6. Synthesis of Hybrids involving CPO-27-Mg

As previously mentioned in Section 6.2, the method for the production of mesoporous silica infused with metal-organic frameworks was by suspending solid silica in a methanolic solution of an appropriate metal salt and allowing the solution to evaporate, leaving mesoporous silica with magnesium nitrate distributed through the structure. This $Mg(NO_3)_2$ infused silica was then used to replace the metal salt addition to the synthesis of the MOF. The infused silica was used in quantities where one gram of material was representative of 2 mmol of magnesium nitrate and refluxed with Na_xH_{4-x}dhtp in water and ethanol for 4 hours. A pale yellow powder was recovered from the solution by filtration and dried before undergoing PXRD analysis. The resulting spectrum is shown below with a comparison.

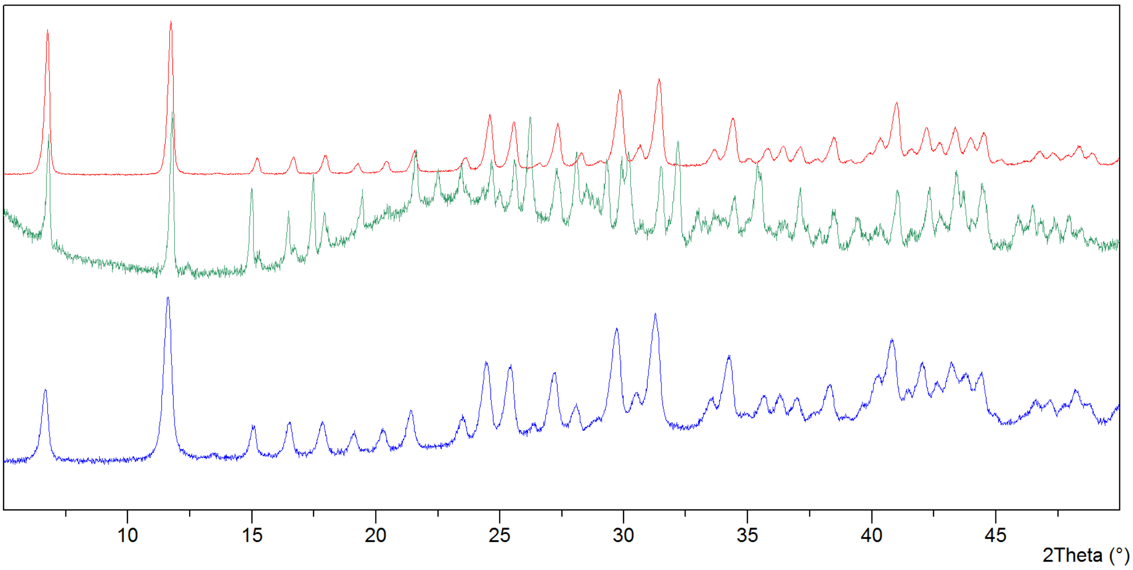

Figure 68: Comparison PXRD of CPO-27-Mg synthesised by two different methods and the hybrid material. CPO-27-Mg made by microwave synthesis (blue), CPO-27-Mg by sodium linker method (red) and the hybrid material (green).

Figure 68 shows a comparison of powder diffraction patterns from different synthetic methods of producing CPO-27-Mg. The hybrid powder pattern shows a distortion caused by the amorphous silica present in the sample, as well as some slight changes to the pattern. The hybrid material, however, shows a capacity for gas sorption that is only present when the MOF structure is intact. The samples of CPO-27-Mg hybrid showed a capacity of between 2 and 3 mmol CO_2/g, which indicates that the material would typically contain 40 to 50%wt of activated MOF, suitable for the removal of toxic gases. These calculations were based on gas sorption measurements compared to the previously synthesised pure MOF, which shows a typical capacity of between 5-6 mmol of CO_2 per gram of solid material at around 1 atmosphere of pressure.[15,18]

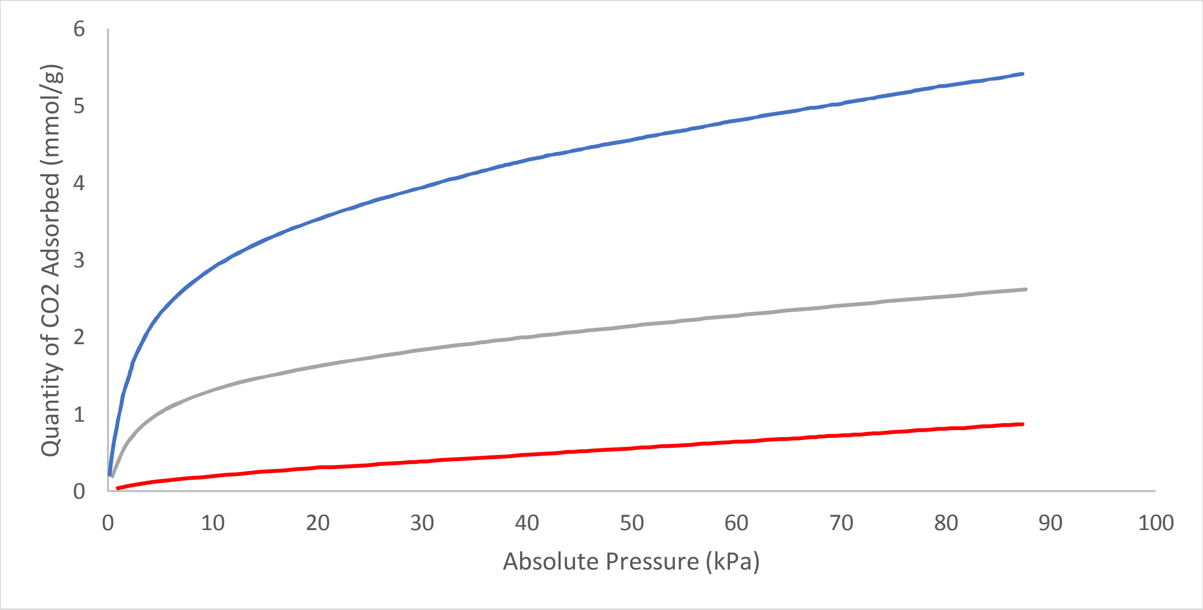

Figure 69: CO2 Adsorption Isotherms of CPO-27-Mg produced by the Na linker method (blue), early CPO-27-Mg hybrids (red) and the CPO-27-Mg hybrids made using the Na ligand synthesis (green).

The capacity of the material is reduced compared to the pure MOF, which is unsurprising given the content of non-adsorbing silica. Gas sorption measurements initially were disappointing with calculations suggesting that approximately 16% of the weight of hybrid material was composed of structurally intact MOF. Repetition and an increase of the reaction time from a four hour synthesis to a sixteen hour synthesis produced material that adsorbed significantly more CO_2. Obtaining an accurate measurement of the quantity of MOF present in the material was desired but ICP-MS was unavailable at the time this research was conducted and by the time it was available as an analytical option, the direction of the research had changed, rendering it moot.

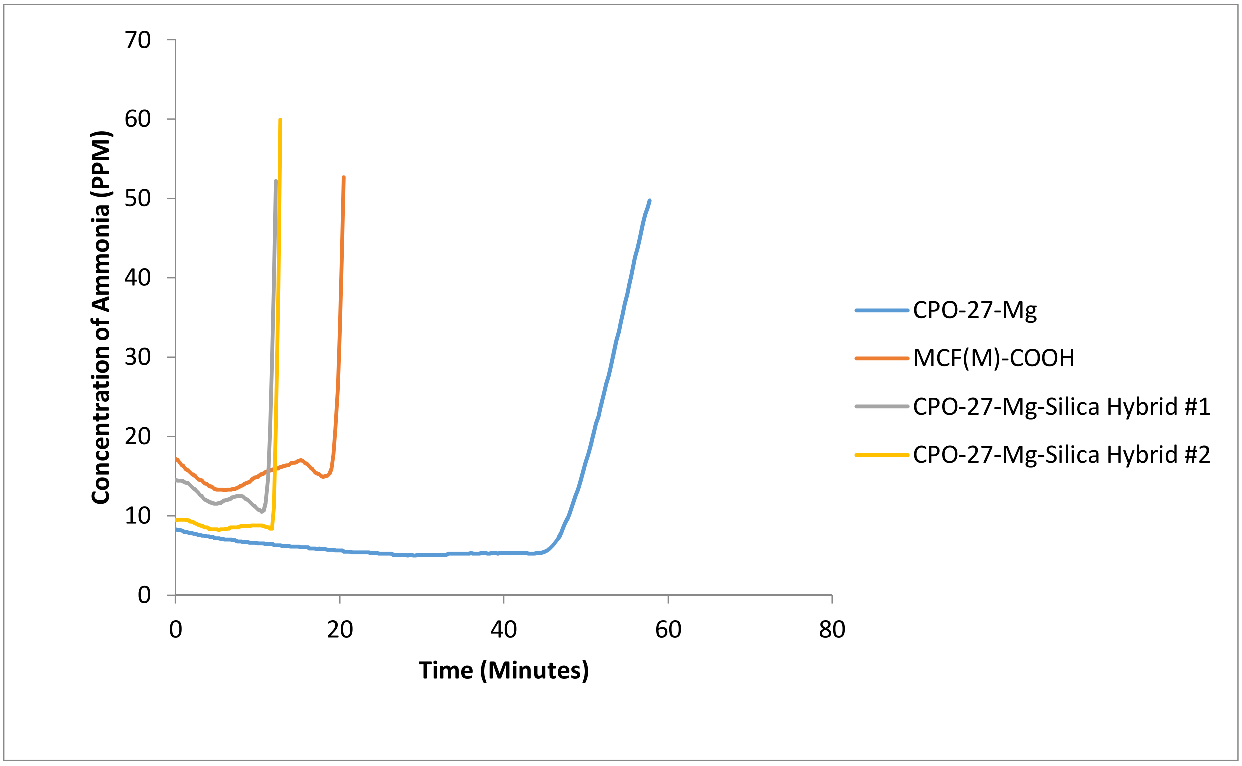

Figure 70: Ammonia Breakthrough Times of CPO-27-Mg, Mesoporous silica and Hybrids of the two materials. The above zero start and decrease before breakthrough is a result of uneven packing of the sample plug.

The hybrid sample was compared to the silica and the as-synthesised MOF by ammonia breakthrough in dry conditions (Figure 70). The CPO-27-Mg samples showed typical breakthrough times of 40 minutes. The hybrid material displayed breakthrough times in the region of 10-20 minutes. In comparison, a sample of the silica used in the hybridisation reaction offered a base time of 18 minutes. Breakthrough times for samples tested under humid conditions showed almost immediate breakthrough.

A modified silica (MCF-M-COOH) was produced using the same method, impregnated with the magnesium salt as before then reacted with the $Na_xH_{4-x.}$dhtp ligand to produce a hybrid material. The material was then post-synthetically modified with 20% of the samples weight in dichlorodimethylsilane to potentially improve hydrophobicity.

Given that CPO-27-Mg silica hybrid materials exhibit poor performance in humid conditions, attempts were made change the process of hybridisation from one that involved incorporating the MOF inside an existing silica, to a process that would involve the deposition of the silica shell onto the MOF crystallites. This is investigated in the following chapter.

5.7. Conclusions

The attempted formation of a hybrid material from MOFs and mesoporous silica did not diminish the water uptake of the MOFs used in the hybrid material. The hybrid materials showed an increase in thermal-stability and retained their capacity for adsorption of gas, with capacities relative to the amount of MOF material present in the samples. It is possible to form both CPO-27-Ni and CPO-27-Mg within the pores of the mesoporous silica, which can be confirmed by powder XRD. Future work may relate to deeper investigation of the functionalisation of the silica to improve the hydrophobic properties of the materials.

5.8. References

1 Image courtesy of V. Lin of Iowa State University. Public Domain Image, *TEM micrograph of mesoporous silica nanoparticle*, 2015.

2 Y.-K. Seo, J. W. Yoon, U.-H. Lee, Y. K. Hwang, C.-H. Jun and J.-S. Chang, *Microporous Mesoporous Mater.*, 2012, **155**, 75–81.

3 P. D. C. Dietzel, B. Panella, M. Hirscher, R. Blom and H. Fjellvåg, *Chem. Commun.*, 2006, 959–961.

4 P. D. C. Dietzel, Y. Morita, R. Blom and H. Fjellvåg, *Angew. Chem. Int. Ed.*, 2005, **44**, 6354–6358.

5 P. D. C. Dietzel, P. A. Georgiev, J. Eckert, R. Blom, T. Strassle and T. Unruh, *Chem Commun*, 2010, **46**.

6 A. R. Millward and O. M. Yaghi, *J. Am. Chem. Soc.*, 2005, **127**, 17998–17999.

7 R. Sanz, F. Martínez, G. Orcajo, L. Wojtas and D. Briones, *Dalton Trans.*, 2013, **42**, 2392–2398.

8 S. Bhattacharjee, J.-S. Choi, S.-T. Yang, S. B. Choi, J. Kim and W.-S. Ahn, *J. Nanosci. Nanotechnol.*, 2010, **10**, 135–141.

9 W. Zhou, H. Wu and T. Yildirim, *J. Am. Chem. Soc.*, 2008, **130**, 15268–15269.

10 T. Grant Glover, G. W. Peterson, B. J. Schindler, D. Britt and O. Yaghi, *Chem. Eng. Sci.*, 2011, **66**, 163–170.

11 A. C. McKinlay, University of St Andrews, 2010.

12 A. Das, P. D. Southon, M. Zhao, C. J. Kepert, A. T. Harris and D. M. D’Alessandro, *Dalton Trans.*, 2012, **41**, 11739–11744.

13 R. S. Franchi, P. J. E. Harlick and A. Sayari, *Ind. Eng. Chem. Res.*, 2005, **44**, 8007–8013.

14 D.-A. Yang, H.-Y. Cho, J. Kim, S.-T. Yang and W.-S. Ahn, *Energy Environ. Sci.*, 2012, **5**, 6465–6473.

15 P. D. C. Dietzel, V. Besikiotis and R. Blom, *J. Mater. Chem.*, 2009, **19**, 7362–7370.

16 WO2013186542 A1, 2013.

17 D. Cattaneo, S. J. Warrender, M. J. Duncan, R. Castledine, N. Parkinson, I. Haley and R. E. Morris, *Dalton Trans*, 2016.

18 X. Wu, Z. Bao, B. Yuan, J. Wang, Y. Sun, H. Luo and S. Deng, *Microporous Mesoporous Mater.*, 2013, **180**, 114–122.

Chapter 6 “Armoured” MOFs – A Protection Strategy

6.1. Background

MOFs have enjoyed a period of exponential growth over the last two decades with a large number of publications each year that have been the focus of a wide range of research topics.[1] The main difficulty encountered using MOFs in real-world applications is that compared to other porous solids such as zeolites, most MOFs are relatively fragile and the supramolecular structure can be disrupted by heat or humidity. Previous methods to attempt to help MOFs overcome these limitations, the concept of the core-shell MOF[2–4] was investigated as a method to exploit the properties different ligands can give MOFs. First, a MOF with the desirable properties is synthesised and then used as a crystal-seed to grow a second MOF on the surface of the existing material. By exploitation of this, it allows for the synthesis of materials that exhibit properties of both MOFs. While this can be advantageous in designing MOFs to suit a specific purpose, the combination still lacks the thermal stability of zeolites.

Due to the microporous nature, the combination of MOFs and zeolites would only be a mixture rather than a hierarchical solid which are made by having a microporous material within a mesoporous material. Hierarchical solids have been made using zeolites and mesoporous silicas and in this chapter, explore a published synthesis which puts a microporous MOF within a mesoporous silica shell.[5,6] However, mesoporous silicas share many of the structural stabilities of zeolites and can have their pores sizes controlled by choosing appropriate synthesis conditions.

In this section, the process of creating a hierarchical material is explored with the hopes of producing a MOF that is resistant to moisture and has enhanced the longevity in adverse conditions.

In early 2014, Li and Zeng[6] reported a process by which they applied a shell of silica around particles of MOF in order to greatly increase their mechanical strength and thermal stability. This simple combination of MOFs and silica results in an impressive increase in the temperature range over which the MOF is stable. A schematic representation of the process is shown below (Figure 71). The armoured materials were characterised by several methods including PXRD, gas sorption techniques, electron microscopy and ammonia breakthrough testing.

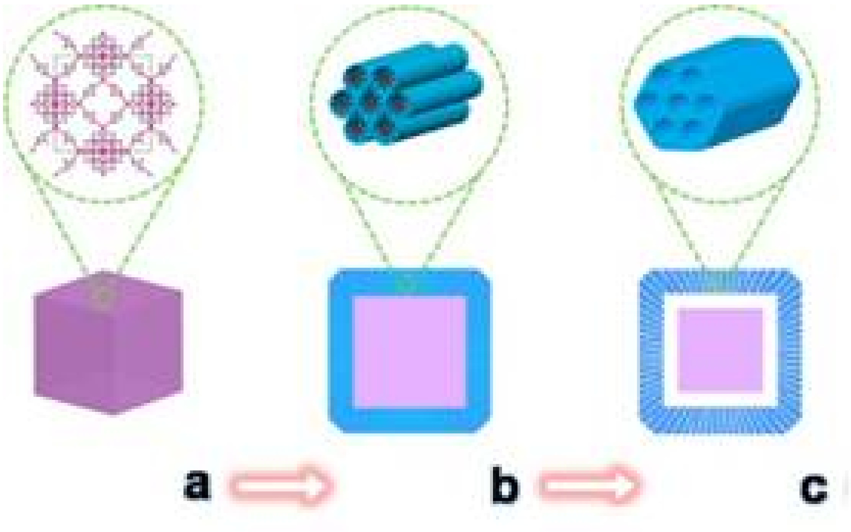

Figure 71: Diagram of "Armouring" Process applied to MOFS.[6] Step *a* is the coating of the material in polymer, Step *b* is the addition of the CTACl template and deposition of the silica layer, Step *c* is the calcination to remove the template. Adapted from work by Li and Zheng.[6]

The synthetic process to apply the layer of mesoporous silica around the MOF was done by the use of polyvinylpyrrolidone (PVP), which was dispersed into methanol and stirred with the MOF, in order to provide a layer around the MOF particles upon which the silica may be deposited (Figure 71.a). A typical base mediated production of mesoporous silica was then used that is similar to industrial standard procedures and relies on a simple templating process using cetyltrimethylammonium (CTA) chloride, which occupies the pores in the silica-gel (Figure 71.b) and is then later removed by heating under vacuum(Figure 71.c).from this synthesis.

MOFs that are capable of withstanding the template removal step are uncommon, as the CTA based templates typically decompose at temperatures >240°C. This is evidenced by the resulting XRD patterns in the previously mentioned publication that show that HKUST-1, while capable of being successfully armoured, does not survive the template removal process which results in a large quantity of copper oxide rather than the intact MOF structure.[6] CPO-27-Mg displays an improved thermal stability over the nickel and zinc variants and is able to withstand temperatures of 250°C without loss of structure when heated in vacuo or inert atmosphere. In addition to the ammonia work undertaken on STAM-1 that was discussed in earlier chapters, this material was also the subject of armouring attempts to affect the water uptake and long-term stability of the material, which presented several interesting challenges in the armouring process that were not encountered by the authors of the previous studies.

6.2. Armoured CPO-27-Mg

The armouring process for CPO-27-Mg closely followed that reported in the literature. The production of MOF from the previously mentioned Na_xH_{4-x}dhtp synthetic method allowed for the scale of the reaction to be increased. As the work of Li and Zheng did not provide details of the quantities of MOF yielded by their synthesis or accurate masses of MOF used in the armouring process, there was no indication as to what mass of MOF powder could be effectively armoured using the published procedure. To combat this, HKUST-1 was synthesised using the method reported and the yield from this reaction was recorded and used as a starting point for the mass of MOF material, in this case CPO-27-Mg, needed for the armouring reaction. Following the published procedure from Li and Zheng, the procedure and reaction time for armouring HKUST-1 (as opposed to the conditions used to armour ZIF-8) was used as it was found that the alkaline (pH = 10) conditions used to armour ZIF-8 caused CPO-27-Mg to disintegrate. The pH of the suspension of CPO-27-Mg in aqueous TEOS was adjusted to pH 8.5 using sodium acetate. PXRD analysis of the resulting solid showed that the MOF remained intact throughout the synthesis. The armoured MOF was recovered from the reaction mixture and dried overnight.[6]

The removal of the templating agent was achieved by heating under a flow of nitrogen gas in a tube furnace from room temperature to 250°C at a rate of 1.5°C/min. Once the sample had reached 250°C, it was held at that temperature for 7 hours before cooling at 1.5°C/min. Nitrogen flow was discontinued when the sample returned to room temperature.

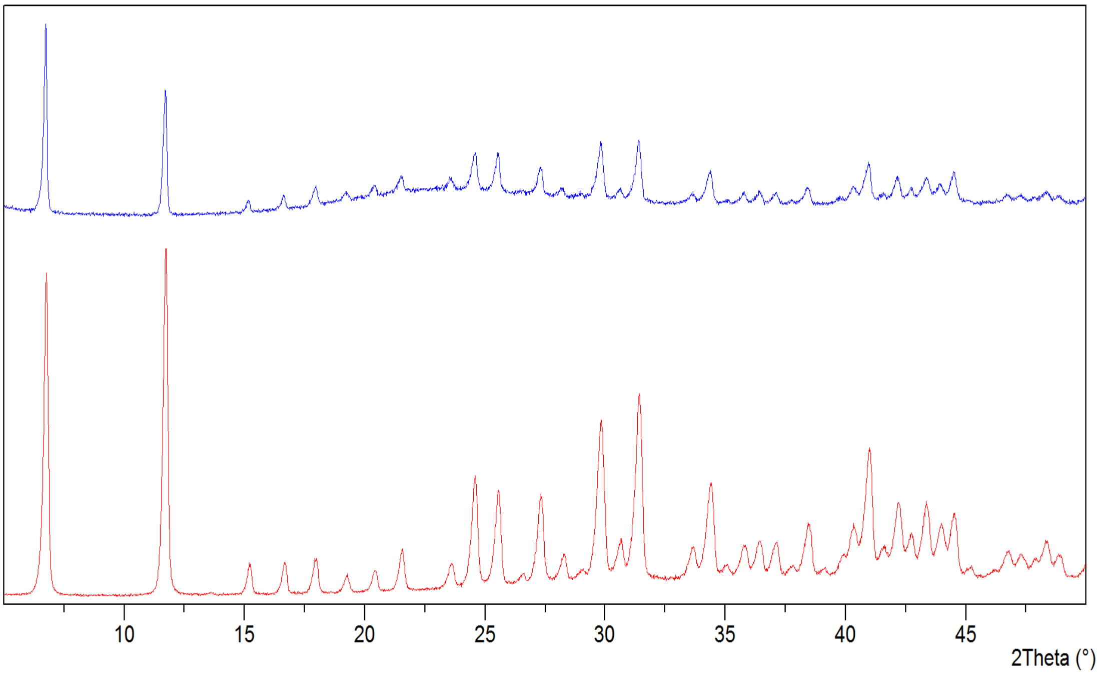

Figure 72: Comparison of CPO-27-Mg (red) with the armoured CPO-27-Mg (blue).

Aside from the higher baseline due to the presence of the amorphous silica signal in the material, the structure of CPO-27-Mg has remained intact throughout the entire armouring process.

In order to confirm that the encapsulation has occurred correctly, the samples were observed directly using electron microscopy. By coupling this with EDX analysis it is possible to determine the location of the silica and CPO-27-Mg within the powder sample and how they are arranged with respect to one another.

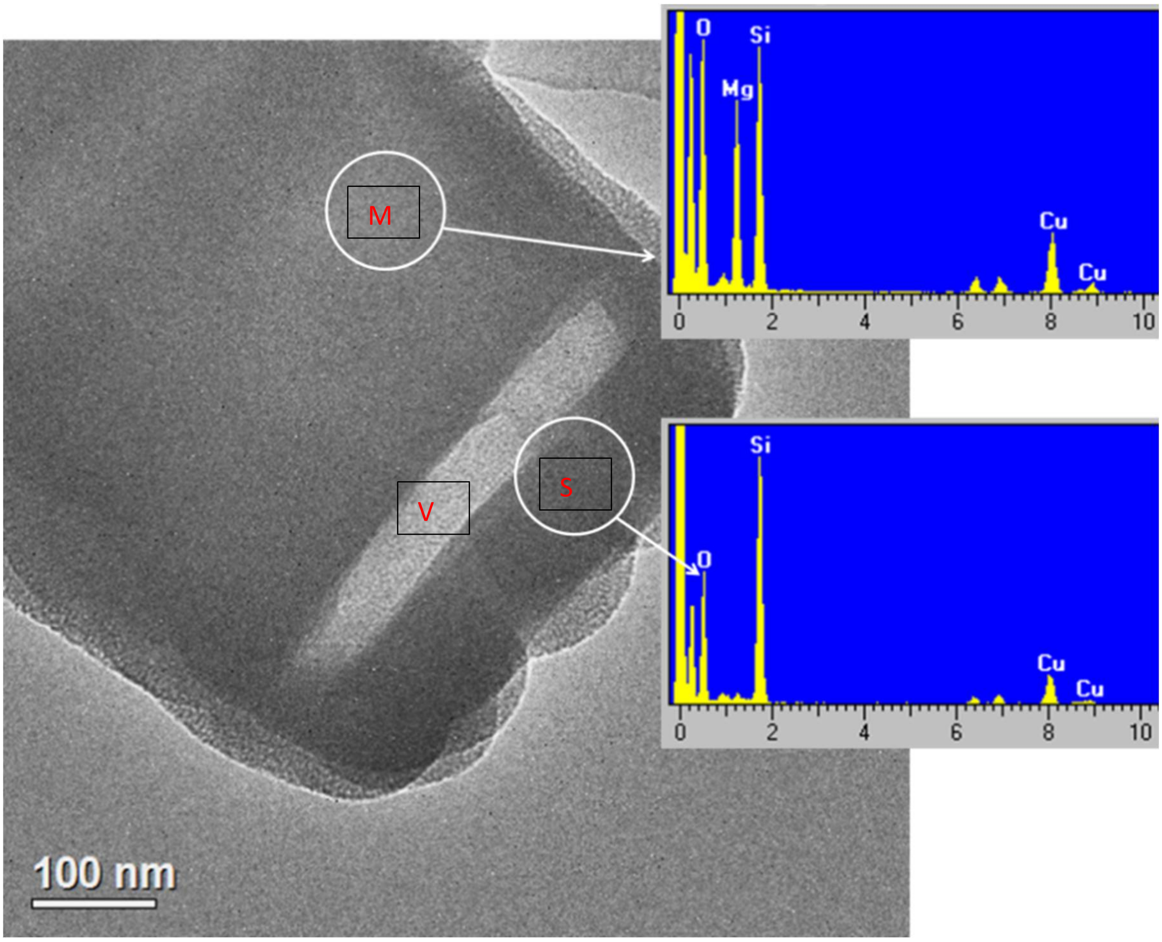

Figure 73: Scanning Transmission Electron Microscopy image of Armoured CPO-27-Mg with EDX graphs showing elemental composition of the material including MOF covered with silica (M), the outer silica shell (S) and the void previously occupied by the PVP (V).

As may be seen in Figure 73, the synthesis has resulted in small particles of MOF being encased in an envelope of silica with empty spaces between the MOF and silica caused by the removal of the PVP layer. The successful removal of the template indicates that the silica portion of the material is porous. In order to confirm the porosity carbon dioxide sorption studied were undertaken on the armoured

CPO-27-Mg in the same manner as those used on the silica hybrid in Chapter 6.The silica itself has no appreciable capacity for adsorption of carbon dioxide, indicating that any observed adsorption comes from the MOF material in the centre of the particles.

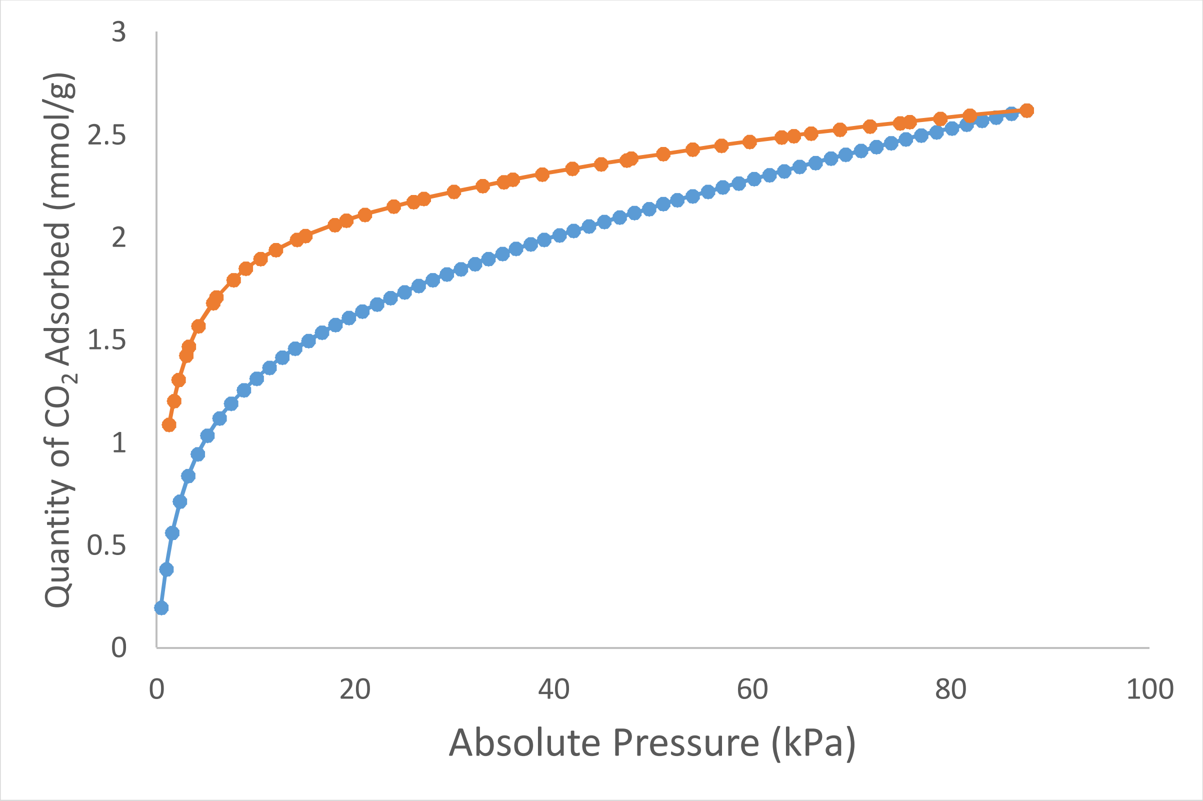

Figure 74: Carbon Dioxide Adsorption Isotherm on Armoured MOF CPO-27-Mg. Blue points indicate adsorption and red points indicate desorption of CO_2.

The material shows an adsorption of 2.5 mmol CO_2/g of solid, whereas the as-synthesised MOF is typically reported to have an adsorption of 5-6 mmol CO_2/g. This suggests that approximately half of the sample is composed of MOF and that the MOF structure remains intact and the material is capable of being evacuated of solvent molecules to allow for gas uptake. A BET measurement of the material indicates that the material has a total surface area of 220 m^2/g. This is significantly lower than the reported values for CPO-27-Mg, which has been reported as high as 1600 m^2/g.[7] It is currently not possible to accurately extrapolate the individual surface areas of the two components of the composite material as interactions between the surfaces of the two will result in unquantifiable changes in interactions with gas molecules. Regardless, the material exhibits suitable porosity for gas uptake studies.

In order to analyse the ratio of MOF to silica in the material, ICP-MS was used. The analysis would typically involve the pertinent sample being dissolved in strong acid and the concentration of the metal ions in solution determined by ICP. In the case of the hybrid and armoured materials, the silica does not dissolve, so corrections must be made to account for the sample not being 100% soluble in the solution. To correct for this, a difference method was applied where the initial sample was weighed, then dissolved using strong nitric acid and the silica residue removed by vacuum filtration, recovered, dried and weighed. The mass of dissolved hydrated MOF could then be calculated by the difference between the sample mass and the mass of the residual silica. The solution was analysed using ICP-MS to determine the quantity of the metal present, which could then be extrapolated to calculate the weight of dry MOF present. The difference between the mass of MOF dissolved and the mass of MOF calculated from the ICP measurements can be used to determine the amount of water occupying the pores within the MOF. An example calculation of the calculation applied to an ICP-MS result is shown in the Appendix.

The ICP-MS analysis indicates that the hybrid material only contains 3.9% of CPO-27-Mg by weight. This value is far lower than expected, based on the quantity of CO_2 adsorbed by armoured material, is not accurate. This suggests that the digestion of the CPO-27-Mg within the silica armour did not take place and only small portions of incomplete coverage or un-armoured MOF were dissolved. While this is problematic for obtaining an accurate measurement of the quantity of CPO-27-Mg in the armoured material, the ability of the material to be placed in concentrated nitric acid and retain a large quantity of the active MOF merits further investigation as to its stability in acidic conditions.

6.3. Ammonia Breakthrough on Armoured CPO-27-Mg

The materials were tested for their ammonia breakthrough capacity and compared to the existing MOF and the previous silica-MOF hybrid materials which had been further modified with methyl groups in order to increase the hydrophobicity of the samples.

Figure 75 shows the breakthrough times for selected samples of CPO-27-Mg and its hybridised variants. The hybrid materials were synthesised using Na_xH_{4-x}dhtp as the ligand source to prepare CPO-27-Mg under reflux conditions,[8] and compared to the materials produced by the THF-Water autoclave synthesis used to produce the samples using Chapter 6. The CPO-27-Mg produced by reflux, as opposed to under solvothermal conditions, shows an improved breakthrough time and higher overall capacity for ammonia adsorption in dry conditions, compared to the material produced from autoclave syntheses. The reflux synthesis of CPO-27-Mg supplanted the traditional solvothermal synthesis from this point onwards, due to its improved properties and ease of production at larger scales.

In comparison to the existing MOFs, the Na_xH_{4-x}dhtp ligand based MOF shown an improved capacity in dry conditions compared to the samples described in Chapter 6. The armoured material shows a longer breakthrough time compared to the hybrid material, with a breakthrough profile which is extremely similar. This suggests that the armoured material has a higher ratio of MOF to silica than the hybrid materials.

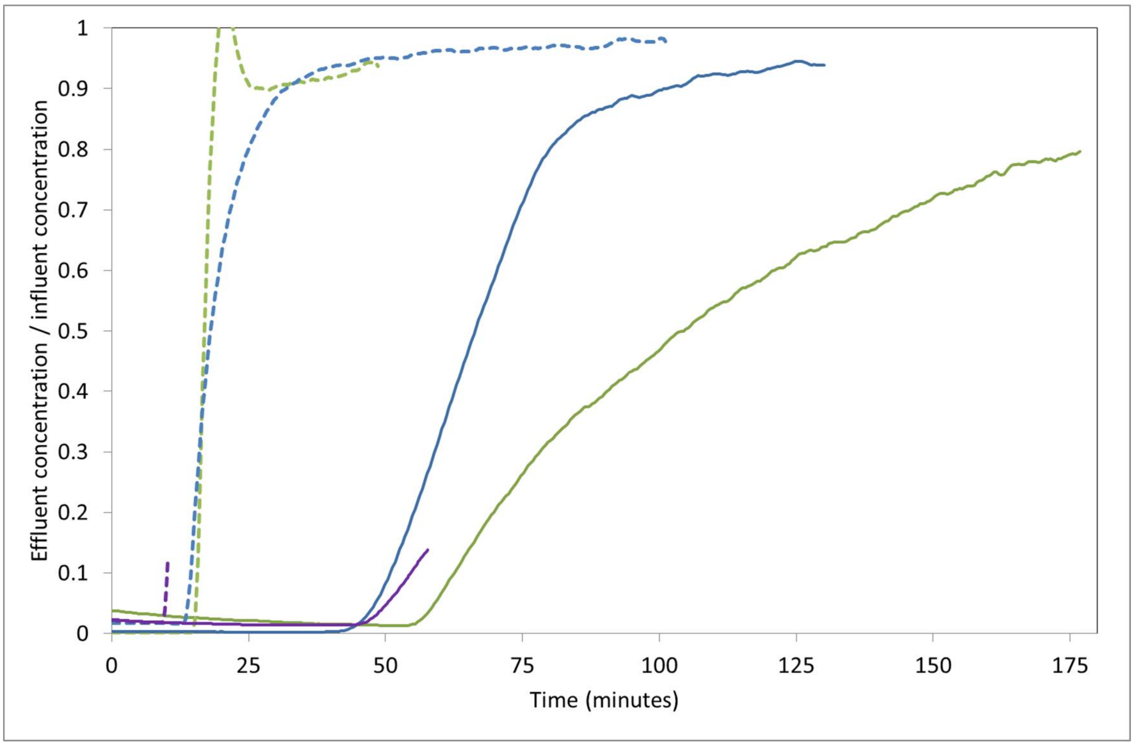

Figure 75: Ammonia Breakthrough Testing of Armoured CPO-27-Mg vs the unarmoured MOF. The Na Ligand CPO-27-Mg is shown in green, the Armoured CPO-27-Mg is shown in blue and the CPO-27-Mg produced by conventional autoclave synthesis is shown in purple for comparison. Dotted lines indicate tests run in 80% relative humidity.

The ammonia adsorption by the armoured materials in humid conditions does not show any significant improvements and are in line with the values obtained for the hybrid materials, showing an approximate breakthrough time of fifteen minutes in humid conditions. This suggests that the armoured material does not inhibit the water vapour uptake of the MOF.

6.4. Water Adsorption in Hybrid MOF Materials

To compare the armoured materials with the as-synthesised MOF, the samples were tested for water adsorption capacity.

The data for these adsorptions is shown in Figure 76. The armoured material shows a capacity for water corresponding to an equivalent untreated MOF. This suggests that the structure has survived the process of armouring, despite the stresses and rigors placed on the structure as a result of it. Further possible reasons for the inconsistency of gas sorption may possibly relate to unremoved template in the material, pore collapse as a result of the silica deposition process occurring directly on the surface of the MOF due to incomplete coverage by the template material, or unremoved solvent that due to increased heat tolerance was not removed when the material was dehydrated prior to analysis.

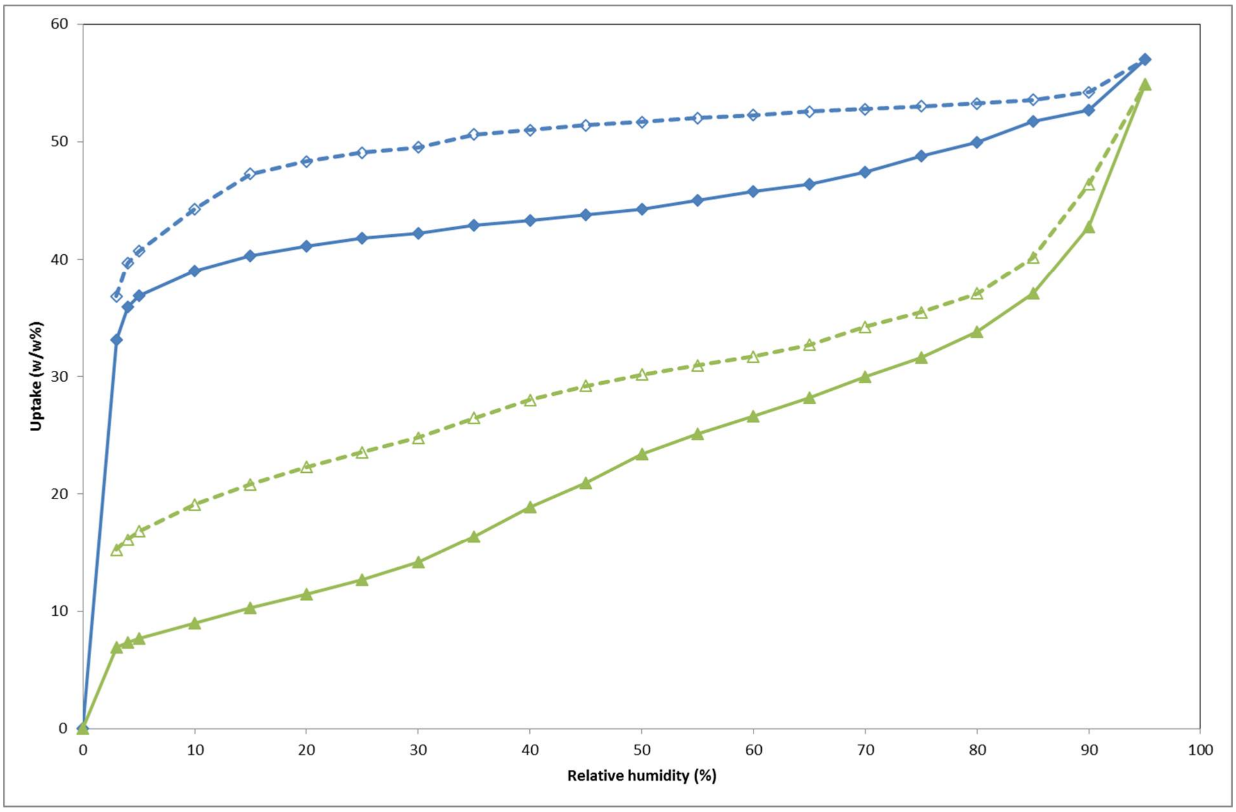

Figure 76: Water Uptake Isotherms of the various CPO-27-Mg from the Na ligand (blue) and the Armoured CPO-27-Mg (green).

Both the as-synthesised and armoured materials show a substantial water uptake. The kinetics of the uptake is altered, with a decrease in the rate of water uptake in the armoured material compared to the untreated MOF powder.

6.5. Armoured STAM-1

An investigation was conducted into armouring STAM-1, using the method published by Li and Zeng.[1] STAM-1, which (as shown in Chapter 5) has been shown by TGA to maintain its structure past the decomposition temperature of templating agent polyvinylpyrrolidone (PVP) and, along with its demonstrated water stability, was deemed to an ideal candidate on which to test the process.

Some minor modification of the method to synthesise the armoured material were made. The CPO-27-Mg based material is more resilient in elevated temperature, in air, STAM-1 typically decomposes at temperatures 100°C lower than CPO-27-Mg does and as a result, this method produced inconsistent results and required twenty-four hour monitoring to ensure gas flow did not drop off or allow the sample to burn. As a result, the armoured STAM-1 materials described herein have their template removed by heating the sample in vacuo using a Buchi furnace. By being able to slowly increase the temperature in vacuo, less charring occurred and the sample was successfully recovered. This also removes the HKUST-1 that is produced alongside STAM-1, as HKUST-1 suffers from similar stability problems at the calcination temperature.

After recovery of the hybrid material and the calcination process, the material was analysed by PXRD and CO_2 adsorption to confirm that that the MOF structure had survived the process and that the material was still porous and able to take up gas. The powder diffraction pattern of STAM-1 compared with a sample of Armoured STAM-1 (A-STAM-1) is shown in Figure 77. There is some loss of crystallinity but the general pattern of STAM-1 is retained. It should be noted that the peaks that indicate the presence of an HKUST-1 impurity (as mentioned in section 5.1) have been significantly diminished.

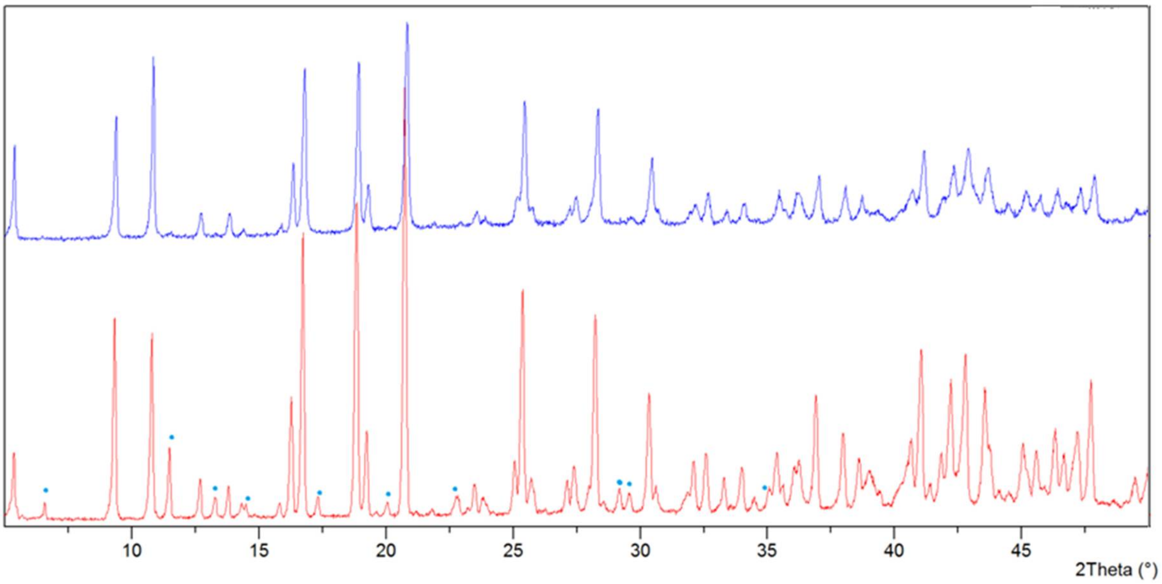

Figure 77: Comparison of STAM-1 (red) and Armoured-STAM-1 (dark blue) after calcination. Some loss of crystallinity is observed/apparent but the porous structure remains intact. Peaks marked with blue dots indicate HKUST-1 peaks that are diminished or removed in the calcined sample.

In order to test that the porous structure of STAM-1 was still accessible to gas, the material was tested using nitrogen adsorption at 77K and carbon dioxide adsorption at 298K. Samples were de-solvated at 150°C for 16 hours prior to gas sorption and were transferred under vacuum from degas port to analyser.

A typical nitrogen isotherm for STAM-1 is shown in Figure 78.

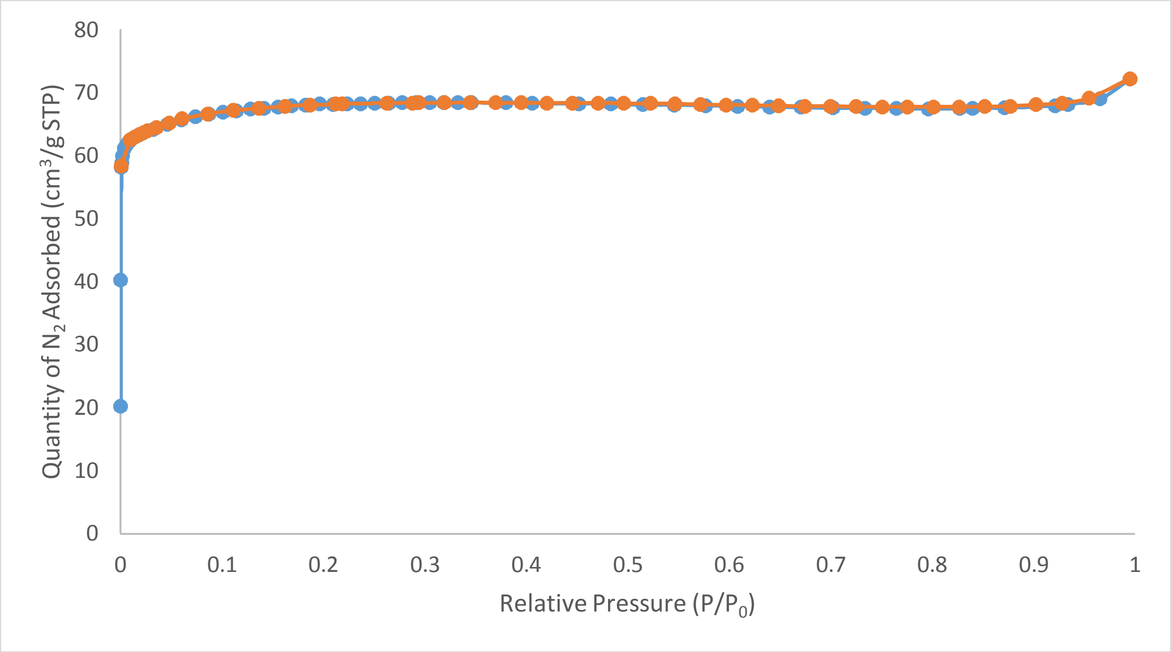

Figure 78: Nitrogen Adsorption Isotherm of a typical sample of STAM-1 displaying a classical Type 1 isotherm. Blue points indicate adsorption and red points indicate desorption.

When the armour is applied, the material shows a small decrease in observed surface area but the kinetics of the adsorption appear to be unaffected in the case of nitrogen (Figure 79). This initially suggested that STAM-1 was successfully encapsulated as demonstrated in the paper.

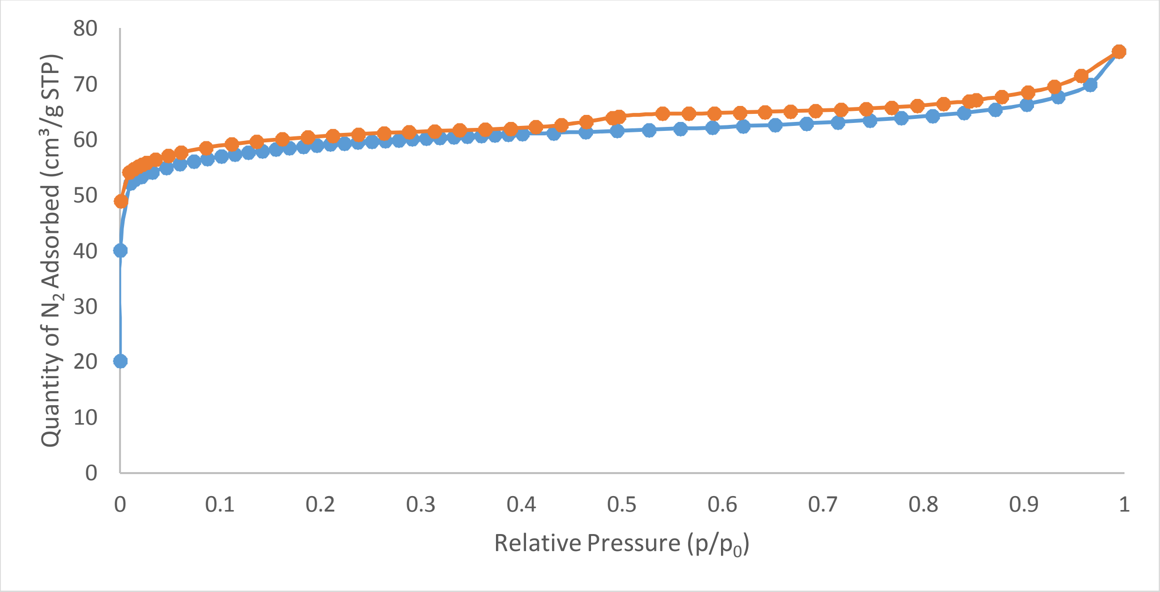

Figure 79: Nitrogen Adsorption on an armoured sample of STAM-1. Only minor variations in the isotherm are visible, suggesting the kinetics have been unaffected. Blue points indicate adsorption and red points indicate desorption.

The samples were analysed using TEM in order to determine if the particles of STAM-1 had been completely covered by the silica. The TEM and EDX show that, while the silica and MOF are both present in the material obtained (Figure 80), the coverage of the particles is incomplete. The presence of nickel in the sample is a result of the use of a nickel support, which was substituted for the traditional copper support to prevent masking of the copper content of STAM-1. It was found that the silica deposition interfered with the accuracy of elemental mapping, as a result analysis of the elemental content of samples of armoured MOF limited to EDX.

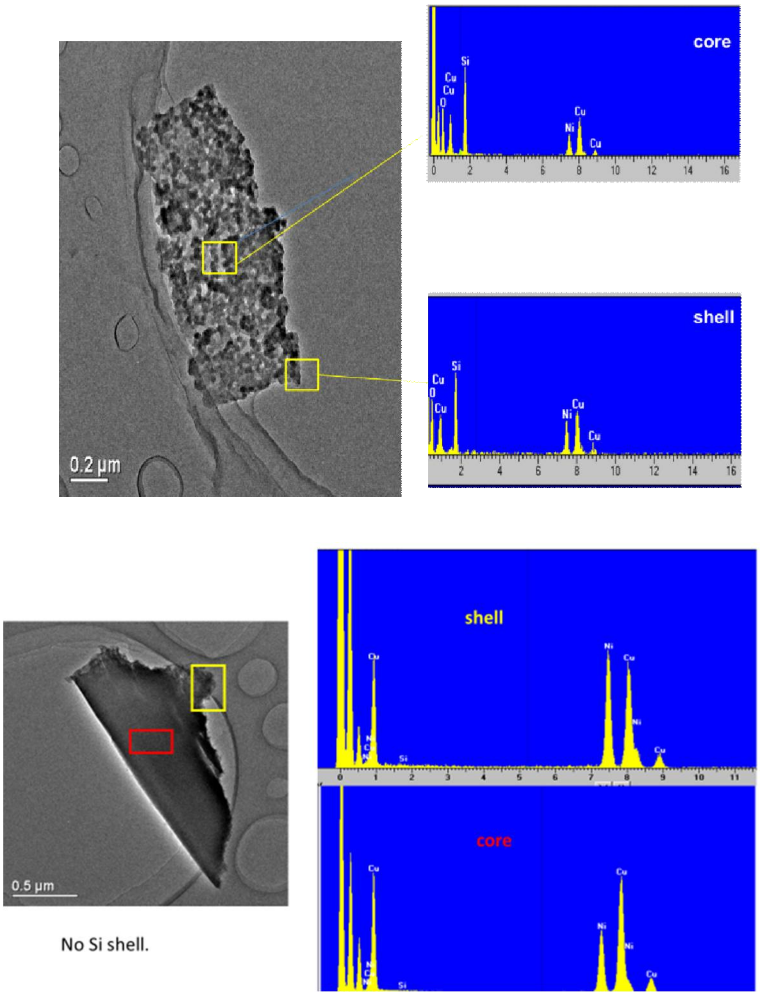

No Si shell.

Figure 80: TEM of STAM-1 particle with partial coating of mesoporous silica. In the background, large pieces of silica can be seen with no MOF embedded in them. Particles of STAM-1 have no silica coating and large pieces of silica can be seen in the background.

Compared to CPO-27-Mg and the samples reported by Li and Zheng, which formed discrete silica shells around the particles of MOF, there is highly inconsistent deposition of the silica. Further investigation of the reaction conditions indicated that when compared with the pH obtained by suspension of HKUST-1 in the silicate solution, which was approximately pH 8.5 when all reagents were added to the reaction, use of the same reaction conditions for armouring STAM-1 resulted in a pH of approximately 7.5. It is currently unclear as to why the change in MOF should produce such a drastic shift in pH, but it is possible that as the small quantities of HKUST-1 present in the mixture disintegrate, the btc^{3-} anions are released which will decrease the pH of the solution and affect the reaction. To remedy the inconsistency of the reaction mixtures, the pH of the later batches of the STAM-1 armour mixture were adjusted by the addition of 1M sodium hydroxide. The resulting TEM micrographs are shown below (Figure 81and Figure 82).

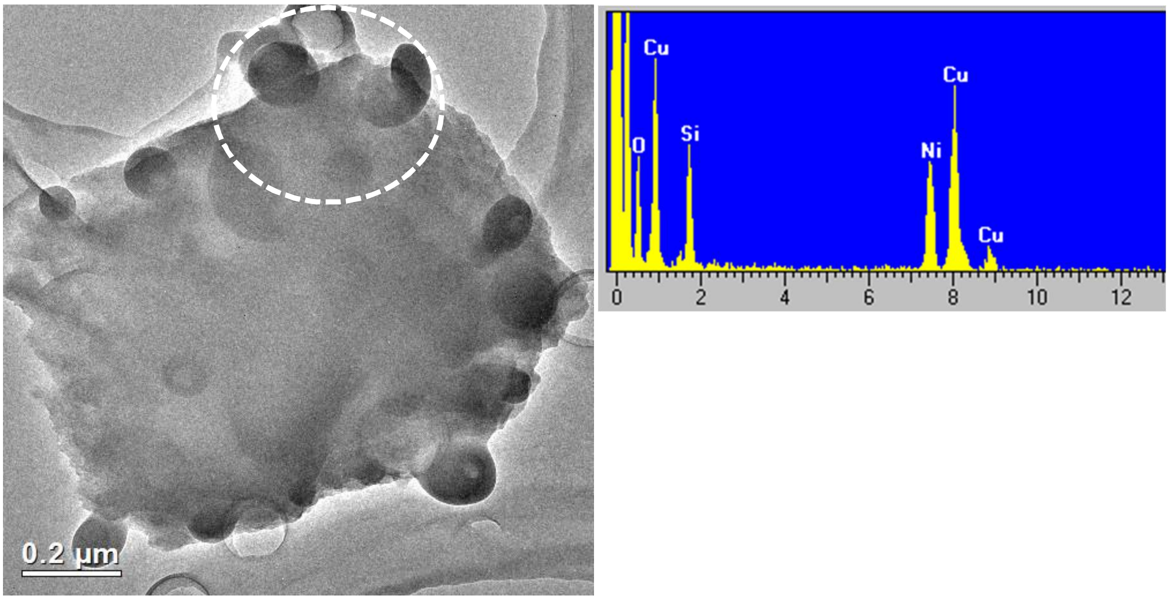

Figure 81: Resulting solid from the pH adjusted synthesis of Armoured STAM-1. The dotted circle indicates the material contains both Cu and Si, indicating the MOF has been encapsulated in the silica.

This also shows an inconsistency in the formation of the silica capsules, where small particles of the MOF are completely embedded in large chunks of silica (Figure 81) and larger particles have incomplete or no coverage (Figure 82). This suggested that, rather than the conditions of the reaction being at fault; the large particle size distribution of STAM-1 was affecting the process due to and the mixed material creating nucleation sites that result in improper deposition of the silica. TEM results from the armoured MOFs paper show that the particles of MOF used are relatively uniform in size and shape, whereas there appears to be a large variance in the particle size within STAM-1 samples.

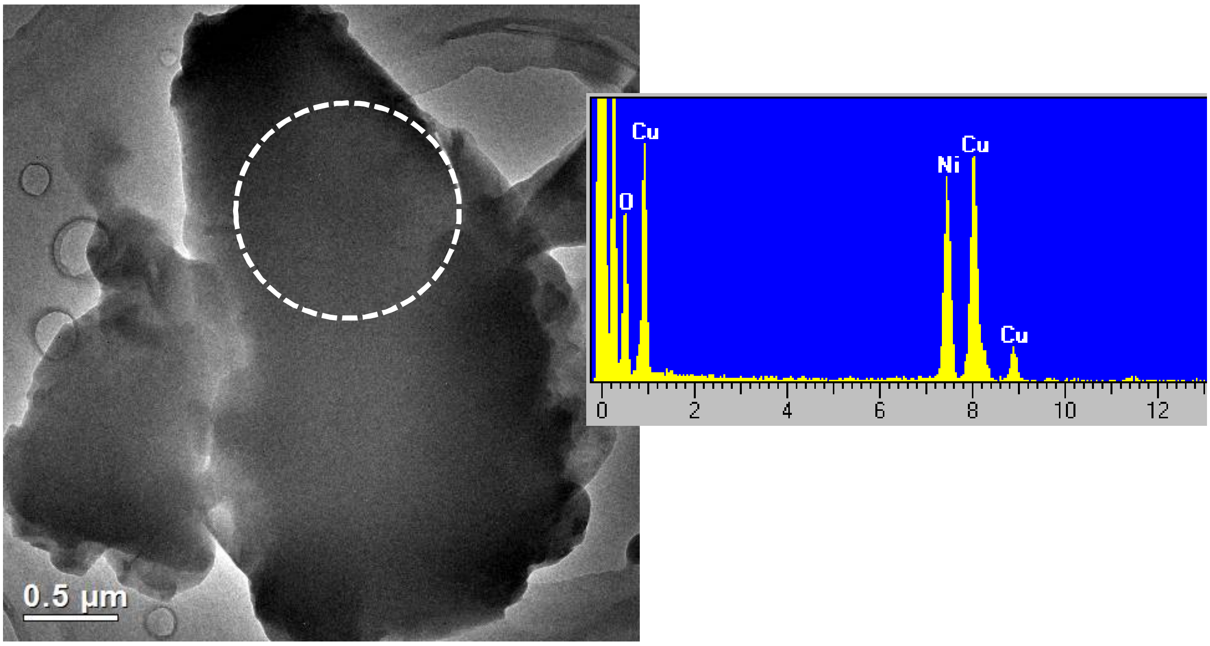

Figure 82: Further solid from pH adjusted synthesis. Note the EDX analysis indicates that while the MOF is present, no silica shell has been deposited on this piece of MOF. Dotted circle indicates the area where EDX analysis was undertaken on the sample.

To date, STAM-1 has yet to be consistently armoured using the published procedure. Future work on the topic will examine the particle size distribution of STAM-1 and attempt to control it via ball-milling.

6.6. Conclusions

CPO-27-Mg was successfully armoured using the same method published by Li and Zheng. This resulted in the armoured CPO-27-Mg material showing greater thermal stability but with no improvement in limiting the water uptake of the material. CPO-27-Mg may be subjected to the armouring process without any noted loss of structure or impairment of the CO_2 capacity of the MOF material. Further research regarding the modification of the silica shell may yield materials which are able to take advantage of the recently published water-based synthesis of CPO-27-Mg by Cattaneo *et al* for future industrial production.[8]

STAM-1 could not be successfully armoured and several notable deviations from the procedure were observed that did not occur with HKUST-1. Despite the conditions STAM-1 was exposed to (basic aqueous environment, silica deposition, removal of template at 250°C), the porous structure remains in-tact but the uniform distribution of the silica over the MOF particles is hampered by the wide particle size distribution of the as-synthesised material. In the future, further work will be carried out to determine if the material can be successfully armoured through use of ball-milling and the resulting slurry being used as a reagent for the armouring process.

6.7. References

1 H.-C. ‘Joe’ Zhou and S. Kitagawa, *Chem. Soc. Rev.*, 2014, **43**, 5415–5418.

2 M. B. Gawande, A. Goswami, T. Asefa, H. Guo, A. V. Biradar, D.-L. Peng, R. Zboril and R. S. Varma, *Chem. Soc. Rev.*, 2015, **44**, 7540–7590.

3 P. Hu, J. V. Morabito and C.-K. Tsung, *ACS Catal.*, 2014, **4**, 4409–4419.

4 T. Li, J. E. Sullivan and N. L. Rosi, *J. Am. Chem. Soc.*, 2013, **135**, 9984–9987.

5 Y.-C. Sue, J.-W. Wu, S.-E. Chung, C.-H. Kang, K.-L. Tung, K. C.-W. Wu and F.-K. Shieh, *ACS Appl. Mater. Interfaces*, 2014, **6**, 5192–5198.

6 Z. Li and H. C. Zeng, *J. Am. Chem. Soc.*, 2014, **136**, 5631–5639.

7 L. Garzón-Tovar, A. Carné-Sánchez, C. Carbonell, I. Imaz and D. Maspoch, *J. Mater. Chem. A*, 2015, **3**, 20819–20826.

8 D. Cattaneo, S. J. Warrender, M. J. Duncan, R. Castledine, N. Parkinson, I. Haley and R. E. Morris, *Dalton Trans.*, 2015, **45**, 618–629.

Chapter 7 Conclusions and Future Work

7.1. Conclusions

The project, when initially envisioned, was primarily concerned with the use of ionic liquids to supplement the exceptional gas sorption properties of MOFs in order to make them suitable for use as adsorbents in respirator canisters. Use of MOFs as for gas sorption in/under "real-world" conditions is typically problematic for MOFs due to the presence of water, which has a high binding affinity for the co-ordinatively unsaturated sites that enable MOFs to remove reactive molecules from gas streams.

While water is typically easier to exclude in the laboratory, or even to a certain extent in industrial processes, the lack of control of the conditions that a respirator cartridge will encounter was deemed something that could not easily be surmounted by engineering of the MOF structure alone. This lead to the investigation of a number of composite materials that combine the useful properties of two different types of material to produce an overall more effective solution.

The attempted impregnation of MOFs into silica monoliths was attempted, still using the CPO-27 series of MOFs, which involved the synthesis of a silica monolith and then subsequent wet impregnation of the MOF components to allow MMOF formation to take place inside the pores of the monolith. These materials were successfully synthesised and tested for ammonia breakthrough and water uptake properties.

The materials showed a reasonable uptake of ammonia in dry conditions. Adsorption of CO_2 by these materials indicated that the gas uptake of the MOF component of the material was not impeded in any way, with the capacity for the quantity of MOF present in each of the samples being around 95% of those reported for the as-synthesised MOF. This is likely due to pore blockages and incomplete reactions occurring inside the monoliths leaving some of the material unable to take up gas. Typical ammonia breakthrough times in dry conditions were around 40 minutes, a significant increase on the typical canister currently in use, which operates effectively in dry conditions for around 15 minutes.

The water uptake of the materials was not, however, improved by the production of the composite material and attempts to further increase the hydrophobic nature of the monolith in a post-synthetic manner did not give any noticeable improvement . Typical breakthrough times dropped below 10 minutes, approximately the same as the currently available canister. This was determined by STEM that the MOF grew both inside and out of the silica monoliths, which did not inhibit water uptake and a result gave diminished uptake of ammonia in humid conditions.

A more complete encapsulation was attempted, based on the synthesis published by Li and Zheng, which would directly deposit a silica shell around the MOF particles. This was achieved by first coating the MOF particles with a polymer, which enabled the deposited silica to adhere to the outer surface of the MOF. The polymer was then removed by calcination, leaving the individual MOF particles fully/completely encased in a layer of silica. This worked well on CPO-27-Mg and the material displayed significant improvement in resistance to high temperatures as a result. This form of silica-MOF hybrid material also had am increased ratio of MOF to silica in the composite, resulting in a higher effective uptake from the same weight of material. Again, however, the water adsorption was not diminished by the different method of protection. Research was shifted onto the material STAM-1, which exhibits a dual-pore system of hydrophobic and hydrophilic pores and was reported to have excellent stability in water. This material was also subjected to the armouring process which was ineffective due to the varied particle size produced by the synthesis of STAM-1. Work on the armoured material led, however, to the discovery whereby effective ammonia capacity improved in humid conditions.

This increase in capacity was determined to be a result of the changing of the structure of STAM-1 during dehydration. Although this was not directly observable in STAM-1 due to loss of single crystal character when dehydrated but was observed on a similar material Cu(EtOip)(H_2O), which also is also composed of a 5-substituted isophthalic acid ligand, results in the hydrophilic pores closing when coordinated water molecules are removed as the copper acetate lanterns in the structure would shift so that some of the coordination sites that have been vacated by water molecules can be occupied by carboxylate oxygen atoms from adjacent sheets. Powder X-ray diffraction studies on both STAM-1 and Cu(EtOip)(H_2O) show that the two compounds undergo the same structural transition upon dehydration. When re-hydrated, the pores revert to their open state and the ammonia was able to enter the pores and displace the water from the metal-centres. This gave an effective 50% increase in capacity of the material.

The MOF itself was then investigated for its capacity and capability to withstand adverse conditions in comparison with HKUST-1, a well-studied MOF that has exceptional capacity in dry conditions but poor stability in humid conditions. STAM-1 was shown to be capable of maintaining both its structure and capacity after exposure to high humidity and temperature, where HKUST-1 was found to decompose under the same conditions.

7.2. Future Work

Work continuing along the theme of this project will be undertaken by examination of the 5-substituted isophthalic acid derivatives developed by Dr. L. J. McCormick, examining their capacity and stability in the same manner as STAM-1, as well as combining the MOF materials with activated carbons to make a material more in line with standard respirator cartridges. The derivative compounds can also be used to observe the gas uptake crystallographically using the gas cells available at the Advanced Light Source at UC Berkeley or at the Diamond Light Source in the UK. The continued research in this area will be supported by Dstl as part of the PhD Scheme with Lauren McHugh being the next PhD candidate to carry on this work.

The armouring process represents an interesting method of potentially improving the stability of MOFs that are not suitable for some industrial processes due to their relative fragility. While the conditions that the MOF would need to be exposed to undergo the armouring process are relatively harsh, they can be adapted to suit individual frameworks on a case-by-case basis. In particular the most challenging step is the removal of the template material. It may be possible to develop a method using a different templating agent, such as an ionic liquid (ionic liquids have been known to template mesoporous silicas), which may be removed by solvent extraction rather than by calcination. By adjusting the 'armouring' conditions to suit other interesting MOFs that are not stable at high temperatures, it may be possible to create “task-specific” catalysts that exploit the properties of MOFs where they could not be used before, such as high-temperature catalytic processes or for the slow release of a loaded gas by altering the kinetics of release.

Appendix

Table 1. Crystal data and structure refinement for CuEtOiP

Identification code	CuEtOipRT	
Empirical formula	C10 H11.33 Cu O6.67	
Formula weight	301.73	
Temperature	300(2) K	
Wavelength	0.7749 Å	
Crystal system	Trigonal	
Space group	P -3 m 1	
Unit cell dimensions	a = 18.5676(12) Å	α= 90°.
	b = 18.5676(12) Å	β= 90°.
	c = 6.8056(6) Å	γ = 120°.
Volume	2031.9(3) Å^3	
Z	6	
Density (calculated)	1.479 Mg/m^3	
Absorption coefficient	2.060 mm^{-1}	
F(000)	922	
Crystal size	0.07 x 0.03 x 0.02 mm^3	
Theta range for data collection	2.392 to 33.184°.	
Index ranges	-26<=h<=26, -26<=k<=26, -9<=l<=9	
Reflections collected	26279	
Independent reflections	2174 [R(int) = 0.0673]	
Completeness to theta = 27.706°	99.9 %	
Absorption correction	Semi-empirical from equivalents	
Max. and min. transmission	0.7465 and 0.6282	
Refinement method	Full-matrix least-squares on F^2	
Data / restraints / parameters	2174 / 1 / 95	
Goodness-of-fit on F^2	1.059	
Final R indices [I>2sigma(I)]	R1 = 0.0384, wR2 = 0.1023	
R indices (all data)	R1 = 0.0496, wR2 = 0.1087	
Extinction coefficient	n/a	
Largest diff. peak and hole	0.782 and -1.005 e.Å^{-3}	

Table 2. Atomic coordinates (x 10^4) and equivalent isotropic displacement parameters ($Å^2$x 10^3) for sad_a. U(eq) is defined as one third of the trace of the orthogonalized U^{ij} tensor.

	x	y	z	U(eq)
Cu(1)	5236(1)	4764(1)	3446(1)	20(1)
O(1)	5889(1)	5589(1)	7537(3)	43(1)
O(2)	6288(1)	5198(1)	4866(3)	42(1)
O(1W)	5628(1)	4372(1)	885(4)	41(1)
O(3)	8411(1)	6822(2)	11892(5)	59(1)
C(1)	6407(1)	5497(1)	6556(3)	26(1)
C(2)	7229(1)	5752(1)	7491(3)	28(1)
C(3)	7778(1)	5556(2)	6566(5)	29(1)
C(4)	7435(1)	6168(2)	9287(4)	34(1)
C(5)	8196(1)	6393(2)	10173(6)	37(1)
C(6)	9138(4)	7118(4)	12753(10)	55(2)
C(7)	9200(6)	7631(6)	14483(14)	87(3)
O(2W)	7156(4)	4312(7)	1905(17)	80
O(3W)	6667	3333	5540(30)	80
O(4W)	7013(8)	4025(16)	120(40)	80

Table 3. Bond lengths [Å] and angles [°] for sad_a.

Cu(1)-O(2)#1	1.9550(17)
Cu(1)-O(2)	1.9550(17)
Cu(1)-O(1)#2	1.9688(17)
Cu(1)-O(1)#3	1.9688(17)
Cu(1)-O(1W)	2.150(3)
Cu(1)-Cu(1)#2	2.6059(7)
O(1)-C(1)	1.251(3)
O(1)-Cu(1)#2	1.9688(16)
O(2)-C(1)	1.248(3)
O(1W)-H(1W)	0.87(2)
O(3)-C(6)	1.313(7)
O(3)-C(6)#4	1.313(7)
O(3)-C(5)	1.358(4)
C(1)-C(2)	1.495(3)
C(2)-C(3)	1.392(3)
C(2)-C(4)	1.394(3)
C(3)-C(2)#4	1.392(3)
C(3)-H(3)	0.9300
C(4)-C(5)	1.395(3)
C(4)-H(4)	0.9300
C(5)-C(4)#4	1.395(3)
C(6)-C(7)	1.482(11)
C(6)-H(6A)	0.9700
C(6)-H(6B)	0.9700
C(7)-H(7A)	0.9600
C(7)-H(7B)	0.9600
C(7)-H(7C)	0.9600
O(2W)-O(4W)	1.30(3)
O(2)#1-Cu(1)-O(2)	89.73(13)
O(2)#1-Cu(1)-O(1)#2	89.83(10)
O(2)-Cu(1)-O(1)#2	168.60(7)
O(2)#1-Cu(1)-O(1)#3	168.60(7)
O(2)-Cu(1)-O(1)#3	89.83(10)
O(1)#2-Cu(1)-O(1)#3	88.36(14)
O(2)#1-Cu(1)-O(1W)	95.93(7)
O(2)-Cu(1)-O(1W)	95.93(7)
O(1)#2-Cu(1)-O(1W)	95.45(7)

O(1)#3-Cu(1)-O(1W)	95.45(8)
O(2)#1-Cu(1)-Cu(1)#2	83.97(5)
O(2)-Cu(1)-Cu(1)#2	83.97(5)
O(1)#2-Cu(1)-Cu(1)#2	84.66(5)
O(1)#3-Cu(1)-Cu(1)#2	84.66(5)
O(1W)-Cu(1)-Cu(1)#2	179.85(8)
C(1)-O(1)-Cu(1)#2	122.32(15)
C(1)-O(2)-Cu(1)	123.89(15)
Cu(1)-O(1W)-H(1W)	109(7)
C(6)-O(3)-C(6)#4	109.9(6)
C(6)-O(3)-C(5)	124.6(3)
C(6)#4-O(3)-C(5)	124.6(3)
O(2)-C(1)-O(1)	125.1(2)
O(2)-C(1)-C(2)	117.33(19)
O(1)-C(1)-C(2)	117.55(19)
C(3)-C(2)-C(4)	120.5(2)
C(3)-C(2)-C(1)	119.3(2)
C(4)-C(2)-C(1)	120.18(19)
C(2)-C(3)-C(2)#4	119.3(3)
C(2)-C(3)-H(3)	120.4
C(2)#4-C(3)-H(3)	120.4
C(2)-C(4)-C(5)	120.1(2)
C(2)-C(4)-H(4)	120.0
C(5)-C(4)-H(4)	120.0
O(3)-C(5)-C(4)#4	120.24(16)
O(3)-C(5)-C(4)	120.24(16)
C(4)#4-C(5)-C(4)	119.5(3)
O(3)-C(6)-C(7)	110.8(6)
O(3)-C(6)-H(6A)	109.5
C(7)-C(6)-H(6A)	109.5
O(3)-C(6)-H(6B)	109.5
C(7)-C(6)-H(6B)	109.5
H(6A)-C(6)-H(6B)	108.1
C(6)-C(7)-H(7A)	109.5
C(6)-C(7)-H(7B)	109.5
H(7A)-C(7)-H(7B)	109.5
C(6)-C(7)-H(7C)	109.5
H(7A)-C(7)-H(7C)	109.5
H(7B)-C(7)-H(7C)	109.5

Symmetry transformations used to generate equivalent atoms:

#1 -y+1,-x+1,z   #2 -x+1,-y+1,-z+1   #3 y,x,-z+1

#4 -x+y+1,y,z

Table 4. Anisotropic displacement parameters ($Å^2$x 10^3)for sad_a. The anisotropic displacement factor exponent takes the form: $-2\pi^2[h^2a^{*2}U^{11} + ... + 2 h k a^* b^* U^{12}]$

	U^{11}	U^{22}	U^{33}	U^{23}	U^{13}	U^{12}
Cu(1)	23(1)	23(1)	21(1)	0(1)	0(1)	16(1)
O(1)	29(1)	74(1)	36(1)	-14(1)	-6(1)	33(1)
O(2)	28(1)	70(1)	36(1)	-18(1)	-9(1)	31(1)
O(1W)	53(1)	53(1)	29(1)	-4(1)	4(1)	35(1)
O(3)	53(1)	84(2)	52(2)	-39(2)	-20(1)	42(1)
C(1)	22(1)	31(1)	30(1)	3(1)	-1(1)	17(1)
C(2)	22(1)	35(1)	32(1)	-2(1)	-2(1)	17(1)
C(3)	25(1)	39(2)	28(1)	-3(1)	-2(1)	20(1)
C(4)	27(1)	44(1)	38(1)	-9(1)	-3(1)	24(1)
C(5)	31(1)	50(2)	37(2)	-16(2)	-8(1)	25(1)

Table 5. Hydrogen bonds for sad_a [Å and °].

D-H...A	d(D-H)	d(H...A)	d(D...A)	<(DHA)
O(1W)-H(1W)...O(1)#5	0.87(2)	2.37(6)	3.072(3)	138(8)

Symmetry transformations used to generate equivalent atoms:

#1 -y+1,-x+1,z #2 -x+1,-y+1,-z+1 #3 y,x,-z+1

#4 -x+y+1,y,z #5 -y+1,-x+1,z-1

Table 1. Crystal data and structure refinement for CuEtOip -dehydrated

Identification code	CuEtOipRTvac	
Empirical formula	C10 H8 Cu O5	
Formula weight	271.70	
Temperature	300(2) K	
Wavelength	0.7749 Å	
Crystal system	Trigonal	
Space group	P 3 1 m	
Unit cell dimensions	a = 33.028(3) Å	α= 90°.
	b = 33.028(3) Å	β= 90°.
	c = 5.2047(6) Å	γ = 120°.
Volume	4917.0(10) $Å^3$	
Z	18	
Density (calculated)	1.652 Mg/m^3	
Absorption coefficient	2.529 mm^{-1}	
F(000)	2466	
Crystal size	0.07 x 0.03 x 0.02 mm^3	
Theta range for data collection	2.329 to 24.079°.	
Index ranges	-34<=h<=34, -34<=k<=34, -5<=l<=5	
Reflections collected	26548	
Independent reflections	4168 [R(int) = 0.0955]	
Completeness to theta = 24.079°	99.8 %	
Absorption correction	Semi-empirical from equivalents	
Max. and min. transmission	0.7450 and 0.45325	
Refinement method	Full-matrix least-squares on F^2	
Data / restraints / parameters	4168 / 8 / 188	
Goodness-of-fit on F^2	1.101	
Final R indices [I>2sigma(I)]	R1 = 0.1503, wR2 = 0.3249	
R indices (all data)	R1 = 0.1666, wR2 = 0.3362	
Absolute structure parameter	0.54(12)	
Extinction coefficient	n/a	
Largest diff. peak and hole	2.575 and -4.046 e.$Å^{-3}$	

Table 2. Atomic coordinates (x 10^4) and equivalent isotropic displacement parameters (Å^{2}x 10^3) for sad_a. U(eq) is defined as one third of the trace of the orthogonalized U^{ij} tensor.

	x	y	z	U(eq)
C(1)	7329(12)	8198(12)	3790(70)	8(8)
C(2)	7755(12)	8174(12)	4410(70)	7(8)
C(3)	7815(15)	7815(15)	3410(90)	10(11)
C(4)	8049(13)	8435(13)	6640(70)	19(9)
C(5)	8390(20)	8390(20)	7490(130)	36(16)
C(6)	9140(30)	8760(30)	9390(180)	30(20)
C(8)	7163(15)	9145(15)	890(80)	20(10)
C(9)	7528(11)	9597(11)	-130(60)	2(7)
C(10)	7580(15)	10000	810(90)	9(11)
C(11)	7790(14)	9606(14)	-2270(80)	21(9)
C(12)	8147(17)	10000	-3210(100)	21(13)
C(13)	8380(30)	9550(20)	-5750(140)	12(17)
C(15)	6168(11)	7578(12)	5680(60)	5(8)
C(16)	5792(9)	7163(10)	6720(50)	37(12)
C(17)	5692(13)	6729(13)	5780(60)	64(17)
C(18)	5352(16)	6323(10)	6970(90)	90(20)
C(19)	5113(13)	6352(10)	9090(80)	100(30)
C(20)	5213(12)	6787(13)	10030(60)	64(17)
C(21)	5553(11)	7192(10)	8840(60)	32(11)
C(22)	4740(20)	10580(20)	6680(110)	53(15)
C(23)	4938(18)	7188(18)	12670(100)	44(13)
C(24)	4580(20)	7050(20)	14990(110)	63(17)
C(25)	5090(30)	9370(20)	4000(120)	100(30)
C(26)	5190(20)	9023(19)	2440(110)	150(40)
C(27)	5532(17)	8924(15)	3300(70)	80(20)
C(28)	5615(11)	8608(13)	1970(70)	44(13)
C(29)	5359(14)	8391(13)	-230(70)	64(17)
C(30)	5019(15)	8490(17)	-1100(80)	71(18)
C(31)	4936(18)	8810(20)	240(110)	190(50)
C(32)	6001(19)	8502(18)	2940(80)	56(16)
C(33)	4300(30)	8200(30)	-3450(170)	110(30)
C(34)	4110(20)	7910(20)	-6380(130)	70(20)
O(1)	7147(10)	8067(11)	1460(50)	26(7)
O(2)	7273(9)	8487(9)	5080(50)	19(6)
O(3)	8689(14)	8689(14)	9060(90)	43(12)

O(4)	6983(9)	8769(9)	-360(50)	11(6)
O(5)	7067(11)	9153(11)	3200(60)	33(8)
O(6)	8416(12)	10000	-5070(70)	26(10)
O(7)	6229(8)	7587(8)	3480(50)	13(6)
O(8)	6353(10)	7957(10)	7030(60)	23(6)
O(9)	4650(13)	10494(12)	4250(70)	45(9)
O(10)	4870(17)	10380(17)	8380(100)	84(14)
O(11)	4931(15)	6781(14)	11820(70)	60(11)
O(12)	5000(30)	9560(20)	2070(130)	150(30)
O(13)	5280(13)	9551(13)	6000(70)	52(10)
O(14)	6084(9)	8272(9)	1280(50)	17(6)
O(15)	6203(9)	8671(9)	5080(50)	20(6)
O(16)	4730(19)	8159(19)	-2860(100)	96(16)
Cu(1)	6579(2)	8126(2)	1190(12)	40(2)
Cu(2)	6753(2)	8593(2)	5463(9)	25(1)
Cu(3)	5131(2)	10000	6985(12)	12(2)
Cu(4)	4749(2)	10000	2693(12)	20(2)

Table 3. Bond lengths [Å] and angles [°] for sad_a.

C(1)-O(2)	1.26(4)
C(1)-O(1)	1.32(4)
C(1)-C(2)	1.48(5)
C(2)-C(3)	1.40(4)
C(2)-C(4)	1.49(5)
C(3)-C(2)#1	1.40(4)
C(3)-H(3)	0.9300
C(4)-C(5)	1.28(5)
C(4)-H(4)	0.9300
C(5)-C(4)#1	1.28(5)
C(5)-O(3)	1.29(8)
C(6)-O(3)	1.39(9)
C(8)-O(5)	1.25(5)
C(8)-O(4)	1.26(5)
C(8)-C(9)	1.47(5)
C(9)-C(10)	1.35(4)
C(9)-C(11)	1.40(5)
C(10)-C(9)#2	1.35(4)
C(10)-H(10)	0.9300
C(11)-C(12)	1.34(5)
C(11)-H(11)	0.9300
C(12)-O(6)	1.31(7)
C(12)-C(11)#2	1.34(5)
C(13)-O(6)	1.47(7)
C(15)-O(7)	1.16(4)
C(15)-O(8)	1.29(5)
C(15)-C(16)	1.42(4)
C(16)-C(17)	1.3900
C(16)-C(21)	1.3900
C(17)-C(18)	1.3900
C(17)-H(17)	0.9300
C(18)-C(19)	1.3900
C(18)-C(22)#3	1.48(7)
C(19)-C(20)	1.3900
C(19)-H(19)	0.9300
C(20)-O(11)	1.31(5)
C(20)-C(21)	1.3900
C(21)-H(21)	0.9300

C(22)-O(10)	1.29(7)
C(22)-O(9)	1.30(6)
C(22)-C(18)#4	1.48(14)
C(23)-O(11)	1.40(6)
C(23)-C(24)	1.59(7)
C(23)-H(23A)	0.9700
C(23)-H(23B)	0.9700
C(24)-H(24A)	0.9600
C(24)-H(24B)	0.9600
C(24)-H(24C)	0.9600
C(25)-O(13)	1.21(5)
C(25)-O(12)	1.30(5)
C(25)-C(26)	1.57(5)
C(25)-Cu(3)	2.55(5)
C(26)-C(27)	1.3900
C(26)-C(31)	1.3900
C(27)-C(28)	1.3900
C(27)-H(27)	0.9300
C(28)-C(29)	1.3900
C(28)-C(32)	1.56(6)
C(29)-C(30)	1.3900
C(29)-H(29)	0.9300
C(30)-O(16)	1.38(6)
C(30)-C(31)	1.3900
C(31)-H(31)	0.9300
C(32)-O(14)	1.27(4)
C(32)-O(15)	1.28(4)
C(33)-O(16)	1.53(9)
C(33)-C(34)	1.74(10)
C(33)-H(33A)	0.9700
C(33)-H(33B)	0.9700
C(34)-H(34A)	0.9600
C(34)-H(34B)	0.9600
C(34)-H(34C)	0.9600
O(1)-Cu(1)	1.99(3)
O(2)-Cu(2)	1.92(3)
O(3)-C(6)#1	1.39(9)
O(4)-Cu(1)	2.03(3)
O(4)-Cu(2)#5	2.28(2)
O(5)-Cu(2)	1.99(3)

O(6)-C(13)#2	1.47(8)
O(7)-Cu(1)	1.96(2)
O(8)-Cu(2)	2.01(3)
O(8)-Cu(1)#6	2.27(3)
O(9)-Cu(4)	1.99(4)
O(10)-Cu(3)	1.98(5)
O(12)-Cu(4)	2.03(7)
O(13)-Cu(3)	1.85(4)
O(14)-Cu(1)	1.92(3)
O(15)-Cu(2)	1.97(3)
Cu(1)-O(8)#5	2.27(3)
Cu(1)-Cu(2)	2.602(7)
Cu(2)-O(4)#6	2.28(2)
Cu(3)-O(13)#2	1.85(4)
Cu(3)-O(10)#2	1.98(5)
Cu(3)-C(25)#2	2.55(5)
Cu(3)-Cu(4)	2.566(9)
Cu(4)-O(9)#2	1.99(4)
Cu(4)-O(12)#2	2.03(7)

O(2)-C(1)-O(1)	122(3)
O(2)-C(1)-C(2)	115(3)
O(1)-C(1)-C(2)	118(3)
C(3)-C(2)-C(1)	120(3)
C(3)-C(2)-C(4)	117(3)
C(1)-C(2)-C(4)	120(3)
C(2)#1-C(3)-C(2)	118(5)
C(2)#1-C(3)-H(3)	120.8
C(2)-C(3)-H(3)	120.8
C(5)-C(4)-C(2)	124(4)
C(5)-C(4)-H(4)	118.1
C(2)-C(4)-H(4)	118.1
C(4)#1-C(5)-C(4)	119(6)
C(4)#1-C(5)-O(3)	120(3)
C(4)-C(5)-O(3)	120(3)
O(5)-C(8)-O(4)	121(4)
O(5)-C(8)-C(9)	115(4)
O(4)-C(8)-C(9)	124(4)
C(10)-C(9)-C(11)	120(3)
C(10)-C(9)-C(8)	120(3)

C(11)-C(9)-C(8)	120(3)
C(9)#2-C(10)-C(9)	118(5)
C(9)#2-C(10)-H(10)	121.0
C(9)-C(10)-H(10)	121.0
C(12)-C(11)-C(9)	123(4)
C(12)-C(11)-H(11)	118.4
C(9)-C(11)-H(11)	118.4
O(6)-C(12)-C(11)	122(3)
O(6)-C(12)-C(11)#2	122(3)
C(11)-C(12)-C(11)#2	115(5)
O(7)-C(15)-O(8)	121(3)
O(7)-C(15)-C(16)	117(3)
O(8)-C(15)-C(16)	119(3)
C(17)-C(16)-C(21)	120.0
C(17)-C(16)-C(15)	120(3)
C(21)-C(16)-C(15)	119(3)
C(16)-C(17)-C(18)	120.0
C(16)-C(17)-H(17)	120.0
C(18)-C(17)-H(17)	120.0
C(19)-C(18)-C(17)	120.0
C(19)-C(18)-C(22)#3	110(4)
C(17)-C(18)-C(22)#3	129(4)
C(18)-C(19)-C(20)	120.00(5)
C(18)-C(19)-H(19)	120.0
C(20)-C(19)-H(19)	120.0
O(11)-C(20)-C(21)	124(3)
O(11)-C(20)-C(19)	116(3)
C(21)-C(20)-C(19)	120.0
C(20)-C(21)-C(16)	120.0
C(20)-C(21)-H(21)	120.0
C(16)-C(21)-H(21)	120.0
O(10)-C(22)-O(9)	131(6)
O(10)-C(22)-C(18)#4	130(10)
O(9)-C(22)-C(18)#4	99(10)
O(11)-C(23)-C(24)	108(4)
O(11)-C(23)-H(23A)	110.2
C(24)-C(23)-H(23A)	110.2
O(11)-C(23)-H(23B)	110.2
C(24)-C(23)-H(23B)	110.2
H(23A)-C(23)-H(23B)	108.5

C(23)-C(24)-H(24A)	109.5
C(23)-C(24)-H(24B)	109.5
H(24A)-C(24)-H(24B)	109.5
C(23)-C(24)-H(24C)	109.5
H(24A)-C(24)-H(24C)	109.5
H(24B)-C(24)-H(24C)	109.5
O(13)-C(25)-O(12)	127(7)
O(13)-C(25)-C(26)	124(6)
O(12)-C(25)-C(26)	98(5)
O(13)-C(25)-Cu(3)	43(3)
O(12)-C(25)-Cu(3)	90(4)
C(26)-C(25)-Cu(3)	165(5)
C(27)-C(26)-C(31)	120.0
C(27)-C(26)-C(25)	120(4)
C(31)-C(26)-C(25)	120(4)
C(26)-C(27)-C(28)	120.0
C(26)-C(27)-H(27)	120.0
C(28)-C(27)-H(27)	120.0
C(29)-C(28)-C(27)	120.0
C(29)-C(28)-C(32)	120(3)
C(27)-C(28)-C(32)	120(3)
C(28)-C(29)-C(30)	120.0
C(28)-C(29)-H(29)	120.0
C(30)-C(29)-H(29)	120.0
O(16)-C(30)-C(31)	128(4)
O(16)-C(30)-C(29)	110(4)
C(31)-C(30)-C(29)	120.0
C(30)-C(31)-C(26)	120.0
C(30)-C(31)-H(31)	120.0
C(26)-C(31)-H(31)	120.0
O(14)-C(32)-O(15)	129(5)
O(14)-C(32)-C(28)	111(4)
O(15)-C(32)-C(28)	119(4)
O(16)-C(33)-C(34)	103(6)
O(16)-C(33)-H(33A)	111.1
C(34)-C(33)-H(33A)	111.1
O(16)-C(33)-H(33B)	111.1
C(34)-C(33)-H(33B)	111.1
H(33A)-C(33)-H(33B)	109.1
C(33)-C(34)-H(34A)	109.5

C(33)-C(34)-H(34B)	109.5
H(34A)-C(34)-H(34B)	109.5
C(33)-C(34)-H(34C)	109.5
H(34A)-C(34)-H(34C)	109.5
H(34B)-C(34)-H(34C)	109.5
C(1)-O(1)-Cu(1)	109(2)
C(1)-O(2)-Cu(2)	133(2)
C(5)-O(3)-C(6)	124(4)
C(5)-O(3)-C(6)#1	124(5)
C(6)-O(3)-C(6)#1	101(8)
C(8)-O(4)-Cu(1)	124(2)
C(8)-O(4)-Cu(2)#5	133(2)
Cu(1)-O(4)-Cu(2)#5	98.8(10)
C(8)-O(5)-Cu(2)	125(3)
C(12)-O(6)-C(13)#2	118(3)
C(12)-O(6)-C(13)	118(3)
C(13)#2-O(6)-C(13)	121(6)
C(15)-O(7)-Cu(1)	129(2)
C(15)-O(8)-Cu(2)	123(2)
C(15)-O(8)-Cu(1)#6	134(2)
Cu(2)-O(8)-Cu(1)#6	99.5(12)
C(22)-O(9)-Cu(4)	117(4)
C(22)-O(10)-Cu(3)	116(4)
C(20)-O(11)-C(23)	122(4)
C(25)-O(12)-Cu(4)	120(5)
C(25)-O(13)-Cu(3)	111(4)
C(32)-O(14)-Cu(1)	129(3)
C(32)-O(15)-Cu(2)	110(3)
C(30)-O(16)-C(33)	112(5)
O(14)-Cu(1)-O(7)	91.3(11)
O(14)-Cu(1)-O(1)	170.5(12)
O(7)-Cu(1)-O(1)	91.4(11)
O(14)-Cu(1)-O(4)	86.8(11)
O(7)-Cu(1)-O(4)	166.2(10)
O(1)-Cu(1)-O(4)	88.4(11)
O(14)-Cu(1)-O(8)#5	82.5(10)
O(7)-Cu(1)-O(8)#5	112.5(10)
O(1)-Cu(1)-O(8)#5	104.8(11)
O(4)-Cu(1)-O(8)#5	80.8(9)
O(14)-Cu(1)-Cu(2)	78.1(8)

O(7)-Cu(1)-Cu(2)	82.8(8)
O(1)-Cu(1)-Cu(2)	93.3(9)
O(4)-Cu(1)-Cu(2)	83.4(7)
O(8)#5-Cu(1)-Cu(2)	155.5(7)
O(2)-Cu(2)-O(15)	168.1(11)
O(2)-Cu(2)-O(5)	90.6(12)
O(15)-Cu(2)-O(5)	84.4(12)
O(2)-Cu(2)-O(8)	91.9(11)
O(15)-Cu(2)-O(8)	90.6(11)
O(5)-Cu(2)-O(8)	167.0(13)
O(2)-Cu(2)-O(4)#6	86.0(10)
O(15)-Cu(2)-O(4)#6	105.9(10)
O(5)-Cu(2)-O(4)#6	112.0(11)
O(8)-Cu(2)-O(4)#6	80.9(10)
O(2)-Cu(2)-Cu(1)	76.0(8)
O(15)-Cu(2)-Cu(1)	92.7(8)
O(5)-Cu(2)-Cu(1)	84.5(9)
O(8)-Cu(2)-Cu(1)	83.8(9)
O(4)#6-Cu(2)-Cu(1)	155.9(7)
O(13)-Cu(3)-O(13)#2	88(2)
O(13)-Cu(3)-O(10)#2	102.8(19)
O(13)#2-Cu(3)-O(10)#2	169.0(19)
O(13)-Cu(3)-O(10)	169.0(19)
O(13)#2-Cu(3)-O(10)	102.8(18)
O(10)#2-Cu(3)-O(10)	66(3)
O(13)-Cu(3)-C(25)	26.4(15)
O(13)#2-Cu(3)-C(25)	95(2)
O(10)#2-Cu(3)-C(25)	96(2)
O(10)-Cu(3)-C(25)	151(2)
O(13)-Cu(3)-C(25)#2	95(2)
O(13)#2-Cu(3)-C(25)#2	26.4(15)
O(10)#2-Cu(3)-C(25)#2	151(2)
O(10)-Cu(3)-C(25)#2	96(2)
C(25)-Cu(3)-C(25)#2	91(4)
O(13)-Cu(3)-Cu(4)	95.0(12)
O(13)#2-Cu(3)-Cu(4)	95.0(12)
O(10)#2-Cu(3)-Cu(4)	87.0(15)
O(10)-Cu(3)-Cu(4)	87.0(15)
C(25)-Cu(3)-Cu(4)	69.1(15)
C(25)#2-Cu(3)-Cu(4)	69.1(15)

O(9)-Cu(4)-O(9)#2	91(2)
O(9)-Cu(4)-O(12)	161(2)
O(9)#2-Cu(4)-O(12)	94(2)
O(9)-Cu(4)-O(12)#2	94(2)
O(9)#2-Cu(4)-O(12)#2	161(2)
O(12)-Cu(4)-O(12)#2	77(4)
O(9)-Cu(4)-Cu(3)	85.9(10)
O(9)#2-Cu(4)-Cu(3)	85.9(10)
O(12)-Cu(4)-Cu(3)	76.2(19)
O(12)#2-Cu(4)-Cu(3)	76.2(19)

Symmetry transformations used to generate equivalent atoms:

#1 y,x,z #2 x-y+1,-y+2,z #3 -x+1,-x+y,z #4 -x+1,-x+y+1,z
#5 x,y,z-1 #6 x,y,z+1

Table 4. Anisotropic displacement parameters ($Å^2$x 10^3)for sad_a. The anisotropic displacement factor exponent takes the form: $-2\pi^2[h^2a^{*2}U^{11} + ... + 2 h k a^* b^* U^{12}]$

	U^{11}	U^{22}	U^{33}	U^{23}	U^{13}	U^{12}
Cu(1)	18(3)	17(3)	85(5)	-15(3)	-1(3)	8(3)
Cu(2)	22(3)	16(3)	38(3)	-12(2)	-4(2)	10(2)

Equation for Calculation of Quantity of MOF present in ICP Sample.

0.7718 mg	mass of sample
614 ppb	[Mg^{2+}] in 10 mL solution
6.14×10^{-10} mg/mL	[Mg^{2+}] in 10 mL solution
6.14×10^{-9} mg	mass of Mg^{2+} in 10 mL solution
1.49×10^{-7} mol	no of mol of Mg^{2+} in 10 mL solution
7.46×10^{-8} mol	no of mol of CPO-27-Mg in 10 mL solution
278.741	molar mass of CPO-27-Mg
2.08×10^{-5} mg	mass of CPO-27-Mg in 10 mL solution